University of Bristol - Explore Bristol Research
General rights

Data-driven modelling of social forces and collective behaviour in zebrafish

Adam K Zienkiewicz[a], Fabrizio Ladu[b], David A W Barton[a],
Maurizio Porfiri[b,1,*], Mario Di Bernardo[a,c,1,*]

[a]Department of Engineering Mathematics, University of Bristol, UK
[b]Department of Mechanical and Aerospace Engineering, New York University Tandon School of Engineering, USA
[c]Department of Electrical Engineering and ICT, University of Naples Federico II, Italy

Abstract

Zebrafish are rapidly emerging as a powerful model organism in hypothesis-driven studies targeting a number of functional and dysfunctional processes. Mathematical models of zebrafish behaviour can inform the design of experiments, through the unprecedented ability to perform pilot trials on a computer. At the same time, *in-silico* experiments could help refining the analysis of real data, by enabling the systematic investigation of key neurobehavioural factors. Here, we establish a data-driven model of zebrafish social interaction. Specifically, we derive a set of interaction rules to capture the primary response mechanisms which have been observed experimentally. Contrary to previous studies, we include dynamic speed regulation in addition to turning responses, which together provide attractive, repulsive and alignment interactions between individuals. The resulting multi-agent model provides a novel, bottom-up framework to describe both the spontaneous motion and individual-level interaction dynamics of zebrafish, inferred directly from experimental observations.

Keywords: Zebrafish, stochastic differential equations, agent-based modelling, data-driven

1. Introduction

Zebrafish are fast emerging as a species of choice in preclinical research [1–4]; the main reasons being its neurogenetic similarities with humans, ease of stocking and maintenance, short intergeneration time, and rich behavioural repertoires in response to environmental and psychoactive compounds [5–8]. The locomotion of this freshwater species is governed chiefly by forward bursts of acceleration, followed by a period of coasting, or deceleration. Turns are achieved by a conformation of body posture, resulting in a change in heading direction, followed by further forward bursts in the new direction [9–12].

Data-driven models of zebrafish promise to aid neurobehavioral science, by empowering researchers with computational tools to conduct pilot in-silico experiments, refine experimental observations, and enhance statistical analysis. Much of the existing work has focused on

---

*Corresponding authors
Email address: `mporfiri@nyu.edu, m.dibernardo@bristol.ac.uk` (Mario Di Bernardo)
[1]These authors contributed equally to this work

individual response of zebrafish, swimming in isolation [13–15], to capture key behavioral phenotypes which have been experimentally observed [7]. For example, in [14], we explained the burst-and-coast swimming style of zebrafish and in [13] we investigated the emergence of thigmotactic response during interactions with tank walls.

A pressing open problem is the derivation of computational models able to capture social interaction between zebrafish swimming in a shoal, and reproduce experimentally observed social behaviour [16–19]. An improved understanding of social interactions can help identifying and quantifying the biological advantages of living in groups, and the role of pharmacological manipulations on group behaviour [20]

Formulating an accurate model of zebrafish social behaviour requires the precise quantification of "social forces" between individual fish [21–23]. Central to this approach is to compute, for each individual at every time-sample, the reaction forces which describe how a focal agent moves, or accelerates, in response to the current "social" configuration of itself and a local neighbour. These configurations are typically described by measurable spatial quantities, for example, the relative position and orientation of a neighbour with respect to the focal individual. Dynamic variables, such as the speed and acceleration of individuals are also taken into account into the description of a pair-wise configuration. The notion of social forces has been successfully applied to study social behaviour of other teleosts, such as golden shiners [21] and mosquitofish [22].

In previous work, we presented preliminary models to capture some aspects of the interaction among zebrafish swimming together towards exploring leader-follower relationships. Specifically, in [24], we examined the interactions between two zebrafish in terms of their turn rate dynamics, without considering speed regulation or wall interaction. In [25], we explored the effects of leaders onto the dynamics of a virtual zebrafish shoal based on a preliminary model of social interaction between conspecifics – developed in more detail in this work.

In this paper, we establish a data-driven model of zebrafish social interaction building on our previous work and on recent analytical methods which have been used to infer interaction behaviours within social animal groups [21, 22, 26, 27].

In particular, we derive a set of interaction rules to capture the primary response mechanisms which have been observed experimentally [28, 29]. Inspired by recent models proposed by Gautrais, Calovi and others [30–32], we subsequently incorporate interaction behaviours into our original model framework [13], in a way which leaves the unique locomotory patterns of individuals intact. Importantly here, we include *dynamic speed regulation* in addition to turning responses, showing that together they better capture experimental observations of attractive, repulsive and alignment interactions between individuals. Variable speed is a fundamental feature of the locomotory patterns of zebrafish and similar species [10, 33]. Similarly, the ability to modulate forward speed with respect to neighbours has also been proposed as a central mechanism for explaining collective behaviour of similar teleosts [21, 22, 34–36].

Our multi-agent model provides a novel, bottom-up framework to describe both the spontaneous motion and individual-level interaction dynamics of zebrafish — inferred directly from experimental observations. In contrast to the conclusions of a similar study [21], we also report evidence of an explicit alignment mechanism between co-swimming zebrafish. Specifically, we use force-mapping analysis to decompose the observed turning responses into distinct attractive and alignment components. These behaviours are subsequently included in the model construction, by determining the relative contributions of each response, as a

function of the spatial configuration of zebrafish pairs.

2. Social-force mapping of zebrafish interactions

The first step towards a comprehensive mathematical model is the identification of the social forces acting on an individual zebrafish as a result of the presence of its conspecifics. These forces are measured from the acceleration of a focal fish at any instant in time — ignoring strictly physical quantities such as mass and momentum. The assumption is that by analysing experimental trajectory data from periods in which fish are swimming in close proximity, we can isolate the accelerations due to their specific interaction responses. Provided sufficient data is collected, accelerations due to interactions are manifested against the residual (random) background from the spontaneous motion of individuals. In this study, we therefore consider composites of multiple observations of zebrafish pairs, swimming together for extended periods of time.

2.1. Data collection

The experiments described in this study, similar to those in [13], are designed to extract sufficient information from live zebrafish in order to reconstruct swimming trajectories — specifically in terms of position, speed, angular velocity (turn-rate) and associated accelerations as a function of time.

We use 18×20 min observations of swimming zebrafish *pairs* from experiments carried out at the Dynamical Systems Laboratory of New York University. Each pair was video recorded from above a shallow (10 cm depth), circular tank after which trajectory data was extracted to obtain unique time-series of centroid positions $\mathbf{x}_i(t)$ for each fish i at time t (see online supporting information (SI): video V1).

The depth of water in the experimental tank is designed to reflect the natural habitat of zebrafish which occupy shallow, slow-flowing waters [37]. The primary component of their collective motion is therefore in the plane, justifying our analysis based on two-dimensional data captured from a single overhead perspective. Ultimately from this data we are able to compute linear components of the fish's acceleration: $a_i^{\parallel}$ in the direction of motion, and $a_i^{\perp}$ in the radial direction, perpendicular to the fish's heading direction (Fig. 1). Turning behaviour is further characterised by computing angular turn-rates $\omega_i(t)$ and the angular accelerations $\dot{\omega}_i(t)$. The same dataset is utilized in [24] and [25].

In what follows, we show how this information is obtained and subsequently analysed to infer average interaction responses of a fish with respect to its neighbours. Specifically, we present and discuss the results of force mapping analysis for experimental observations of co-swimming zebrafish pairs. For each mapping described, data is averaged over all 18 pair observations, taking each fish in turn as the focal fish. Using a coordinate system in the frame of the focal fish (Fig. 1), we compute population density and force maps such that the focal fish's orientation is aligned with the y-axis of each plot.

2.2. Zebrafish response as a function of relative position

The mapping shown in Fig. 2A depicts the population density of positions occupied by a neighbour over time, relative to the focal fish. The most populated region forms an ellipse, elongated in the direction of motion, with preferred separation distances of approximately

3

1 body-length (BL) in the front-back direction d_{FB}, and approximately $0.8\,\mathrm{BL}$ in the left-right direction d_{LR}. Regions with the highest probability of occupation by a neighboring fish are found to either side of the focal fish, with a preferred angle of $\pm 90°$ with respect to its orientation. This suggests that side-by-side swimming is somewhat more common than in-line (front-to-back) swimming. A low density region surrounding the focal fish indicates an exclusion, or repulsive zone in which neighbours are unlikely to be found. Beyond the high density region, neighbours are less likely to be found further than $3\,\mathrm{BL}$ to either side or $5\,\mathrm{BL}$ in front or behind ($< 1\%$ occupancy).

By computing the acceleration vector $\mathbf{a}(t) = [a^{\parallel}, a^{\perp}]$ of the focal fish in its body coordinate frame, we construct the mapping of the magnitude $|\mathbf{a}|$ (Fig. 2B). The tangential (forward-backwards / axial) and radial (left-right / lateral) components of the acceleration, $a^{\parallel}$ and $a^{\perp}$, are used to plot the vector field shown. As one expects, the high population density regions are associated with regions where the magnitude of the response force of the focal fish $|\mathbf{a}|$ is minimised. The region of lowest response however, forms an ellipse which encircles the focal fish but which is biased in the frontal direction. Within the (low density) repulsion zone, the avoidance response is mediated primarily by the tangential component $a^{\parallel}$, where we find strong deceleration, with acceleration vectors anti-aligned with the fish's orientation. Negative tangential acceleration (slowing down to avoid collisions) in the region just ahead of the focal fish, is much more pronounced than in the region behind, suggesting fish are more sensitive to neighbours directly in front of them, as could be expected for a reaction to visual stimuli. Directly behind the fish, there is some evidence of forward acceleration (rear collision avoidance), although small in comparison to frontal response.

In general, we find that the tangential acceleration $a^{\parallel}$ increases more rapidly in the frontal direction than behind, thereby the focal fish tends to accelerate to stay close to its neighbour by modulating its forward speed. Conversely, to the rear-left and rear-right of the focal
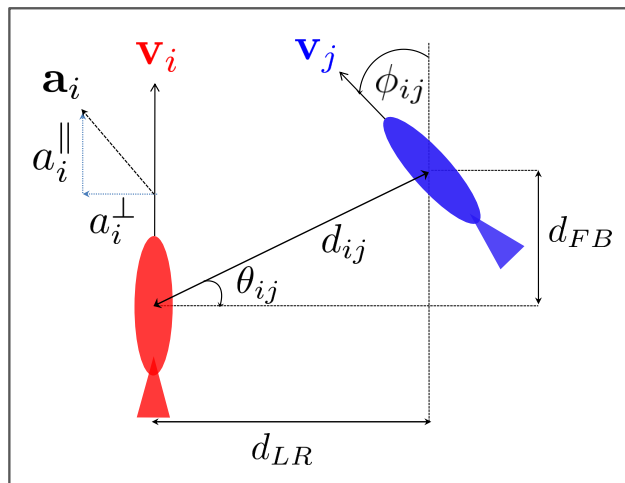

Figure 1: **Fish interaction coordinate system and separation metrics.** Cartesian coordinate system in frame of focal fish i, separated from its neighbour j by d_{ij} with front-back distance $d_{FB} = d_{ij}\sin\theta_{ij}$ and left-right distance $d_{LR} = d_{ij}\cos\theta_{ij}$ with respect to its velocity $\mathbf{v}_i$ (orientation). Angle θ_{ij} is formed between the heading direction of fish i and the relative position of fish j; with ϕ_{ij} giving the relative orientation (heading angle) of fish j with respect to fish i. The tank frame acceleration vector $\mathbf{a}_i$ is decomposed into a tangential acceleration $a_i^{\parallel}$ and a radial acceleration $a_i^{\perp}$ in the focal fish frame as shown.

4

fish, the radial acceleration $a^\perp$ dominates, suggesting that the fish expends more effort by turning, perhaps allowing for better visual perception of its neighbour, rather than to change its forward speed. Beyond a radius of approximately 2 BL away from the focal fish, it is the radial component $a^\perp$ which increases most with distance, where $|\mathbf{a}|$ is found to be greatest on either side of the focal fish, and reduced in the regions directly in front and to the rear.

We note that the mean speeds of individuals swimming in pairs are very well matched across all observations (Fig. S10A). Indeed, conspecifics must necessarily match their swimming speeds in order to remain close. However, observations of isolated individuals (Fig. S10B) suggest that their preferred, or intrinsic, swimming speed is somewhat lower but are likely to be sufficiently similar such that only minor accelerations ($a^\parallel$) are required when swimming in front-to-back arrangement. In contrast, the radial accelerations $a^\perp$ resulting from turns
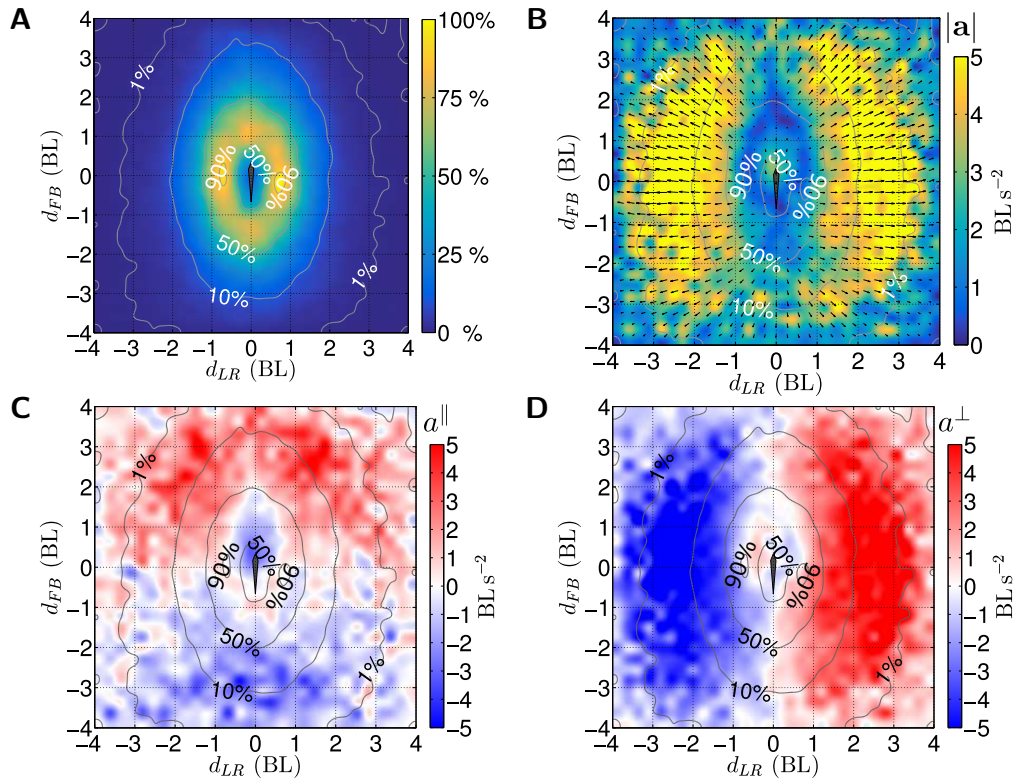

Figure 2: **Relative neighbour position density and interaction force (acceleration) maps for 18 zebrafish pairs.** Two dimensional histograms are constructed by discretising the area around a focal fish shown into a 30×30 grid of equal width bins (interpolated over 300×300 grid), accumulating values in the appropriate bins according the the location of a neighbour at each time sample, averaged over every focal-neighbour pair combination. (A) Probability of a neighbouring fish located at a given position relative to a focal fish at the origin, aligned with the y-axis (as per Fig. 1). Contours (all panels) indicate % density isolevels with respect to the most populated location bin. An exclusion region just larger than the shape of the focal fish depicted (grey polygon) is clearly shown, surrounded by a high density annular region. (B) Magnitude of focal fish acceleration response $|\mathbf{a}|$ as a function of the neighbour's position and vector field (black arrows) indicating size and direction of the response 'force' on the focal fish, relative to its orientation. (C) Tangential acceleration $a^\parallel$ of focal fish, as a function of neighbour position. Positive acceleration (red) indicate fish speeding up in its direction of motion, negative acceleration (blue) indicates fish slowing down. (D) Radial acceleration $a^\perp$ of focal fish, as a function of neighbour position. Positive accelerations are to the right (red) whilst negative accelerations are to the left (blue).

towards a neighbour on either side are much higher, most likely a consequence of a rapid change of orientation followed by a burst of forward motion.

In Fig. 2C, we report the tangential acceleration $a^{\parallel}$, indicating the forward, or axial speeding force response of a focal fish as a function of its neighbour's position. Data clearly highlights the repulsive region, extending approximately $0.8\,\mathrm{BL}$ to either side of the focal fish. Hence, the focal fish slows down ($a^{\parallel} < 0$) if its neighbour is less than $2\,\mathrm{BL}$ ahead of its position, and speeds up ($a^{\parallel} > 0$) if its neighbour is following less than $1\,\mathrm{BL}$ behind, presumably in both cases to avoid collisions. When neighbours are further away, fish accelerate to catch up with the neighbour when it is far ahead ($d_{FB} > 2\,\mathrm{BL}$), and decelerate when neighbours are further behind ($d_{FB} < 1\,\mathrm{BL}$). Outside of the repulsive region, the speeding force is found to be primarily dependent on the front-back distance d_{FB} and insensitive to the left-right separation d_{LR}. It is clear that our observations from this analysis support previous studies suggesting that speed regulation is an important mechanism for the interaction between small shoaling fish; one which should not be overlooked when describing a realistic model of their group behaviour[21, 22].

Spatial mapping of the radial acceleration $a^{\perp}$ (Fig. 2D) suggests the resultant lateral attraction and repulsion responses of a focal fish, a result of turning, as a function of its neighbour's position. This plot also reveals a pronounced repulsive region, surrounded by a wider region of attraction with a dependence primarily on the left-right separation d_{LR}. The repulsive region is concentrated just in front of the focal fish, characterised by accelerations in the opposite direction to neighbouring fish's position when it is closer than approximately $0.8\,\mathrm{BL}$ to either side. Beyond this distance however, focal fish's response is attractive - accelerating (radially) in the direction towards its neighbour, largely independent of their front-back separation d_{FB}.

2.3. Zebrafish response as a function of relative orientation

We now proceed by observing how focal fish acceleration components, $a^{\parallel}$ and $a^{\perp}$, vary as a function of spatial position, but also with respect to the pair's relative *orientation* ϕ_{ij} (Fig. 3). We also look for direct evidence of an alignment response by computing the angular acceleration $\dot{\omega}$, in addition to the resultant lateral attraction or repulsion described by $a^{\perp}$.

The response of the tangential acceleration $a^{\parallel}$ (Fig. 3A) as a function of the relative orientation ϕ_{ij} is similar to that observed in Fig. 2C. When conspecifics are well aligned, we find evidence of a slight increase in the front-back width of the (faintly) discernible repulsive region. At larger d_{FB} separations, the sign of $a^{\parallel}$ indicates attraction towards the neighbour independent of their relative orientation. Similarly, we find that the direction of the radial acceleration $a^{\perp}$ is always in the direction towards its neighbour, regardless of the orientation (Fig. 3C). Interestingly, and in contrast to our results for $a^{\perp}$, mapping the angular acceleration $\dot{\omega}$ as a function ϕ_{ij}, and either front-back (Fig. 3B), or left-right (Fig. 3D) separation, reveals a strong dependence on the relative orientation. Specifically, the angular acceleration is found to be in consistently the same sense of rotation which would be required to align the focal fish with its neighbour.

The results of this analysis suggest that whilst the tangential (forward) accelerations are strongly correlated with the relative position of a neighbour, zebrafish turning response is a function of both relative position (attraction / repulsion), and the specific orientation (alignment) of a neighbour. The histograms in Fig. 3B and Fig. 3D, where the angular acceleration

6

of the focal fish is mapped as a function of ϕ_{ij}, do not suggest a strong distance dependence of such an alignment interaction when data is averaged over either axis of separation individually.

Furthermore, by averaging over all pairwise samples (ignoring relative position), we can summarise the alignment interaction by plotting projection of $\dot{\omega}$ only as a function of ϕ_{ij} (Fig. 7C). The relationship we find is highly linear between $0°$ (fully aligned) and $\pm 90°$, with peak positive and negative accelerations occurring at $\phi_{ij} \approx \pm 120°$ respectively, decaying to $\dot{\omega} = 0$ as the pair become progressively anti-aligned ($\phi_{ij} \rightarrow \pm 180°$). As such, the sign (direction) of $\dot{\omega}$ varies with that of the relative orientation ϕ_{ij}, with an approximate relationship given by $\dot{\omega} \propto \sin \phi_{ij}$. These results, and those outlined in the following section, therefore reveal a more complex turning response than understood previously in [21] (for golden shiners), indicating *explicit* alignment interactions between conspecifics.
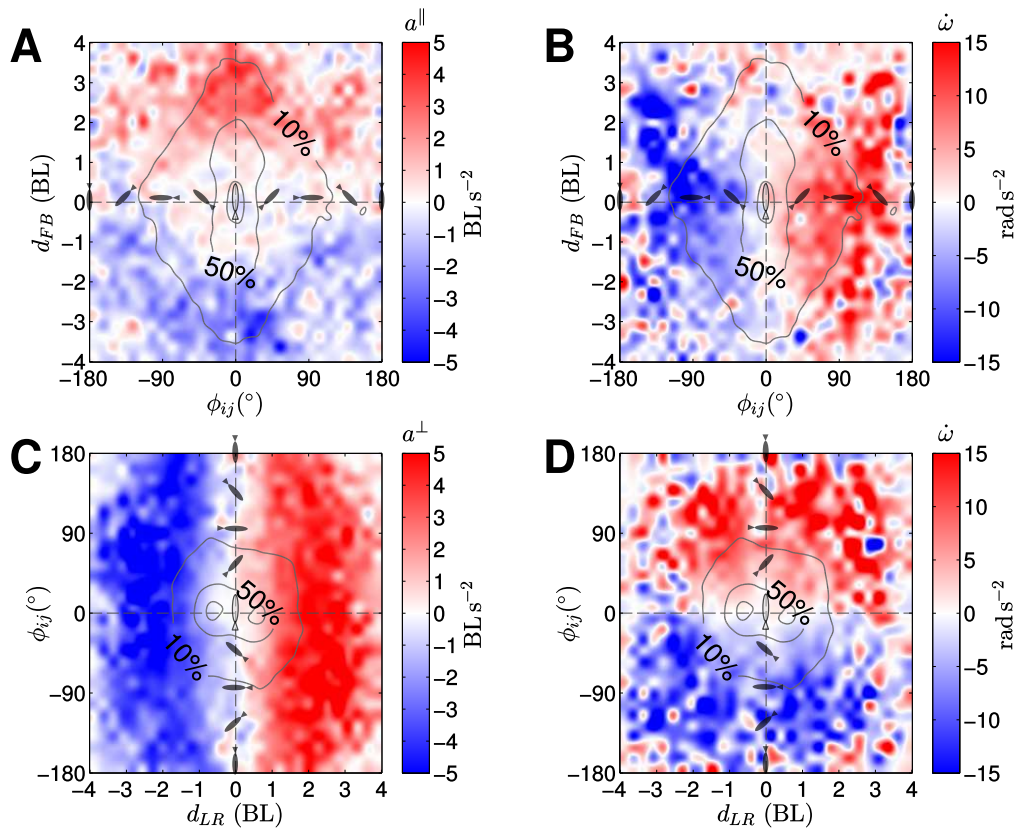

Figure 3: **Force mapping as a function of the relative heading angle and separation between a focal zebrafish and its neighbour.** (A) Tangential acceleration $a^{\parallel}$ and (B) angular acceleration $\dot{\omega}$ of the focal fish as functions of front-back displacement d_{FB} of the neighbour and its relative heading angle ϕ_{ij}. (C) radial acceleration $a^{\perp}$ and (D) angular acceleration $\dot{\omega}$ of the focal fish as functions of the left-right displacement d_{LR} of the neighbour and its relative heading angle ϕ_{ij}. Orientation of the neighbour fish is shown pictorially, with respect to the focal fish oriented along the positive y-axis at the centre of each panel. Contours show the relative population density of neighbours in a specific configuration. Red regions indicate tangential (forward) acceleration, radial accelerations to the right or angular accelerations in a clockwise direction. Blue regions correspondingly indicate either tangential deceleration, radial acceleration to the left, or anti-clockwise angular acceleration.

7

2.4. Spatial structure of attraction and alignment interactions

We investigate the spatial structure of the alignment and attractive interactions in more
detail by plotting separate spatial maps of the accelerations $\dot{\omega}$ and $a^{\perp}$ as functions of the
distances $[d_{FB}, d_{LR}]$ for subsets of the relative pair orientation ϕ_{ij}, grouped into the four
quadrants spanning $\phi_{ij} = [-\pi, \pi]$ (Fig. 4). Segregating the data in this way allows us to
disambiguate the positional and orientation dependencies, highlighting the different inter-
action responses which occur as a result of specific pair configurations. Interestingly this
analysis confirms our previous assertion that the spatial structure of the radial acceleration,
in terms of the relative position of the neighbour (Fig. 5), remains essentially invariant to the
relative orientation. Conversely, within the radius of interaction shown ($\pm 4\,\mathrm{BL}$) the angular
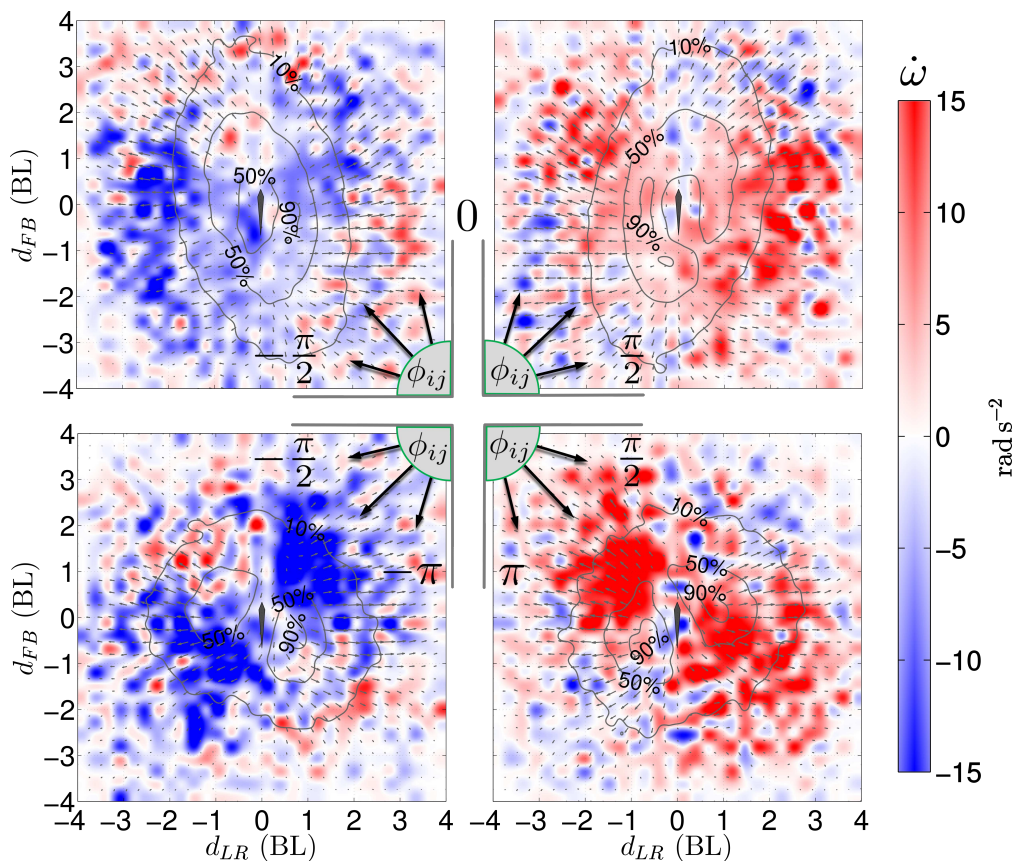acceleration depends primarily on the relative orientation, with only subtle variation due to

Figure 4: **Angular acceleration response of focal zebrafish as a function of neighbour position and relative orientation.** Histograms show the average angular acceleration $\dot{\omega}$ of the focal fish as it varies depending on the relative position of its neighbour. Panels show data isolated for ranges of relative heading angle ϕ_{ij} split across four quadrants: (top-left) $-\frac{\pi}{2} < \phi_{ij} \leq 0$, (top-right) $0 < \phi_{ij} \leq \frac{\pi}{2}$, (bottom-left) $-\pi < \phi_{ij} \leq -\frac{\pi}{2}$, (bottom-right) $\frac{\pi}{2} < \phi_{ij} \leq \pi$. Positive values of ϕ_{ij} indicate neighbour is rotated clockwise with respect to the focal fish. Positive angular accelerations (red) indicate increased (clockwise) turning to the right, negative angular accelerations indicate increased (anti-clockwise) turning to the left. Contours show isolevels of population density as percentages of the maximum bin value for each panel individually. Arrows indicate the vector field given by $[a^{\parallel}, a^{\perp}]$. In each quadrant we find that overall, the angular acceleration is such that the focal fish rotates in the direction required to align with the neighbour's orientation, indicated by arrows at each corner.
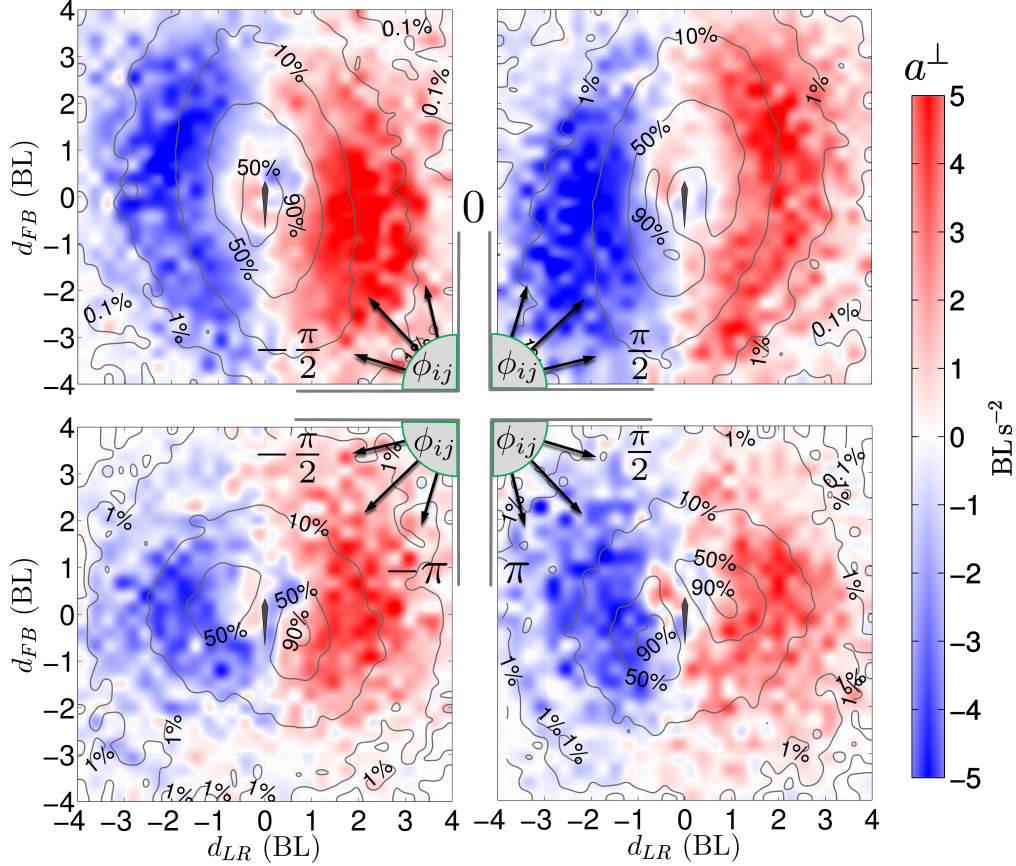
8

Figure 5: **Radial acceleration response of focal zebrafish as a function of neighbour position and relative orientation.** Histograms shows radial acceleration $a^\perp$ of the focal fish as it varies depending on the relative position of its neighbour. Panels description as per Fig. 4. Here, positive values of ϕ_{ij} indicate neighbour is rotated clockwise with respect to the focal fish. Positive radial forces (red) indicate increased acceleration to the right, negative radial forces indicate increased accelerations to the left.

the relative position (Fig. 4). Examining the $\dot{\omega}$ maps in more detail, we note that the spatial structure of the angular acceleration response is bilaterally symmetric as one would expect, i.e., it shows an equal and opposite alignment response, depending on whether the neighbour is rotated anti-clockwise (Fig. 4, left panels) or clockwise (right panels). For a more detailed description of this analysis, see online SI §S3.

2.5. Effects of forward speed on attraction, repulsion and alignment

Motivated by a similar analysis conducted by Katz *et al.* in [21], we further leverage the force mapping method to reveal how the forward speed of either fish affects the observed interaction responses.

The structure of the tangential acceleration $a^\parallel$ (Fig. 6A) suggests that the width of the repulsive region in the front-back direction increases proportionally to the speed of the focal fish u_f. We also find that attractive regions extend further both in front and behind the focal fish as speed increases, where the maximum acceleration achieved also becomes stronger with speed. Both of these observations seem intuitive in that a faster moving fish should increase its average distance between neighbours, and/or change its speed more rapidly to avoid
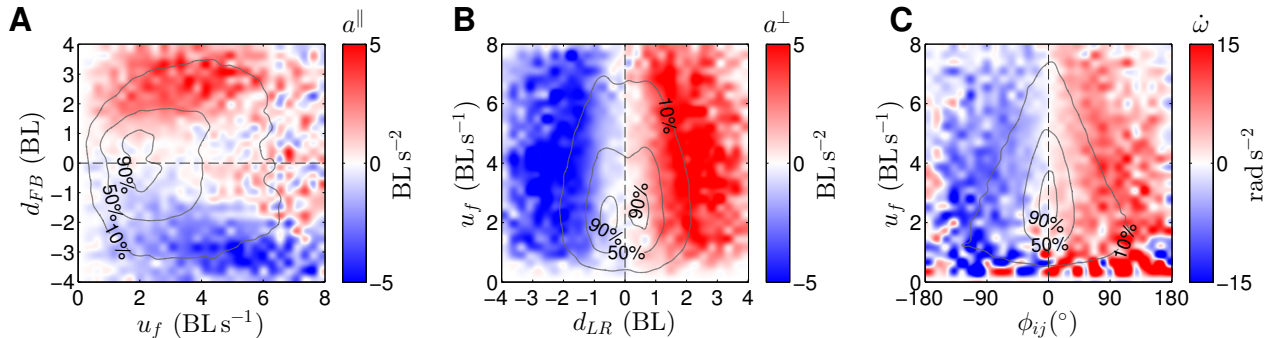
Figure 6: **Force mapping as a function of the forward speed of the focal zebrafish.** (A) tangential acceleration $a^{\parallel}$ as a function of front-back separation d_{FB} and speed of the focal fish u_f; (B) radial acceleration $a^{\perp}$ as a function of left-right separation d_{LR} and u_f; (C) angular acceleration $\dot{\omega}$ as a function of ϕ_{ij} and u_f. Contours show the population density of neighbours relative to the most common configuration.

collisions. 216

The effect of the fish's speed on radial acceleration $a^{\perp}$ (Fig. 6B) is less striking, where we 217 note only a slight decrease in the range of the attractive force as the speed increases. At low 218 speeds ($u_f < 1\,\mathrm{BL}^{-1}$) the angular acceleration (Fig. 6C) plotted as a function of the relative 219 orientation ϕ_{ij}, is found to be magnified, in line with our previous observations that high 220 speed turning is associated with lower forward speeds. 221

A confounding issue is that approximations of ω and its derivative $\dot{\omega}$ for the focal fish 222 are potentially less accurate at such low speeds and are both subject to high amplitude 223 fluctuations, making a reasonable interpretation of this result difficult (see online SI §S1.4). 224 Regardless, we note that the relative density of data points, indicated by the overlaid con- 225 tours, is skewed in the u_f axis, such that the distribution of samples becomes spread over a 226 larger range of ϕ_{ij} at lower speeds. This suggests that higher forward speeds are associated 227 with increased alignment of the interacting pair, a correlation also observed in groups of 228 golden shiners [38], giant danios [39], and barred flagtails [30]. 229

Additional analysis shows that for most observations, the pair separation $d_{ij}(t)$ is strongly 230 correlated with the mean forward speed of the pair $\bar{u}_{ij}(t)$ at time t, with changes in speed 231 found to lag those of the separation by approximately $0.14\,\mathrm{s}$ on average (see cross-correlograms 232 in Fig. S11 & Fig. S12 in the online SI). Supporting conclusions from the force maps described, 233 the latter observation also suggests the rapid modulation of swimming speed required to 234 prevent collisions and maintain close proximity. 235

3. Data-driven model of zebrafish shoals 236

In this section, we develop a modelling framework which captures the primary character- 237 istics of the individual locomotory patterns of zebrafish observed in experiments — further 238 incorporating the structure and dynamics of the various interaction behaviours which have 239 been discussed. Employing a bottom-up approach, we proceed by augmenting an existing 240 data-driven model of individual zebrafish locomotion [13], with coupled feedback terms (in- 241 teraction rules) which as far as possible, approximate the various dynamical relationships 242 which have been revealed earlier. 243

10

The proposed multi-agent model has been designed to include the following key features, inferred directly from the available experimental data: (i) autocorrelated, mean-reverting individual speed and turn-rate with joint distributions similar to those observed experimentally, (ii) wall-avoidance behaviour via boundary induced modulation of the turn-rate, (iii) attraction and repulsion to position of neighbours, governed by regulation of both forward speed and turning, and (iv) alignment with orientation of neighbours, governed by turn-rate regulation.

3.1. Individual model of zebrafish locomotion

A two-dimensional model describing the swimming dynamics of individual zebrafish was proposed in a previous study [13], in which we extended the so-called persistent turning walker (PTW) model presented by Gautrais *et al.* in [30, 40]. Specifically, our extended model uses two, coupled stochastic differential equations (SDEs), describing the evolution of both the forward speed $U(t)$, and the angular turn-rate $\Omega(t)$ of a random walker in the plane, according to:

$$dU = -\theta_u(U - \mu_u)dt + \sigma_u dW \tag{1a}$$

$$d\Omega = -\theta_\omega(\Omega - f_W)dt + f_c(U)dZ \tag{1b}$$

where we restrict the output values of U at any discrete time step t to be strictly greater than an empirical lower bound set at $U_{\min} = 10^{-6}\,\mathrm{cm\,s^{-1}}$ — ensuring physically realistic, forward only swimming. Both speed and (absolute) turn-rate values are saturated when they exceed the maximum realistic values $U_{\max} = 10\,\mathrm{BL\,s^{-1}}$ and $\Omega_{\max} = 20\,\mathrm{rad\,s^{-1}}$ respectively, in line with experimental observations. (An alternative approach to avoid using saturations has been recently presented in [15].)

Derived from the standard Ornstein-Uhlenbeck (OU) process, both equations in (1) exhibit mean reversion to an equilibrium value with an exponentially decaying autocorrelation (relaxation rate $\theta_{u/\omega}$). The equilibrium forward speed in (1a) is prescribed by a fixed parameter μ_u, whilst the equilibrium turn-rate in (1b) is nominally zero (unbiased turning) modulated by a time-varying value given by a wall avoidance function f_W. Random fluctuations are driven by independent Wiener processes dW and dZ, with variances proportional to the fixed parameter σ_u, and a speed-dependent coupling function f_c respectively.

Data from zebrafish trajectories, whether swimming in pairs as found here, or swimming in isolation [13], indicates that the range and variance of turn-rate decays (approximately) exponentially as a function of forward speed (see Fig. S13 for examples). To account for this, we define the coupling function f_c as:

$$f_c(U) = \alpha_c \exp(-\beta_c U) \tag{2}$$

describing an exponential decay as the speed U increases, with maximum amplitude α_c and decay parameter β_c. The parameters α_c and β_c can be extracted directly from experimental data using maximum-likelihood estimation (MLE) – see online SI §S5 for methodology.

The function f_W provides an empirical description of the interaction and collision avoidance behaviour observed for zebrafish as they approach a boundary [13]. Specifically, f_W describes a bias to the turn-rate as a function of the projected distance d_W, and incident

11

angle ϕ_W to the circular tank boundary, given the current position and velocity of the fish at any given sample. It is chosen as

$$f_W = \mathrm{sgn}(\phi_W)\alpha_W \exp\left(-\beta_W d_W\right) \tag{3}$$

where parameters α_W and β_W control respectively the strength and decay of the interaction as a function of the projected distance to the boundary. Again, both parameters can be estimated directly using the same MLE procedure.

3.2. Pair interactions and multi-agent model

The interaction model presented here is adapted from an existing framework developed in [30, 31, 41] for other species, where we tailor the behavioural rules based directly on the force mapping analysis presented in the previous section. Inspired by the simple functional form of the interactions in [30] which are introduced as perturbations to the equilibrium of the stochastic turn-rate process, we extend the same methodology to reproduce observed zebrafish responses via modulation of both the forward speed and turn-rate.

Interaction rules are encapsulated in two response functions $U_i^*(t)$ and $\Omega_i^*(t)$, which bias the equilibrium (time-averaged mean) values of the forward speed and angular velocity of fish i, modifying the existing stochastic equations of motion in (1) as follows:

$$dU_i = -\theta_u\left(U_i - \mu_u - U_i^*\right)dt + \sigma_u dW_i \tag{4a}$$

$$d\Omega_i = -\theta_\omega\left(\Omega_i - f_W - \Omega_i^*\right)dt + f_c dZ_i \tag{4b}$$

The response terms U_i^* and Ω_i^* are informed by the previous force mapping analysis, derived as functions which are dependent on the external stimuli due a neighbour, and to a lesser extent on the present internal state of a focal fish. External stimuli (neighbour interactions) in this model are restricted to (i) the relative position of the neighbour, expressed in polar coordinates with respect to position and heading of a focal fish: at a distance d_{ij} with angle θ_{ij}, and (ii) the relative orientation ϕ_{ij} between focal fish i and neighbour j (Fig. 1).

In general, for the set $\mathcal{N}_i$ of interacting neighbours of fish i, we define the interaction functions as a normalised linear superposition of pairwise contributions:

$$U_i^* = \frac{1}{|\mathcal{N}_i|\theta_u} \sum_{j \in \mathcal{N}_i} \underbrace{f_d\big(d_{ij}\big)}_{\text{distance-decay}} \underbrace{K_s\big[d_{ij} - r_u\big(U_i\big)\big]\cos\theta_{ij}}_{\text{attraction / repulsion}} \tag{5a}$$

$$\Omega_i^* = \frac{1}{|\mathcal{N}_i|} \sum_{j \in \mathcal{N}_i} f_d\big(d_{ij}\big) \left[\underbrace{K_p\frac{(d_{ij} - r_\omega)\sin\theta_{ij}}{U_i}}_{\text{attraction / repulsion}} + \underbrace{K_v\frac{\sin\phi_{ij}}{\theta_\omega}}_{\text{alignment}}\right] \tag{5b}$$

Here, $|\mathcal{N}_i|$ is the number of interacting neighbours of i, where in general, the set of individuals $\mathcal{N}_i$ contains the first-shell Voronoi neighbours of fish i (see online SI §S7).

Constants $K_s\,(\mathrm{s}^{-1})$, $K_p\,(\mathrm{rad\,s}^{-2})$, and $K_v\,(\mathrm{rad\,s}^{-2})$ define a set of tunable gain parameters which modify the strength of each of the interaction types, namely: speed induced attraction (and repulsion), turning induced attraction (and repulsion), and alignment. In contrast to
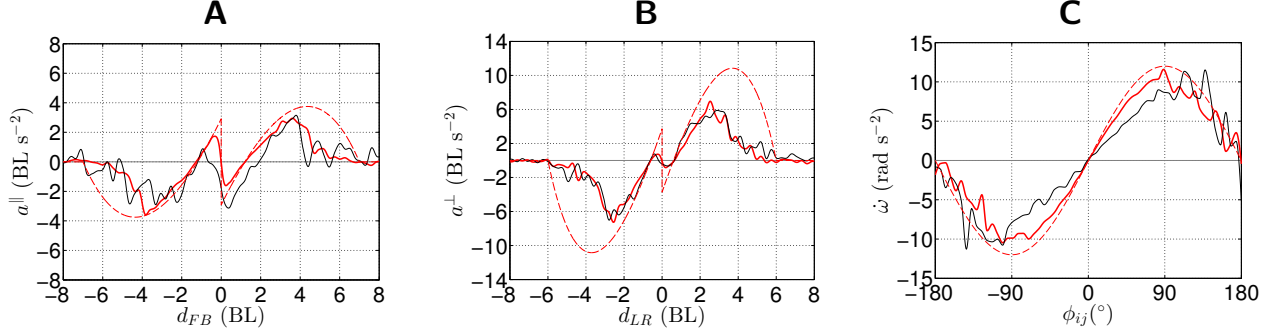
Figure 7: **Axial force projections - comparing experimental and simulated data** (A) Projection of the tangential acceleration $a^{\parallel}$ in the $d_{LR} = 0$ axis, parallel to the focal fish's direction of motion. (B) Projection of the radial acceleration $a^{\perp}$ in the $d_{FB} = 0$ axis, perpendicular to the direction of motion. (C) Angular acceleration $\dot{\omega}$ as a function of the relative heading angle ϕ_{ij} between focal fish i and neighbour j. Experimental data computed for 18 zebrafish pairs (black) is compared with data from 18 ($18 \times 20\,\mathrm{min}$) simulated realisations of the model (solid red). Model acceleration functions used in (5a), (5b) are shown in panels A and B respectively (red dashed) for nominal interaction parameter set, assuming $\phi_{ij} = 0$ and $U_i = \mu_u$. Model angular acceleration from (5b) is shown in panel C (red dashed).

recent models [30, 31], we also prescribe explicit repulsion through the parameter r_ω and the function $r_u(U)$ that accounts for variation in repulsion zone in response to speed variations.

The radius of the repulsive region r_u can be estimated directly from the time-averaged spatial force map in Fig. 2C, or more precisely from the axial projection in Fig. 7A as the (absolute) value of d_{ij} or d_{FB} respectively, where $a^{\parallel}$ passes through zero. However, our observations in Fig. 6 indicate that the radius of the repulsive region is strongly dependent on the speed of the focal fish $U_f \equiv U_i(t)$ at time t, increasing in diameter as the speed increases. Therefore we choose

$$r_u\big(U_i(t)\big) = r_{u0}\frac{U_i(t)}{\mu_u} \tag{6}$$

that describes a linear increase of the repulsion zone as a function of the speed from its nominal value r_{u0} at the mean speed.

In addition, we introduce two decay functions $f_{d,u}$ and $f_{d,\omega}$ to attenuate long-range interactions as a function of the pair separation d_{ij}. The two functions are chosen to share the same functional form given by

$$f_{d,u/\omega} = \begin{cases} 1 - \exp\left[(d_{ij} - \delta_{u/\omega})/\lambda_{u/\omega}\right], & \text{if } d_{ij} < \delta_{u/\omega} \\ 0, & \text{otherwise.} \end{cases} \tag{7}$$

where the parameters $\delta_{u/\omega}$ and $\lambda_{u/\omega}$ are chosen to match the experimental observations for the speed and turning interaction respectively.

The functional form of the speed response in (5a) is informed directly from the spatial mapping shown in Fig. 2C, such that we derive a comparable potential field for the tangential acceleration as a function of polar coordinates (d_{ij}, θ_{ij}). Specifically, we find that the spatial structure of the experimental tangential acceleration, $a^{\parallel}$, is symmetric in the $d_{LR} = 0$ axis, and approximately symmetric but with opposite sign in the $d_{FB} = 0$ axis. From this, we infer a response function which is maximised along the d_{FB} axis, with an amplitude modulated

13

by $\cos\theta_{ij} \propto d_{FB}$. Based on the projection of $a^{\parallel}$ in the $d_{LR} = 0$ axis (Fig. 7A), we choose the model function in (5a) (see Fig. 7 for its validation on the experimental data).

With respect to the attraction/repulsion term in (5b), we follow a similar line of argument based on the spatial force mapping in Fig. 2D, and the projection in Fig. 7B. Note that to match the experimental observations we scale this term by the speed of the focal fish $U_i(t)$ – see relationship derived in SI §S2.

The alignment term in (5b) is inspired from that used in the original PTW model in [30], to estimate the dependence of the angular acceleration $\dot{\omega}_i$ as a function of the relative pair orientation ϕ_{ij} – capturing the observed relationship (Fig. 3B,D) and Fig. 7C.

Unlike the PTW model described in [24, 31], we do not include an angular weighting to the turning (or speeding) response to bias the interaction in favour of neighbours in front of the focal fish (visual region), finding insufficiently strong evidence for this from our force mapping analysis. We also do not specify a speed dependence on the alignment term since, due to the coupling function f_c, we already expect faster moving fish to have lower turn-rate variance thus encouraging polarisation (aligned swimming).

We emphasise that whilst the first term (radial attraction/repulsion) in (5b) varies proportionally with the separation distance d_{ij}, the second term (alignment) does not. The combined interaction allows for a distance-dependent weighting between dominant alignment at short separation distances, with attraction dominating as the distance increases. This model description, as noted in [30], provides a continuous transition between alignment and attraction, in contrast to 'zonal' models, e.g.,[42], in which dominant behaviour is effectively switched beyond a prescribed (radial) distance. The effect of this smooth transition is demonstrated by plotting the potential force fields due to the tangential (U^*) and radial (Ω^*) acceleration terms in the model, shown in Fig. S14, and the (semi-spatial) force maps in Fig. S15. The same transition between attraction and alignment is also demonstrated by evaluating spatial force maps for $\dot{\omega}$ (Fig. S16).

4. Model calibration and validation

In the spirit of the data-driven approach we adopt for this study, the parameters of the proposed model were, as far as possible, determined directly from the experimental data obtained from observations of swimming zebrafish pairs. For a complete description of the calibration procedures, including maximum-likelihood estimation, we refer the reader to the online SI. For brevity, we present here only the set of nominal parameter values used for further numerical simulations described in this study.

The model described in the previous section is defined by two sets of parameters, those characterising the dynamics of an individual's motion, including wall avoidance behaviour (Tab. 1), and those which measure the interactions between conspecifics (Tab. 2).

We proceed by performing a force mapping analysis of simulated trajectory data. Synthetic trajectories were generated from 18 independent simulations of interacting, homogeneous pairs. Trajectories were simulated for $20\,\text{min}$ of real time, generated at a frequency of $30\,\text{Hz}$, and with randomised initial conditions (see online SI §S4). The total number of samples obtained is therefore identical to that of the experimental data set. Similar analysis was performed using heterogeneous parameters for each fish, calibrated separately on each of

14

Table 1: **MLE calibrated parameters for individual zebrafish model**

Description	Symbol	Unit	Value
SDE parameters			
equilibrium speed	μ_u	$\mathrm{cm\,s^{-1}}$	**11.42**
speed variance	σ_u	$\mathrm{cm\,s^{-3/2}}$	**2.59**
speed mean-reversion rate	θ_u	$\mathrm{s^{-1}}$	**0.21**
turn-rate coupling amplitude	α_c	$\mathrm{rad\,s^{-3/2}}$	**11.81**
turn-rate coupling decay	β_c	$\mathrm{s\,cm^{-1}}$	**0.11**
turn-rate mean-reversion rate	θ_ω	$\mathrm{s^{-1}}$	**3.58**
wall-avoidance amplitude	α_W	$\mathrm{rad\,s^{-1}}$	**5.00**
wall-avoidance decay	β_W	$\mathrm{cm^{-1}}$	**0.15**

Table 2: **Nominal pair interaction parameters.**

Description	Symbol	Unit	Value
Interaction parameters			
Tangential force gain	K_s	$\mathrm{s^{-1}}$	**4**
Radial force gain	K_p	$\mathrm{rad\,s^{-2}}$	**6**
Alignment force gain	K_v	$\mathrm{rad\,s^{-2}}$	**12**
Speed modulated repulsion (mean) radius	r_u	cm	**3.6**
Turning modulated repulsion radius	r_ω	cm	**1.8**
Speed interaction cut-off distance	δ_u	cm	**21**
Turning interaction cut-off distance	δ_ω	cm	**18**
Speed distance decay	λ_u	cm	**22.5**
Turning distance decay	λ_ω	cm	**6**

the 18 observations (see Fig. S17), where we found no significant differences to the composite force mapping results.

The plots in Fig. 8 show the density and linear ($a^\parallel$ and $a^\perp$) force mappings, obtained as an averaged composite for each fish pair. Specifically, we take each fish in turn as the focal fish for every pair, and accumulate data from all pairs by taking an average force value at each discretised relative position coordinate. These plots can be compared directly to those extracted from experimental zebrafish data, presented earlier (Fig. 2).

Considered separately, the simulated tangential force $a^\parallel$ (Fig. 8C) and radial force $a^\perp$ (Fig. 8D) maps match extremely well with the experimental ones (Figs. 2C & 2D respectively). The characteristic circular repulsion regions around the origin are clearly visible, beyond which we find the attractive regions. Therein, forces vary in magnitude as a function of the neighbour's position, as prescribed by model potential fields for U^* and Ω^* (Fig. S14).

The spatial structure of linear accelerations close to the focal fish ($d_{FB}, d_{LR} < 2\,\mathrm{BL}$) is examined in more detail, by comparing the magnitude $|\mathbf{a}|$ for experimental data (Fig. 9A), to the model predictions (Fig. 9B), and dynamic simulations (Fig. 9C).

The plots in Fig. 10 report the semi-spatial force maps obtained using the same method adopted previously for experimental data (Fig. 3). From the 18 simulated pairs, we compute mappings for linear accelerations $a^\parallel$ and $a^\perp$, and angular acceleration $\dot{\omega}$, as functions of
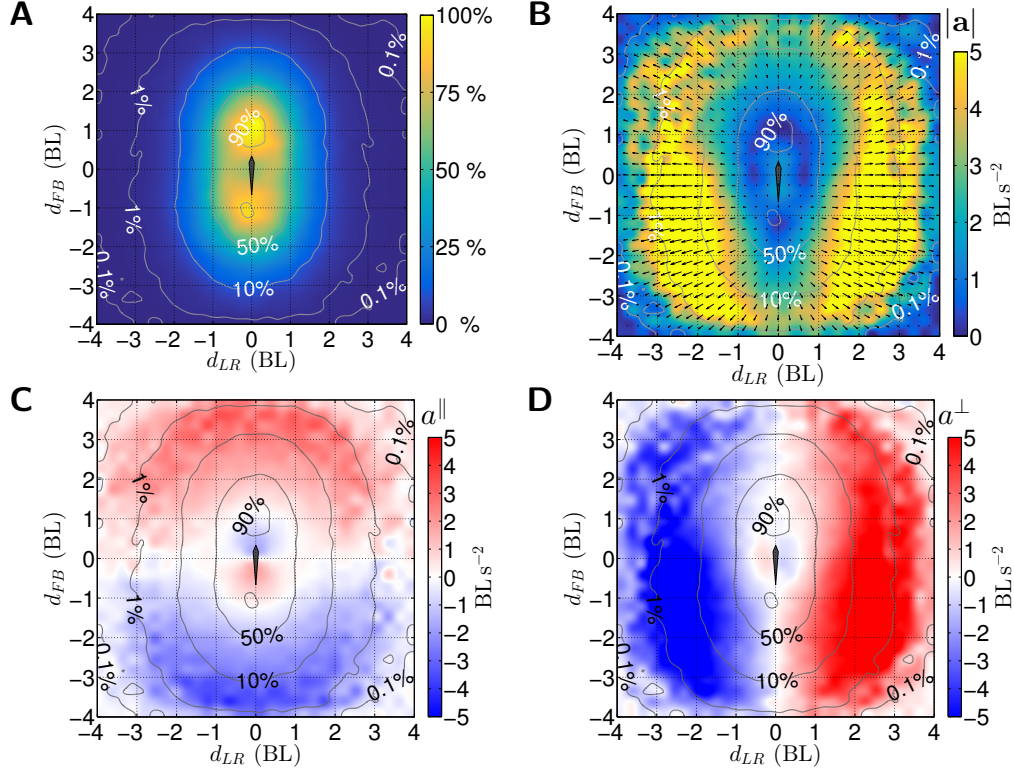
Figure 8: **Relative neighbour position density and force maps for simulated fish pairs.** Data obtained from 18×20 min independent realisations of model with 2 interacting fish simulated with nominal parameters in Tabs. 1 & 2. Histogram construction as per Fig. 2. Panels show: (A) relative position density. (B) Magnitude of focal fish acceleration response $|\mathbf{a}|$ with vector field $[a^{\parallel}, a^{\perp}]$ (arrows). (C) Tangential acceleration $a^{\parallel}$ of focal fish. (D) Radial acceleration $a^{\perp}$ of focal fish. Positive accelerations indicate translations or turns right/clockwise (red) whilst negative accelerations are to the left/anti-clockwise (blue). Contours indicate 0.1, 1, 10, 50 and 90% density isolevels with respect to the most populated location bin.
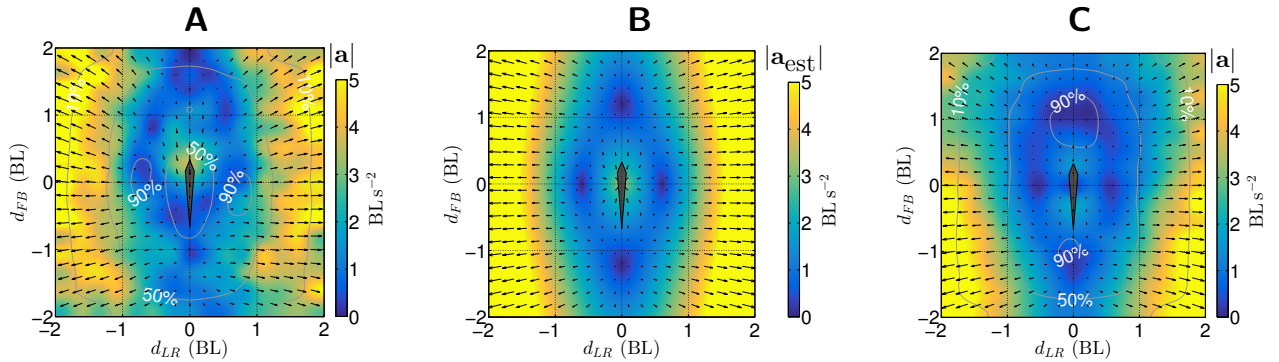

Figure 9: **Acceleration response maps within $\pm 2\,\mathrm{BL}$ of focal fish.** Close up mapping of focal fish acceleration response as a function of neighbours position for (A) experimental zebrafish data, (B) predicted force magnitude $|\mathbf{a}_{\mathrm{est}}|$ from equations for U^* and Ω^* with nominal parameters, and (C) simulated (dynamic) realisations of fish pairs using nominal parameters. In each panel, the magnitude of the linear acceleration $|\mathbf{a}|$ is plotted as heatmap with its components $a^{\parallel}$ and $a^{\perp}$ in the focal fish frame used to construct vector field (arrows).

orthogonal separation distances (d_{FB} or d_{LR}), and the relative orientation ϕ_{ij}. Overall we find that the characteristic features of each force map are qualitatively similar to those evaluated for the experimental data — with more specific observations described in what follows.

Force maps in Figs. 10A & 10B report respectively the tangential acceleration $a^{\parallel}$, and the angular acceleration $\dot{\omega}$ as functions of the front-back separation d_{FB}, and the relative orientation ϕ_{ij}, averaged over values of the left-right separation d_{LR}. Here, we find that the speed response ($a^{\parallel}$) varies primarily as a function of d_{FB}. However, similar to the experimental mapping (Fig. 3A), we also find the range and magnitude of the repulsive interaction to be more pronounced when the pair are well aligned. Note that this behaviour is not prescribed explicitly in the model description but emerges from its simulation.

In terms of the angular acceleration $\dot{\omega}$ (Fig. 10B), we find values are primarily dependent on the relative orientation such that the direction of increasing rotation is always to restore alignment between the pair, as found for experimental data (Fig. 3B). Only the magnitude of the angular acceleration component is found to vary as a function of the pair separation, as prescribed by the distance decay term $f_{d,\omega}$ in the model, as per (5b) and (7).
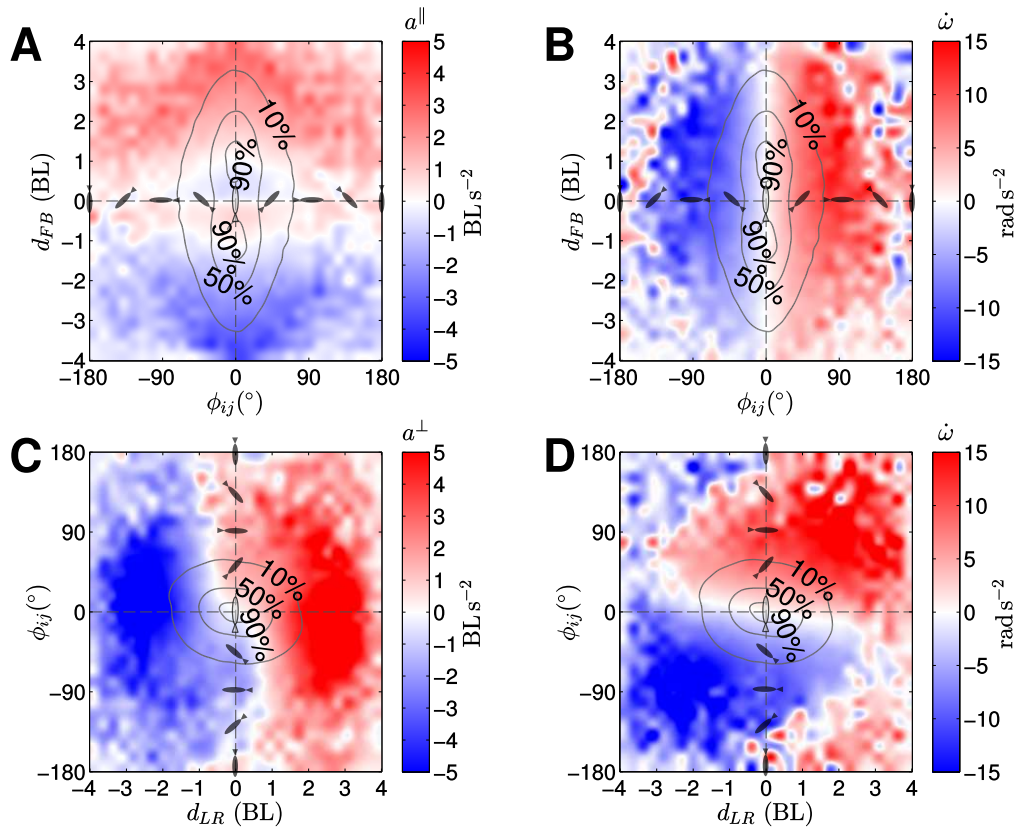

Figure 10: **Force mapping as a function of the relative heading angle and separation between simulated conspecifics.** Panel descriptions as per Fig. 3. Force maps show significant characteristics of both (A) tangential $a^{\parallel}$, and (C) radial $a^{\perp}$ attraction and repulsion in response to relative position of neighbour, with only marginal dependence on the relative orientation. Force maps for $\dot{\omega}$ in (B) and (D) however, indicate strong angular acceleration dependence on relative orientation indicating active alignment between conspecifics, as described by the model

17

Analysis of experimental data indicated that resultant radial accelerations (Fig. 3C) are largely independent of the relative orientation ϕ_{ij}, whilst the observed angular acceleration $\dot{\omega}$ (Fig. 3D) are dependent only on ϕ_{ij}. Both of these features are well captured overall in respective force mappings for simulated pair trajectories shown in Figs. 10C & 10D.

The overall dependence of the angular acceleration on ϕ_{ij}, averaging over all positions of the neighbour (spatial maps in Fig. 10B & 10D) is compared against experimental data in Fig. 7C. Based on this simplified projection, in conjunction with the axial projection of $a^{\perp}$ (Fig. 7B), we find that the model is able to simultaneously capture both the angular and linear components of the turning response, including the observed repulsive region, with a high degree of accuracy.

More specifically, we find that increasing the relative strength of the alignment interaction by adjusting K_v in (5b), provides better matching of the $\dot{\omega}$ map in Fig. 10D with the experimental equivalent. Unfortunately, exaggerating the alignment response in this way negatively impacts the observed radial acceleration plot (Fig. 10C), which becomes increasingly dominated by changes in the relative orientation ϕ_{ij}. For comparison, a similar analysis (see Fig. S6 in the SI) was conducted on simulated trajectories with no explicit alignment behaviour ($K_v = 0$). There, we find that the radial acceleration becomes entirely uniform with respect to orientation, comparably better with respect to experimental data. However, the resulting angular acceleration response with respect to front-back separation is essentially flat (zero everywhere), responding only to left-right separation due to residual radial attraction ($a^{\perp}$) with no dependence on ϕ_{ij}. These results indicate that an *explicit* alignment response is required to reproduce the angular accelerations observed experimentally for zebrafish.

Further evidence supporting our choice of interaction model, prescribing a continuous weighting between radial attraction and alignment, is obtained by comparing the spatial structures of accelerations for different neighbour orientations. Panels in Fig. S2 & Fig.S3 (online SI) report results of the same analysis we performed for zebrafish data as per Figs. 4 & 5, in which we compute spatial (d_{LR}, d_{FB}) mappings for simulated conspecifics, separately across four angle quadrants of relative orientation ϕ_{ij}. For angular accelerations $\dot{\omega}_i$ (Fig. S2.B), we find alignment interactions dominate in a region of approximately $\pm 2\,\mathrm{BL}$ around the focal agent, such that it turns to align its heading direction with respect to the neighbour, irrespective of its relative position. As the separation increases however, attraction dominates such that the focal agent turns towards the neighbour, irrespective of its orientation.

Similar to our experimental observations, the direction (sign) of the angular acceleration $\dot{\omega}$ is found to change depending on the sign of the orientation ϕ_{ij}. For radial accelerations however, the sign of $a^{\perp}$ at any particular position is (almost) independent of ϕ_{ij}, indicating changes to the perpendicular translation speed of the fish, — e.g. beyond the repulsion zone, it is always attractive with respect to the neighbour's position. However, unlike our experimental observations, the magnitude of the radial accelerations are noticeably reduced when agents are anti-aligned (Fig. S3.B, bottom panels). Although the dynamics of the model dynamics does not recover all of the subtleties observed for zebrafish, these mappings further demonstrate its ability to capture the fundamental features of both attraction and alignment as functions of both the location and orientation of a neighbour. Again, these features are put into perspective when performing the same analysis for model realisations without explicit alignment ($K_v = 0$) — shown in Fig. S7. In those simulations we find that angular acceleration is, predictably, a function only of the neighbour's position where the
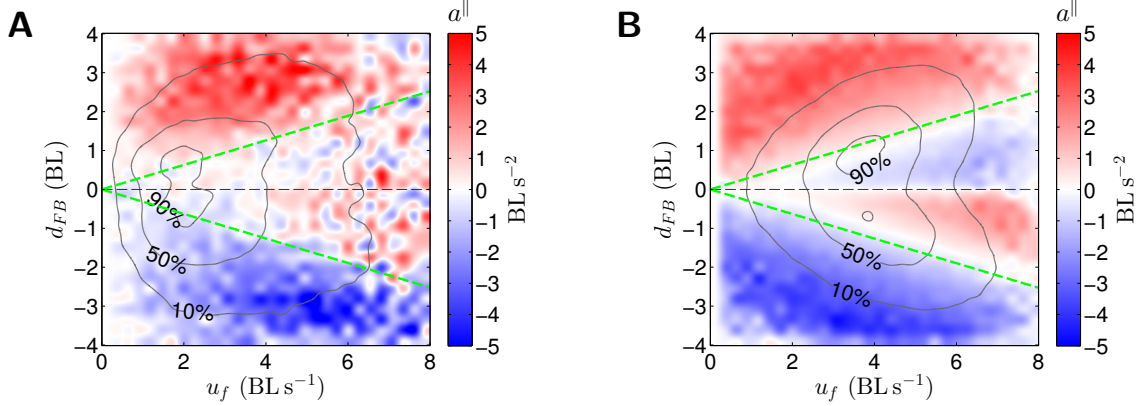
18

Figure 11: **Speed dependent repulsion.** Force maps shown for tangential acceleration $a^{\parallel}$ as a function the front-back distance d_{LR}, and the focal fish speed u_f and U_f, respectively for (A) experimental zebrafish data, and (B) simulated pairs. The speed dependent repulsion radius $\tilde{r}_u = \pm r_u \left(U_i(t)/\mu_u\right)$, estimated from experimental data and prescribed in the model, is shown in green for nominal parameter value $r_u = 3.6\,\mathrm{cm}$ (1.2 BL)

structure (normalised values) of all mappings shown for $\dot{\omega}$ and $a^{\perp}$ are qualitatively identical. 422

The final force-map comparison presented in this analysis quantifies the effect of the 423 focal agent's forward speed on the dynamics of interactions. In particular, we demonstrate 424 the effects of regulating the repulsion radius r_u of the tangential acceleration as function 425 of forward speed $U(t)$, as per (6). Here, we compare mappings for $a^{\parallel}$ values computed 426 as a function of focal fish speed, and the front-back separation distance d_{LR} — for both 427 experimental (Fig. 11A) and simulated data (Fig. 11B). Results obtained from dynamical 428 simulation clearly indicate the linear speed dependence defined in the model. 429

Force maps for both radial and angular acceleration responses due to the speed of the 430 focal agent are presented in Fig. S18). As found for zebrafish, the radial acceleration com- 431 ponent is essentially invariant to the speed. Similarly, we find no obvious speed dependence 432 on the magnitude of angular accelerations $\dot{\omega}$. Importantly however, the narrowing width of 433 isodensity contours for simulated data (Fig. S18C) suggests that pair alignment, or polarisa- 434 tion, is more likely as speed increases. Although this effect is not found to be as pronounced 435 as observed in experimental data, it is still an interesting and desirable feature of the model 436 proposed. 437

5. Comparative collective dynamics of small shoals 438

The force mapping analysis conducted for calibrated model realisations suggests that 439 the model successfully captures many of the interactions, previously observed for live ze- 440 brafish pairs. In what follows, we extend our comparisons by considering how these localised 441 (individual-level) interaction behaviours lead to aggregate collective states in simulated and 442 experimental shoals. Here, we draw direct comparisons between experimental and simulated 443 dynamics in terms of the emergent collective behaviour — quantified using a set of global 444 observables, measured at each time sample. To provide a comprehensive analysis, we also 445 simulated interacting populations of five individuals, and compared their collective dynamics 446 to experimental trajectory data obtained for five zebrafish shoals in [43]. 447
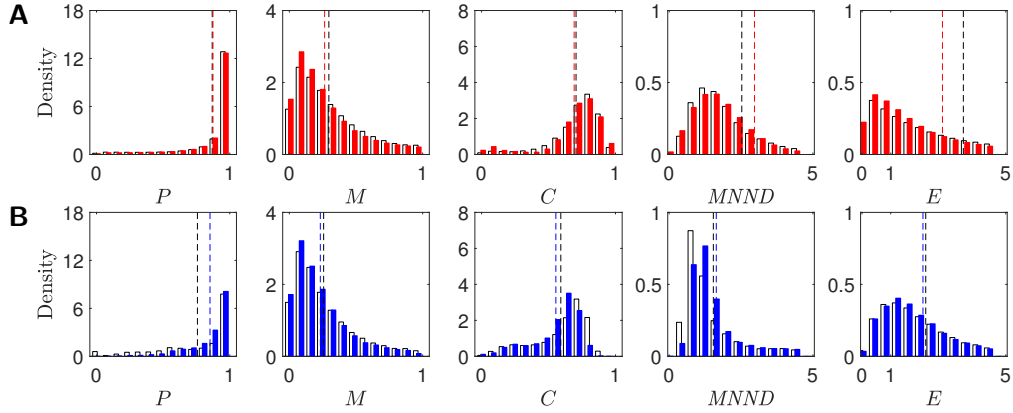
19

Figure 12: **Comparing experimental and simulated distributions of global observables** Experimental distributions (grey) are compared with those for simulated data with: (A) two fish (red), and (B) five fish (blue). Nominal model parameters (Tabs. 1 & 2) are used for both simulated groups, but where for (A) alignment strength is reduced: $K_v = 8$, and in (B) increased: $K_v = 14$, to yield better comparisons for some distributions. From left to right, histograms report: (P)olarisation, (M)illing, (C)ohesion, Mean nearest-neighbour distance ($MNND$), and (E)longation. Mean values shown by vertical dashed lines. *Data for five-fish shoals was gathered under identical conditions, selected from a set of control trials in* [43]

Specifically, we infer the relative persistence of either polarised (P) or rotational milling (M) dynamical states, as well the relative group cohesion (C) based on each individual's distance from the shoal centre of mass (where $P, M, C \in [0,1]$). In addition to polarised and rotational aggregate states, we also compute observables measuring the mean nearest-neighbour distance ($MNND$), and the shoal elongation (E). Mathematical derivations and descriptions for each observable can be found in §S8 of the SI.

The collective behaviour of fish shoals, as with other animal groups, are found to transition between different states which may persist for long periods of time, or exist only for brief periods before dissipating. Perturbations within a highly polarised ($P \approx 1, M \approx 0$) school may for example, result in a transient milling (rotating) state ($M \to 1, P \to 0$), before reorganising into a well polarised configuration. For this reason, we capture the evolution of transient dynamical states over extended periods by computing the time-series distributions of each global observable.

We simulated trajectories ($18 \times$ 20 min, $F_s = 30$ Hz) for both two-, and five-fish groups, parametrised using the nominal, homogeneous set of individual parameters obtained via MLE (Tab. 1), and interaction parameters estimated via force-mapping analysis (Tab. 2). For two fish simulations however, we found polarisation to be exaggerated — with a corresponding reduction in the propensity for milling configurations. To compensate for this, we reduced the relative propensity of individuals to align by simulating model realisations with a weakened alignment interaction strength by setting $K_v = 8$ for fish pairs. Similarly for five-fish shoals, good agreement was obtained when setting $K_v = 14$. Animated visualisations of two- and five-fish simulated shoals can be found in the online SI: videos V2 & V3 respectively.

Distribution histograms for each observable are shown in Figs. 12A and Figs. 12B with comparison to the corresponding experimental values (denoted by grey bars).

Overall, our findings display remarkable similarities between the distributions measured for experimental and simulated data for both fish shoals. By comparing experimental data

for both the two- and five-fish populations, we find mean values for group cohesion (C), mean nearest neighbour distance ($MNND$), and shoal elongation (E) are all noticeably lower in the five fish group — also reflected in simulated data. From the cohesion (C) distribution in particular, we note that for zebrafish and simulated pairs, there is a well defined peak corresponding to a stable, equilibrium separation between individuals. The heavy left-sided tail represents brief periods in which the two fish in the pair become separated. Both experimental and simulated data for the five fish groups however, show a flattened, almost bimodal C distribution, with evidence of a second, much smaller peak at $C \approx 0.25$. Further analysis of the experimental $C(t)$ and $M(t)$ time-series data for these shoals, suggests this additional peak corresponds to the average value of cohesion when the shoal exhibits transient milling behaviour (see Fig. S19). The primary peak ($C \approx 0.7$) corresponds to the average value of cohesion when the fish are swimming with sustained high polarisation. Importantly, this subtle bimodal distribution is also evident in simulated data for the same reasons.

For both populations, we find that judicious adjustment of the parameter K_v regulating alignment strength may be used to promote, or inhibit, polarised and rotational collective phases. However, in conjunction with the previous force-mapping analysis, it is clear that further tuning of the model parameters depends on what features of the experimental data need to be captured with higher priority. Crucially, our results demonstrate that the model is able to reproduce both the individual level interaction responses, and emergent collective dynamics of multiple fish swimming together as a shoal. Similar analysis of collective dynamics for simulations in which we selectively remove individual interaction responses (via K_s, K_p, and K_v) can be found in Fig. S8.

6. Summary

In this work, we have explored the dynamic structure of zebrafish interactions at the individual-level by analysing their movement patterns in response to a neighbour. The observed interaction behaviours include dynamic forward speed regulation, yielding both attractive and repulsive interactions with respect to the relative position of the conspecifics. Turning responses, interpreted from both the radial and angular acceleration components, were found to be more complex; consisting of distance mediated attraction, repulsion and alignment behaviours. In contrast to previous studies of golden shiners [21], we found strong evidence that the alignment response between conspecifics is in fact an explicit component of zebrafish interaction, rather than a purely emergent phenomenon.

The social force mappings revealed from data analysis were used to derive a novel model framework which encapsulates both the unique locomotory patterns of individual zebrafish, and a detailed description of the interactions between pairs. Data-driven methods were used to calibrate and verify the consistency of the multi-agent model with respect to experimental observations. In particular, a set of mean model parameters was derived able to reproduce key features of both the individual-level interaction behaviours, and the emergent collective dynamics of small zebrafish shoals.

21

[1] C. Maximino, T. M. de Brito, A. W. da Silva Batista, A. M. Herculano, S. Morato, A. Gouveia, Measuring anxiety in zebrafish: A critical review, Behav. Brain Res. 214 (2) (2010) 157–171.

[2] A. V. Kalueff, J. M. Cachat (Eds.), Zebrafish models in neurobehavioural research, Humana Press, 2011.

[3] A. V. Kalueff, A. M. Stewart, R. Gerlai, Zebrafish as an emerging model for studying complex brain disorders., Trends Pharmacol. Sci. 35 (2) (2014) 63–75.

[4] M. B. Orger, G. G. de Polavieja, Zebrafish Behavior: opportunities and challenges, Ann. Rev. of Neurosci. 40 (1) (2017)

[5] C. Lawrence, The husbandry of zebrafish (*Danio rerio*): A review, Aquaculture 269 (1-4) (2007) 1–20.

[6] P. Panula, Y. C. Chen, M. Priyadarshini, H. Kudo, S. Semenova, M. Sundvik, V. Sallinen, The comparative neuroanatomy and neurochemistry of zebrafish CNS systems of relevance to human neuropsychiatric diseases, Neurobiol. Dis. 40 (1) (2010) 46–57.

[7] A. V. Kalueff, M. Gebhardt, A. M. Stewart, J. M. Cachat, M. Brimmer, J. S. Chawla, C. Craddock, E. J. Kyzar, A. Roth, S. Landsman, S. Gaikwad, K. Robinson, E. Baatrup, K. Tierney, A. Shamchuk, W. Norton, N. Miller, T. Nicolson, O. Braubach, C. P. Gilman, J. Pittman, D. B. Rosemberg, R. Gerlai, D. Echevarria, E. Lamb, S. C. F. Neuhauss, W. Weng, L. Bally-Cuif, H. Schneider, Towards a comprehensive catalog of zebrafish behavior 1.0 and beyond., Zebrafish 10 (1) (2013) 70–86.

[8] S. Butail, T. Bartolini, M. Porfiri, Collective response of zebrafish shoals to a free-swimming robotic fish, PLoS One 8 (10) (2013) e76123.

[9] L. A. A. Fuiman, P. W. W. Webb, Ontogeny of routine swimming activity and performance in zebra danios (*Teleostei: Cyprinidae*), Anim. Behav. 36 (1) (1988) 250–261.

[10] F. E. Fish, J. F. Fegely, C. J. Xanthopoulos, Burst-and-coast swimming in schooling fish (*Notemigonus crysoleucas*) with implications for energy economy, Comp. Biochem. Physiol. Part A Physiol. 100 (3) (1991) 633–637.

[11] U. K. K. Muller, E. J. J. Stamhuis, J. J. J. Videler, Hydrodynamics of unsteady fish swimming and the effects of body size: comparing the flow fields of fish larvae and adults, J. Exp. Biol. 203 (2000) 193–206.

[12] N. Danos, G. V. Lauder, The ontogeny of fin function during routine turns in zebrafish (*Danio rerio*)., J. Exp. Biol. 210 (Pt 19) (2007) 3374–86.

[13] A. K. Zienkiewicz, D. A. W. Barton, M. Porfiri, M. Di Bernardo, Data-driven stochastic modelling of zebrafish locomotion, J. Math. Biol. 71 (2014) 1081–1105.

[14] V. Mwaffo, R. P. Anderson, S. Butail, M. Porfiri, A jump persistent turning walker to model zebrafish locomotion, J. R. Soc. Interface 12 (102) (2014) 20140884.

[15] V. Mwaffo, S. Butail, M. Porfiri, In-silico experiments of zebrafish behaviour: modeling swimming in three dimensions, Sci. Rep. 7 (January) (2017) 39877.

[16] H. Yoshioka, Mathematical analysis and validation of an exactly solvable model for upstream migration of fish schools in one-dimensional rivers, Mathematical Biosciences 281 (2016) 139–148.

[17] D. S. Calovi, A. Litchinko, V. Lecheval, U. Lopez, A. P. Escudero, H. Chaté, C. Sire, G. Theraulaz, Disentangling and modeling interactions in fish with burst-and-coast swimming, arXiv (2017) 1–12`arXiv:1703.03801`.

[18] V. Lecheval, L. Jiang, P. Tichit, C. Sire, C. K. Hemelrijkm, G. Theraulaz, Domino-like propagation of collective U-turns in fish schools, bioRxiv`doi:10.1101/138628`.

[19] A. Filella, F. Nadal, C. Sire, E. Kanso, C. Eloy, Hydrodynamic interactions influence fish collective behavior, arXiv`arXiv:1705.07821`.

[20] S. Shams, R. T. Gerlai, Pharmacological manipulation of shoaling behavior in zebrafish, Current Psychopharmacology 5 (2) (2016) 180–193.

[21] Y. Katz, K. Tunstrøm, C. C. Ioannou, C. Huepe, I. D. Couzin, Inferring the structure and dynamics of interactions in schooling fish, PNAS 108 (46) (2011) 18721.

[22] J. E. Herbert-Read, A. Perna, R. P. Mann, T. M. Schaerf, D. J. Sumpter, A. J. W. Ward, Inferring the rules of interaction of shoaling fish, PNAS 108 (46) (2011) 18726–18731.

[23] J. E. Herbert-Read, Understanding how animal groups achieve coordinated movement, J. Exp. Biol. 219 (19) (2016) 2971–2983.

[24] S. Butail, V. Mwaffo, M. Porfiri, Model-free information-theoretic approach to infer leadership in pairs of zebrafish, Phys. Rev. E 93 (4) (2016) 042411.

[25] A. K. Zienkiewicz, D. A. W. Barton, M. Porfiri, M. Di Bernardo, Leadership emergence in a data-driven model of zebrafish shoals with speed modulation, Eur. Phys. J. Spec. Top. 224 (17-18) (2015) 3343–3360.

[26] A. Eriksson, M. Nilsson Jacobi, J. Nystrom, K. Tunstrom, Determining interaction rules in animal swarms, Behav. Ecol. 21 (5) (2010) 1106–1111.

[27] R. Lukeman, Y.-X. Li, L. Edelstein-Keshet, Inferring individual rules from collective behavior, PNAS 107 (28) (2010) 12576–12580.

[28] B. L. Partridge, T. J. Pitcher, The sensory basis of fish schools: relative roles of lateral line and vision, J. Comp. Physiol. 135 (1980) 315–325.

[29] T. J. Pitcher, The Behaviour of Teleost Fishes, Springer, Boston, MA, 1986.

[30] J. Gautrais, F. Ginelli, R. Fournier, S. Blanco, M. Soria, H. Chaté, G. Theraulaz, Deciphering interactions in moving animal groups., PLoS Comput. Biol. 8 (9) (2012) e1002678.

[31] D. S. Calovi, U. Lopez, S. Ngo, C. Sire, H. Chaté, G. Theraulaz, Swarming, schooling, milling: phase diagram of a data-driven fish school model, New J. Phys. 16 (1) (2014) 015026.

[32] B. Collignon, A. Séguret, J. Halloy, A stochastic vision-based model inspired by zebrafish collective behaviour in heterogeneous environments, Roy. Soc. Open Sci. 3 (1) (2016) 150473.

[33] M. Sfakiotakis, D. M. Lane, J. B. C. Davies, Review of fish swimming modes for aquatic locomotion, IEEE J. Ocean. Eng. 24 (2) (1999) 237–252.

[34] A. Berdahl, C. J. Torney, C. C. Ioannou, J. J. Faria, I. D. Couzin, Emergent sensing of complex environments by mobile animal groups, Science 339 (6119) (2013) 574–576.

[35] J. E. Herbert-Read, S. Krause, L. J. Morrell, T. M. Schaerf, J. Krause, A. J. W. Ward, P. R. S. B, The role of individuality in collective group movement, Proc. R. Soc. B Biol. Sci. 280 (December 2012) (2013) 20122564.

[36] A. Strandburg-Peshkin, C. R. Twomey, N. W. F. Bode, A. B. Kao, Y. Katz, C. C. Ioannou, S. B. Rosenthal, C. J. Torney, H. S. Wu, S. A. Levin, I. D. Couzin, Visual sensory networks and effective information transfer in animal groups., Curr. Biol. 23 (17) (2013) R709–711.

[37] R. Spence, G. Gerlach, C. Lawrence, C. Smith,The behaviour and ecology of the zebrafish, *Danio rerio.*, Biol. Rev. Camb. Philos. Soc. 83 (1) (2008) 13-34.

[38] K. Tunstrøm, Y. Katz, C. C. Ioannou, C. Huepe, M. J. Lutz, I. D. Couzin, Collective States, Multistability and Transitional Behavior in Schooling Fish, PLoS Comput. Biol. 9 (2) (2013) e1002915.

[39] S. Viscido, J. Parrish, D. Grünbaum, Individual behavior and emergent properties of fish schools: a comparison of observation and theory, Mar. Ecol. Prog. Ser. 273 (2004) 239–249.

[40] J. Gautrais, C. Jost, M. Soria, A. Campo, S. Motsch, R. Fournier, S. Blanco, G. Theraulaz, Analyzing fish movement as a persistent turning walker., J. Math. Biol. 58 (3) (2009) 429–445.

[41] D. S. Calovi, U. Lopez, P. Schuhmacher, H. Chate, G. Theraulaz, Collective response to perturbations in a data-driven fish school model, J. R. Soc. Interface 12 (2015) 20141362.

[42] I. D. Couzin, J. Krause, R. James, Collective memory and spatial sorting in animal groups, J. Theor. Biol. 218 (1) (2002) 1–11.

[43] F. Ladu, S. Butail, S. Macrí, M. Porfiri, Sociality modulates the effects of ethanol in zebra fish., Alcohol. Clin. Exp. Res. 38 (7) (2014) 1–9.

Data-driven modelling of social forces and collective behaviour in zebrafish

A K Zienkiewicz, F Ladu, D A W Barton, M Porfiri & M Di Bernardo

Supporting Information

S1. Zebrafish experiments

Experiments with live zebrafish were conducted at the Dynamical Systems Laboratory (New York University Tandon School of Engineering, NY, USA) and were approved by the University Animal Welfare Committee of New York University under protocol number 13-1424. The animals and apparatus used to acquire trajectory data for swimming zebrafish pairs, was broadly similar to those described previously in [13]. In the present study however, a camera with higher spatial and temporal resolution was used to observe fish swimming in the experimental tank. Where appropriate we also make use of recently published data in [43], obtained under similar experimental conditions for isolated individuals and groups of five zebrafish.

S1.1. Animals and environment

Wild-type zebrafish *(Danio rerio)* were bought online (LiveAquaria.com, Rhinelander, WI, USA) and housed according to the description in [13]. At the time of the experiments, fish were 6-8 months of age, with a mean body length of approximately 3 cm. A photoperiod of approximately 12 hr light, 12 hr dark per day was automatically prescribed in accordance with the natural circadian rhythm of zebrafish [44]. Water temperature and pH in the holding tanks were maintained at 27 ± 1°C and 7.2 respectively. Feeding with commercial flake food (Hagen Corp./Nutrafin Max, USA) was carried out on a daily basis at 7 pm. In total, 36 experimentally naïve individuals were used for this study, allowing for a ten day acclimatisation period in holding tanks prior to experimentation.

S1.2. Apparatus

Experimental subjects were observed in a tank measuring $120 \times 120 \times 20$ cm (10 cm water depth). A ring of radius 45 cm placed inside the tank provides a barrier restricting the freedom of movement of zebrafish to within the interior circular region. The bottom surface of the tank, and the circular wall was covered with a white contact paper — enhancing the contrast for automated tracking. The entire tank assembly was supported on an aluminium frame, with diffused overhead provided by four 25 W fluorescent tubes (All-Glass Aquarium, preheat aquarium lamp, U.K.). Opaque curtains surrounding the tank were used during observations to provide shielding from the laboratory.

Video frames were recorded with a high-resolution, high-bandwidth Flea3 (USB 3.0) camera (Point Grey Research, Richmond, Canada), mounted 80 cm above the water surface, centred over the circular ring. The camera was configured to record full-colour frames at 30 Hz with 1280×960 pixel resolution using high-quality MJPEG compression.

1

S1.3. Experimental procedure

Observations were conducted for 18 unique pairs of experimentally naïve zebrafish. Before each trial, two fish were hand-netted at random from the holding tanks. Test subjects were transferred directly to a single 250 ml glass beaker, filled with water from the holding tank and the experimental tank in roughly equal measures. The beaker was placed in the experimental tank and after 10 min, it was gently tipped to release the fish in the experimental tank. This procedure was selected to reduce any potential shock arising from differences in water quality or temperature between the holding and experimental tanks. Video recording was initiated shortly afterwards, filming for 30 min in total, which included an initial 10 min period allowing for habituation to the novel environment [45] — discarded from subsequent analysis. On completion of each 30 min observation, test subjects were retrieved with the hand net and transferred to a separate holding tank.

S1.4. Tracking and trajectory reconstruction

Video image analysis and multi-target tracking was achieved using an in-house software package ('Peregrine' [8]), identical to that used in our analysis in [13]. Tracking was performed off-line enabling at the maximum video frame rate: $F_s = 30\,\text{Hz}$.

Raw experimental data consisted of two-dimensional Cartesian positions $\mathbf{x}_i(t) = [x, y]_i(t)$ for each fish i, measured in centimeters from the origin, positioned at the centre of the circular tank. For this experiment, it is important that each fish can be uniquely identified throughout each observation. By evaluating the size distribution of each fish, determined by the area of a blob measured in pixels, the tracking software continuously monitored for occlusions — where fish were found to overlap from the perspective of the camera. In frames where blobs were found to be larger than 2 standard deviations of their mean size, an expectation-minimisation algorithm was used to optimally fit Gaussian distributions to the larger, occluded blob [46].

Using an off-line graphical user interface, trajectory data for each observation was then manually verified in their entirety, to ensure that the unique identity of each fish was preserved for the entire 20 min period, post habituation (as per [43]). Tracking errors such as an unresolved occlusions, missing data or false detections could therefore be found and corrected in all instances.

S1.5. Position smoothing

Prior to further analysis, raw position data $\mathbf{x}(t)$ was smoothed using a third-order Savitsky-Golay (SG3) moving average filter [47], with a nominal moving average window of 15 samples, equivalent to $0.5\,\text{s}$ (using the built-in MATLAB *smooth* function with the 'sgolay' option). From this smoothed time-series data, we then computed both the velocity $\mathbf{v}(t)$ and acceleration $\mathbf{a}(t)$ in the tank-reference frame, numerically via successive (backwards) finite differences. Instantaneous speed $u(t)$ is given by the velocity vector norm: $u(t) = \|\mathbf{v}(t)\|$. Turn-rate $\omega(t)$ is computed via an approximation of the trajectory curvature through a symmetric window of position samples, assuming a path along the circumcircle prescribed by these positions. Angular acceleration $\dot{\omega}(t) = \mathrm{d}\omega(t)/\mathrm{d}t$ is computed similarly, via the central difference of the approximated turn-rate.

Different from our previous analysis in [13], the velocity vectors of each fish are computed as the time-derivative of position data, smoothed using a Savitsky-Golay (SG) filter, rather than using Kalman filtered velocity data generated by the tracking software [8]. The SG filter

works by convolving successive subsets of data, within a fixed sample window (w), fitted to a low-degree (p) polynomial using the least-squares method. This alternative method provides a simple and consistent means by which we can suppress the noise (measurement errors) inherent in the automated visual tracking procedure. By adjusting the sample window size of the SG filter, the degree to which the position data is smoothed can now be varied to observe its effect on model parameter calibration. Since all other metrics (speed, turn-rate, acceleration etc.) are estimated in some way using the position data, we also befit from a single, controllable source of filtering such that its effects can be more easily characterised. Later in this document (§S5), we provide a limited survey of the effects of smoothing, specifically in relation to the sample window size w, choosing to fix the polynomial order p of the SG filter. For a detailed study of optimal parameter $\{w, p\}$ selection for SG filtering, we refer the reader to the work of Krishnan *et al.* [48].

S1.6. Velocity estimation

In the computations required to produce the force maps resolved in this analysis, we suppress noise by applying a third-order $(p = 3)$ Savitsky-Golay (SG3) filter to smooth the tracked position data, nominally choosing a $w = 15$ sample moving-average window equivalent to $0.5\,\mathrm{s}$ at $30\,\mathrm{Hz}$. The velocity $\mathbf{v}(t)$, and acceleration $\mathbf{a}(t)$ are then computed from successive finite differences using

$$\mathbf{v}(t + \Delta t) = \left(\mathbf{x}(t + \Delta t) - \mathbf{x}(t)\right)/\Delta t$$

and

$$\mathbf{a}(t + \Delta t) = \left(\mathbf{v}(t + \Delta t) - \mathbf{v}(t)\right)/\Delta t$$

respectively, where $\mathbf{x}(t)$ now refers to smoothed position values. The instantaneous (scalar) speed $u(t)$ is then calculated trivially from the vector norm of the velocity, where $u(t) = \|\mathbf{v}(t)\|$.

Selection of the SG filter parameters $\{w = 15, p = 3\}$ is achieved heuristically and discussed later in §S5 where we further adjust w to calibrate model parameters. Alternative methods which attempt to optimise the accuracy of velocity estimation from noisy position data via adaptive sample windowing have been considered [49]. However, trial implementation of these methods have not yet proved successful using reasonable estimates of the tracking noise. Whichever method is used, we should be mindful that every metric we consider is derived solely from discretely sampled positions; for example, first and second derivatives for velocity and acceleration. As such, position errors unavoidably propagate to all measurements and will be magnified when computing higher order derivatives.

S1.7. Turn rate estimation: adaptive curvature method

In our previous study [13], we described a method of computing the turn-rate $\omega(t)$ time-series from the (Kalman filtered) velocity $\mathbf{v}(t)$, in the absence of explicit information indicating the orientation of the fish (velocity method). Having now chosen to ignore the Kalman filtering method in favour of SG smoothing of position vectors, we consider an alternative method for computing $\omega(t)$, directly from the available position data. Extending a method previously described in [40], we estimate the trajectory curvature as a (short) moving average through consecutive position samples to infer the angular deviations of the fish's heading (curvature method).

3

At each time step, we compute the radius of a circumcircle described by three position samples, symmetrically spaced in time around the position at time t. From this, we derive the angle of arc $\Delta\phi$ between the end points, estimating $\omega(t)$ from the central difference (see Fig. S1). In general, to estimate the turn rate at time t, we construct the circumcircle defined by vertices: $\mathbf{x}(t - n\Delta t)$, $\mathbf{x}(t)$ and $\mathbf{x}(t + n\Delta t)$, and compute the angle $\Delta t\phi$ describing the arc from $\mathbf{x}(t - n\Delta t)$ to $\mathbf{x}(t + n\Delta t)$ about the circumcentre, giving $\omega(t) \approx \Delta t\phi/(2n\Delta t)$. From this approximated $\omega(t)$ time series, we can then also compute the angular acceleration $\dot{\omega}(t)$ via the (central) finite difference given the sample period Δt.

Typically, the turn rate is approximated using a default symmetric window size of $n = 1$ samples, [14, 40], such that we compute the arc between position samples either side of the position $\mathbf{x}(t)$. When the fish is found to be very slow moving, the random tracking error in position samples becomes large in comparison to the true displacement between successive samples, producing potentially large fluctuations in measured turn rate. If we wish to continue estimation of turn rate during these very slow moving periods (excluded from force mapping analysis — see §S2), we can adjust the window size n as a function of the fish's speed, smoothing out high-frequency tracking noise. A simple algorithm was therefore implemented to increment n until the average speed along the trajectory between end points $\mathbf{x}(t - n\Delta t)$ and $\mathbf{x}(t + n\Delta t)$, exceeds a threshold $u_{\min}$, for each computation of the turn rate $\omega(t)$ and time t, that is when the condition

$$\frac{1}{n\Delta t} \sum_{k=-n+1}^{n} \|\mathbf{x}(t + k\Delta t) - \mathbf{x}(t + (k-1)\Delta t)\| > u_{\min} \tag{8}$$

is satisfied, where $u_{\min} = 0.2\,\mathrm{BL\,s^{-1}}$, chosen heuristically to achieve adequate noise suppression.

For a comprehensive study comparing the velocity based method used in [13], the position based method ($n = 1$), and an alternative solution for $\omega(t)$ in which orientations are obtained directly shape-tracking measurements, we refer the reader to the recent work of Mwaffo *et al.* [50].
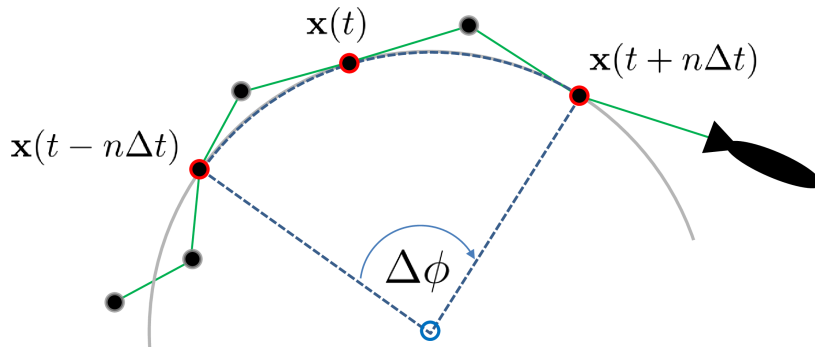

Figure S1: **Position based (curvature) method for approximating turn rate.** Turn rate $\omega(t) = \mathrm{d}\phi/\mathrm{d}t \approx \Delta\phi/2n\Delta t$ at time t is estimated using the curvature of the trajectory segment (green) centred on position sample $\mathbf{x}(t)$, about the circumcentre (blue circle) of three symmetrically time-spaced position samples (red outlined circles) - example shown here with window size $n = 2$ samples.

S2. Social-force mapping: methodology

To infer interactions between fish, we use a force mapping method similar to that described by Katz *et al.* in [21] to compute the acceleration of a focal fish as a function of the relative position and orientation of its neighbour. As in [21], the components of this acceleration are referred to as social reaction 'forces', both tangential to the direction of motion ('speeding force': $a^{\parallel}$), and a radial component ('turning force': $a^{\perp}$). In the present study, we perform an additional analysis of the resultant *angular* acceleration, $\dot{\omega}(t)$, and therefore adopt the more specific terms: tangential, radial and angular acceleration accordingly. In this way, we intentionally discriminate between turning interactions which incur changes in radial (left-right axis) speed, and those which result in changes to the angular speed (turn-rate) of the focal fish, $\omega(t)$.

Importantly, by computing both the angular and radial components of the fish's acceleration, we are able to distinguish between responses leading to a net change in position, that is an attractive and repulsive force, and those which result in the specific alignment of the fish. The first measure $a^{\perp}$, indicates changes to the radial component of the fish's velocity, that is to say how much more has it moved to its left or right as a result of a turning manoeuvre. The angular acceleration $\dot{\omega}$ is the rate of change of angular velocity, inferred from the varying curvature of the trajectory. Both measures are clearly related, not least because they are both computed from the same trajectory position samples. More specifically, as the fish changes its orientation, or heading angle, with turn-rate $\omega(t)$ (angular velocity), the radial acceleration along its trajectory depends on the forward speed $u(t)$, with an approximate relationship given by:

$$a^{\perp}(t) = \lim_{\Delta t \to 0} \frac{u(t)}{\Delta t} \sin\left(\omega(t)\Delta t\right) \approx u(t)\omega(t) \tag{9}$$

where Δt is the small time increment between position samples.

The dependence of $a^{\perp}$ on ω in (9) implies a phase lag between the radial acceleration component and angular acceleration such that whilst the radial speed might be decreasing ($a^{\perp} < 0$), the curvature of the trajectory in the same direction can still be increasing ($\dot{\omega} > 0$). Crucially for our analysis of the social interaction 'forces', the signs, or directions of $a^{\perp}(t)$ and $\dot{\omega}(t)$, can be opposed whilst consistently describing different features of how a fish turns in response to a neighbour: its attraction or propensity to align.

In the present study, we consider a variety of dynamical relationships conferred by interactions, explored in terms of different functions of the pair's spatial and dynamical configuration. The various constructions for the force-maps used to explore these relationships are described in what follows.

S2.1. Spatial force maps

Spatial force maps are two-dimensional histograms, constructed using values of the acceleration, $a^{\parallel}$, $a^{\perp}$, or $\dot{\omega}$ computed for a focal fish, given the relative position of its neighbour at every sampled time frame. By expressing both the acceleration and relative position in a moving reference frame aligned with the focal fish's direction of motion, we can derive a spatial mapping which is independent of the its position in the tank, as follows.

For each data sample at time t, the acceleration $\mathbf{a}_i = [a^x, a^y]_i$ of a focal fish i, in the tank reference frame, is decomposed into two components of $\mathbf{a}'_i = [a^\parallel, a^\perp]_i$, describing the tangential acceleration $a_i^\parallel$ parallel to the direction of the fish i's motion, and a radial acceleration $a_i^\perp$ in the perpendicular direction. This simple transformation is accomplished by rotating the tank frame vector $\mathbf{a}_i$ by negative ϕ_i — fish i's current heading angle with respect to the x-axis, where

$$\phi_i = \mathrm{atan2}(v_i^y, v_i^x) \tag{10}$$

This is achieved by performing the rotation

$$\mathbf{a}_i'^T = \mathbf{R}\mathbf{a}_i^T \tag{11}$$

where R is the rotation matrix:

$$\mathbf{R} = \begin{bmatrix} \cos\alpha & -\sin\alpha \\ \sin\alpha & \cos\alpha \end{bmatrix}; \alpha = -\phi_i \tag{12}$$

and 'atan2' is the four-quadrant arctangent function providing the (signed) heading direction $[-\pi, \pi]$ from the positive x-axis, given the velocity $\mathbf{v}_i = [v^x, v^y]_i$ of fish i in the tank reference frame.

The position $\mathbf{d}_j$ of a neighbouring fish j is expressed in terms of its front-back distance d_{FB} and its left-right distance d_{LR}, relative to the focal fish i placed at the origin with its velocity vector aligned with the positive x-axis. Here, an identical rotation transformation is performed:

$$\mathbf{d}_j = [d_{FB}, d_{LR}]_j^T = \mathbf{R}(\mathbf{x}_j - \mathbf{x}_i)^T \tag{13}$$

giving us the required orthogonal components d_{FB} and d_{LR} with respect to the focal fish's orientation. A schematic diagram showing the construction of relative position and linear reaction 'forces' ($a^\parallel$ and $a^\perp$), is shown in Fig. 1.

To construct each of the 'social-force' (acceleration) maps, reported in this study, we discretise the relative positional space around the focal fish into n_b^2 bins of equal width δ_d defining a square grid, spanning $\pm d_{\max}$ in both front-back and left-right axes. For each data sample at time t, we determine the correct bin index $(n(t), m(t))$ by interpolating the pair separation vector (d_{FB}, d_{LR}) in the focal fish reference frame across the coarse grid, that is

$$n(t) = [d_{LR}(t) - \mathrm{mod}(d_{LR}(t), \delta_d)] / \delta_d \tag{14a}$$
$$m(t) = [d_{FB}(t) - \mathrm{mod}(d_{FB}(t), \delta_d)] / \delta_d \tag{14b}$$

In separate histogram matrices, we accumulate the associated values of $a^\parallel$, $a^\perp$, or $\dot\omega$ of each sample in the bin according to (14). A separate relative position density matrix (map) is constructed trivially by incrementing the appropriate bin values by 1. This process is performed twice for each set of observation data, once for each focal fish, producing composite histograms for the entire data set of 18 (20 min duration) observation. Relative position density plots are normalised by the maximum bin occupancy, such that bin values are expressed as a percentage of this value. Finally, bin values are averaged by the number of pair permutations (36 focal fish comparisons). For linear components, further division by the average fish body length (3 cm) provides accelerations in units of $\mathrm{BL\,s}^{-2}$. Additional smoothing is

6

applied via numerical (bicubic) interpolation across the square grid, up-scaling by a factor of ten, such that a 30×30 grid of histogram bins becomes a 300×300 grid of values.

To avoid potentially strong interactions with tank boundaries, data frames in which either fish is closer than $2\,\mathrm{BL}$ to the boundary, regardless of their orientation, are rejected from all force mapping analyses. Frames in which the speed of either fish $u(t) < 0.2\,\mathrm{BL\,s^{-1}}$, $u(t) > 10\,\mathrm{BL\,s^{-1}}$ are also rejected to reduce spurious angular fluctuations which result from tracking noise at low (or stationary) fish speeds. Note that at very low speeds, approximated accelerations / forces become effectively zero.

S2.2. Semi-spatial force maps

In addition to the described spatial mappings, where histograms are binned according to the relative position (d_{FB}, d_{LR}), we also consider alternative maps in terms of other pertinent variables. Specifically, we construct $(a^{\parallel}, a^{\perp}$, and $\dot{\omega})$ histograms maps for: the relative orientation ϕ_{ij} between interacting fish; and the swimming speed of either the focal fish u_f, or neighbouring fish u_{nb}. Two-dimensional histograms, or semi-spatial maps, are constructed in a similar way as before, where we now average over sample values of either d_{FB} or d_{LR} depending on the relationship of interest. Here, the accumulated acceleration values are binned with indexes $(n(t), m(t))$. Using an example of $a^{\perp}$ mapped as functions of d_{LR} and ϕ_{ij} (averaging over d_{FB}), we have:

$$n(t) = \left[d_{LR}(t) - \mathrm{mod}(d_{LR}(t), \delta_d)\right] / \delta_d \qquad (15)$$

$$m(t) = \left[\phi_{ij}(t) - \mathrm{mod}(\phi_{ij}(t), \delta_\phi)\right] / \delta_\phi \qquad (16)$$

where bin width δ_ϕ is equal to $2\pi/n_b$ (radians).

S3. Spatial structure of zebrafish alignment responses

Following our summary in the main text (§2.4), we provide a detailed description of the angular (Fig. S2.A) and radial (Fig. S3.A) acceleration responses for clockwise rotations of the focal zebrafish's neighbour – with observations being identical for anti-clockwise oriented neighbours, but mirrored in the d_{LR} axis with $\dot{\omega}$ negated. Supporting our description in the main text, we also provide comparison plots comparison for simulated pairs (Fig. S2.B & Fig. S3.B).

When neighbours have a positive d_{FB} velocity component with respect to the focal fish $(0 < \phi_{ij} < \pi/2)$, the spatial structure of $\dot{\omega}$ is generally isotropic such that the focal fish's angular acceleration is in the clockwise direction, to align with its neighbour. An exception is in the front-right spatial quadrant in which the neighbour is moving away from the focal fish, both in terms of its d_{FB} and d_{LR} velocity components. In this particular configuration, where conspecifics are receding yet highly visible, it is possible that explicit alignment gives way to (radial) attraction, found to be strong for these orientations in the same spatial region (Fig. S3.A).

When neighbours velocities have a negative d_{FB} component $(\pi/2 < \phi_{ij} < \pi)$, the $\dot{\omega}$ turning response of the focal fish is distinctly anisotropic with respect to the position of the neighbour. For these neighbour orientations, the turning response is magnified in the front-left quadrant where the neighbour's velocity is directed towards the focal fish, and in

7

the rear-right quadrant where the neighbour's velocity is approximately away from the focal fish. The enhanced alignment response when the neighbour is ahead and oriented towards the focal fish is a possible evidence of evasive manoeuvres where a focal fish adjusts its orientation more rapidly to avoid a collision. Enhancement in the rear-right quadrant may simply indicate that a more rapid turning response is required to maintain visibility of the a posterior neighbour, moving away from the focal fish.

Opposite front-right and rear-left spatial quadrants indicate what appears to be 'anti-alignment' behaviour, with significant regions where $\dot{\omega} < 0$. In the rear-left quadrant, the increased turning to the left (anticlockwise) may still be the consequence of an alignment response, but one which better maintains visibility of a neighbour positioned initially behind the focal fish. In other words, the focal fish chases the tail of its neighbour, turning to keep it in its left visual field. In contrast, turning in the opposite direction (clockwise) may result in more rapid alignment but at the expense of losing sight of the stimulus. The negative (anticlockwise) region of $\dot{\omega}$ observed in the front-right quadrant is also well pronounced, however we do not currently offer a reasonable hypothesis as to the possible causes underlying this specific response.
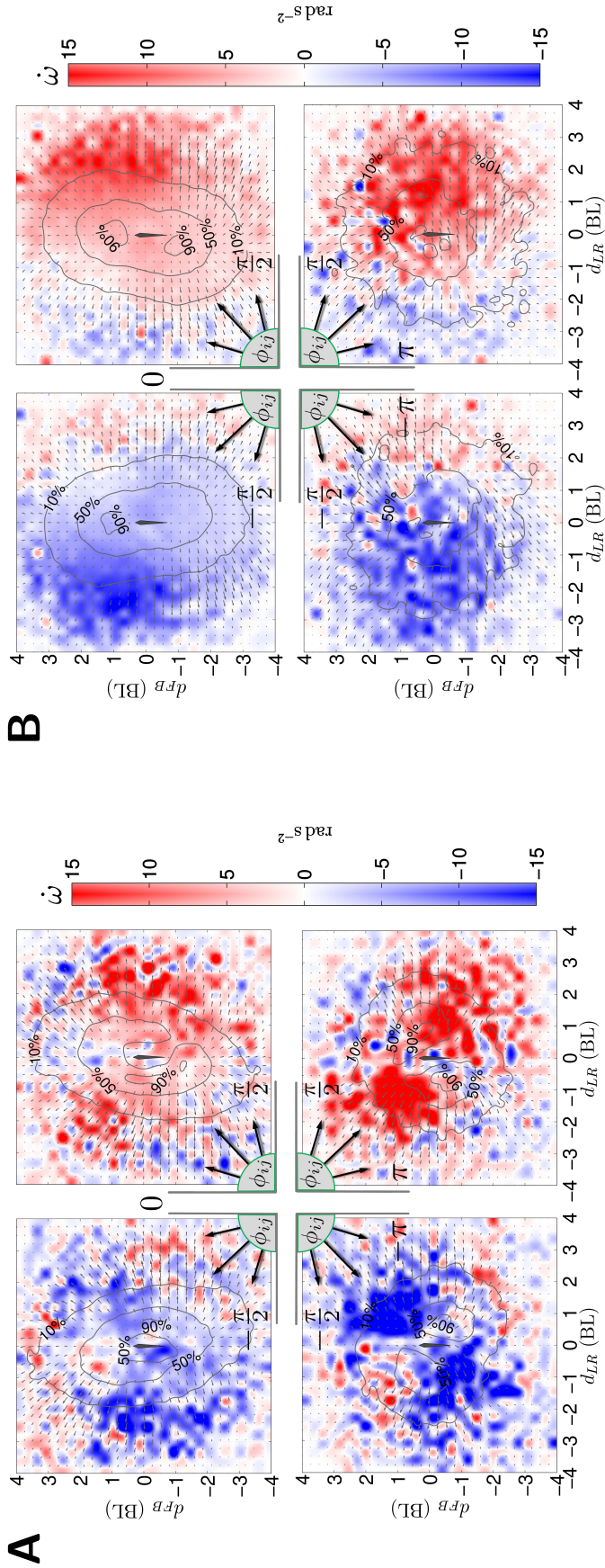
Figure S2: **Angular acceleration responses of focal fish as a function of neighbour position and relative orientation.** Histograms map show the average angular acceleration $\dot{\omega}$, of (A) the focal zebrafish, and (B) simulated fish as they vary depending on the relative position of their neighbours. Panels show data isolated for ranges of relative heading angle ϕ_{ij} split across four quadrants: (top-left) $-\frac{\pi}{2} < \phi_{ij} \leq 0$, (top-right) $0 < \phi_{ij} \leq \frac{\pi}{2}$, (bottom-left) $-\pi < \phi_{ij} \leq -\frac{\pi}{2}$, (bottom-right) $\frac{\pi}{2} < \phi_{ij} \leq \pi$. Positive values of ϕ_{ij} indicate neighbour is rotated clockwise with respect to the focal fish. Positive angular accelerations indicate increased (clockwise) turning to the right, negative angular accelerations indicate increased (anti-clockwise) turning to the left. Contours show isolevels of population density as percentages of the maximum bin value for each panel individually. Arrows indicate the vector field given by $[a^{\parallel}, a^{\perp}]$. In each quadrant we find that overall, the angular acceleration is such that the focal fish rotates in the direction required to align with the neighbour's orientation, indicated by arrows at each corner.
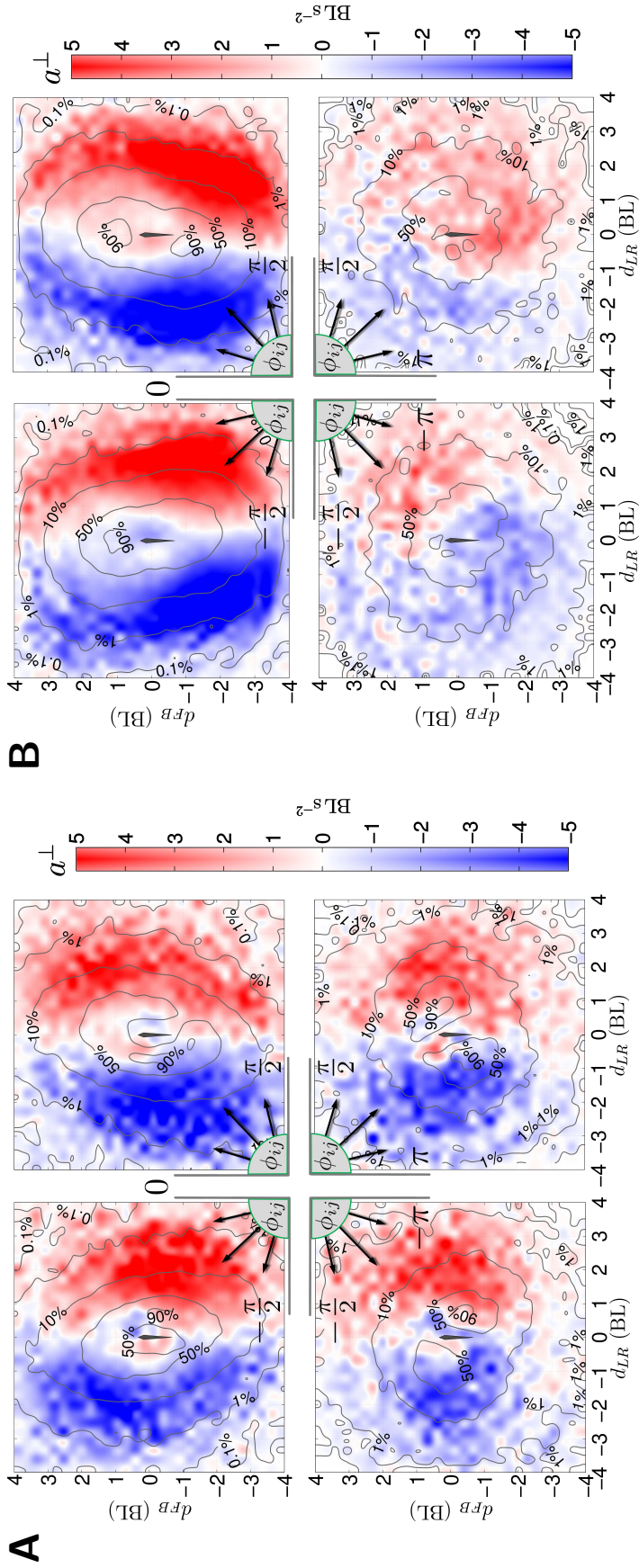
Figure S3: **Radial force responses of focal zebrafish as a function of neighbour position and relative orientation.** Histograms map show the radial acceleration $a^\perp$ of (A) the focal zebrafish, and (B) simulated fish, as they vary depending on the relative position of their neighbours. Panels show data isolated for ranges of relative heading angle ϕ_{ij} split across four quadrants: (top-left) $-\frac{\pi}{2} < \phi_{ij} \leq 0$, (top-right) $0 < \phi_{ij} \leq \frac{\pi}{2}$, (bottom-left) $-\pi < \phi_{ij} \leq -\frac{\pi}{2}$, (bottom-right) $\frac{\pi}{2} < \phi_{ij} \leq \pi$. Positive values of ϕ_{ij} indicate neighbour is rotated clockwise with respect to the focal fish. Positive radial forces (red) indicate increased acceleration to the right, negative radial forces indicate increased acceleration to the left. Contours show isolevels of population density as percentages of the maximum bin value for each panel individually. In each quadrant we find that unlike the angular acceleration, the radial acceleration is strongly influenced by the relative position but not the relative orientation.

10

S4. Numerical implementation of shoal model

Simulated trajectories for multiple fish are computed by numerical integration of the equations of motion for speed $U_i(t)$ and turn rate $\Omega_i(t)$ described by the SDEs in (1). Discrete solutions are obtained using the Euler-Maruyama method [51, ch.10], where for each fish i we have:

$$U_i(t + \Delta t) = U_i(t) + \theta_u\big(\mu_u + U_i^*(t) - U_i(t)\big)\Delta t + \sigma_u \Delta W(t) \tag{17a}$$

with $U_i(t)$ truncated between $[0 \ldots U_{\max}]$, and

$$\Omega_i(t + \Delta t) = \Omega_i(t) + \theta_\omega\big(\Omega_i^*(t) + f_{Wi}(t) - \Omega_i(t)\big)\Delta t + \sigma_\omega \Delta Z(t) \tag{17b}$$

with $\Omega_i(t)$ truncated between $[-\Omega_{\max} \ldots \Omega_{\max}]$.

Here Δt is the (short) time step duration, with $\Delta W(t)$ and $\Delta Z(t)$ being independent and identically distributed normal random variates with zero mean and variance $\sqrt{\Delta t}$. In general for the group of N fish, we can define heterogeneous sets of parameters, such that $\mu_u = \mu_{u[i=1..N]}$, $\theta_\omega = \theta_{\omega[i=1..N]}$, etc. are individually assigned for each fish i, to account for their unique locomotory characteristics. However, for much of the comparative analysis presented in this study, we obtain and prescribe a set of mean model parameters (homogeneous agents).

Each trajectory realisation is a two-dimensional (correlated) random walk in the plane, where the heading angle $\phi(t)$ and position $\mathbf{x}(t)$ at time t are sequentially updated via Euler integration using values of speed $U(t)$ and turn rate $\Omega(t)$ generated, as follows.

- Heading angle update (wrapped within a range of $[-\pi, \pi]$ radians):

$$\phi(t) = ([\phi(t - \Delta t) + \pi + \Omega(t)\Delta t] \bmod 2\pi) - \pi \tag{18a}$$

- Position update:

$$\mathbf{x}(t) = \mathbf{x}(t - \Delta t) + \mathbf{V}(t)\Delta t, \quad \mathbf{V}(t) = U(t)\left[\cos(\phi(t)), \sin(\phi(t))\right] \tag{18b}$$

For every realisation of N agents, initial positions $\{\mathbf{x}(0)_i\}_{i=1}^N$, were uniformly distributed within the circular virtual tank boundary ($R_{\text{tank}} = 45$ cm), with uniformly random heading angles in $[-\pi, \pi]$. Initial speeds were set to the equilibrium speed parameter value, $\{U(0)_i\}_{i=1}^N = \mu_u$, with turn-rate $\{\Omega(0)_i\}_{i=1}^N = 0$. For all numerical realisations of the model described in this study, we set $\Delta t = 1/30$ s ($F_s = 30$ Hz) — previously found to be sufficient for accurate numerical integration [13]. Sample generation frequency is matched with the experimental acquisition frequency for convenience.

S4.1. Computing the wall avoidance function (f_W)

The value of the wall avoidance term $f_W(t)$ in (3) is calculated at each time t by projecting the velocity vector of a fish, from its current position, to its intersection with the circular boundary (radius $R_{\text{tank}} = 45$ cm) of the virtual tank. For each sample with Cartesian position and velocity components $\mathbf{x}(t) = [x_x, x_y](t)$ and $\mathbf{v}(t) = [v_x, v_y](t)$, the collision point at the boundary $\mathbf{x}_c$ is computed from the intersection of the (infinite) line extending through both (x_x, x_y) and $(x_x + v_x, x_y + v_y)$, with the circular boundary described by $x^2 + y^2 = R_{\text{tank}}$. This

calculation yields two intersection points, of which we select only the point in front of the fish. From the chosen intersection $\mathbf{x}_c$ we compute the projected distance $d_W = \|\mathbf{x}_c - \mathbf{x}(t)\|$, and the corresponding collision angle ϕ_W according to:

$$\phi_W = \text{sgn}\big([\mathbf{x}_c \times \mathbf{v}(t)]_z\big) \cos^{-1}\left(\frac{d_W^2 + R_{\text{tank}}^2 - \|\mathbf{x}(t)\|^2}{2 d_W R_{\text{tank}}}\right) \tag{19}$$

Here, the (signum) function $\text{sgn}[\cdot]_z$ provides the required sign given by the z component of the cross product of the projected velocity with the normal vector at the collision point.

S5. Calibrating spontaneous motion via MLE

The parameters determining the locomotion individual fish are those required by the equations of motion, namely the speed (1a) and turn-rate (1b), in the absence of corresponding interaction responses U^* and Ω^*. With regard to the SDE governing forward speed U, the set of parameters includes: the equilibrium swimming speed μ_u, the speed fluctuation variance σ_u, and the relaxation (autocorrelation) rate θ_u. For the turn-rate process for Ω, we require: the parameters of the coupling function (f_c) governing the fluctuation variance, namely, α_c and β_c; the associated relaxation rate θ_ω; and also the parameters of wall avoidance function (f_W), that is α_W and β_W.

Extending the method used in [13], we again use maximum likelihood estimation (MLE) to obtain estimates for parameters of the updated individual-model. In this new approach, we explicitly include the coupling between the SDEs to estimate parameter values characterising this interaction, as well as approximations for the wall-avoidance, directly from the available speed and turn-rate data.

In contrast to the analytical solutions employed in [13], we compute the value of the likelihood function for all time-consecutive speed and turn-rate sample pairs which individually satisfy similar threshold criteria (minimum swimming speed, wall proximity, etc.). The eight parameters of the individual-model, described above, are subsequently computed via numerical optimisation to find values which maximise the log-likelihood.

S5.1. Deriving the likelihood function

The source data use to calibrate model parameters is discretely sampled, time-series data, approximating the speed $u(t)$ and turn-rate $\omega(t)$ of individual zebrafish. In order to derive the corresponding likelihood functions, we therefore require discrete-time versions of the equations of motion in (1), with linearised, continuous-time solutions given by

$$\text{(OU process)} \qquad \mathrm{d}S = \theta\big(\mu - S\big)\mathrm{d}t + \sigma \mathrm{d}W \tag{20}$$

where S is a mean-reverting stochastic process (mean μ and relaxation rate θ), with random fluctuations generated by the standard Wiener process W with variance σ^2. In this form, S describes a stationary, Gaussian process with normally distributed solutions [52]. Unlike the conventional linear OU process, the model equations have additional nonlinear terms in (1b), which account for the coupling between speed and turn-rate given by f_c, and the wall avoidance function f_W. However, over small time intervals, linear terms are expected to dominate, provided we use a suitable discrete-time solution.

Here we use an exact, analytical solution of (20) which is independent of the time-step, as derived in [53] — where for consecutive values S_i and S_{i+1}, spaced δ apart in time, we have:

$$S_{i+1} = S_i e^{-\theta\delta} + \mu(1 - e^{-\theta\delta}) + \sigma\sqrt{\frac{1 - e^{-2\theta\delta}}{2\theta}}\mathcal{N}_{0,1} \tag{21}$$

Here, $\mathcal{N}_{\mu=0,\sigma=1}$ indicates a standard normal random variate, with a probability density $f(x)$ given by:

$$f(x|\mu,\sigma) = \frac{1}{\sigma\sqrt{2\pi}}\exp\left(-\frac{(x-\mu)^2}{2\sigma^2}\right) \tag{22}$$

Extending this assumption of the probability density for both speed and turn-rate processes, we derive the conditional probability of an observation of either state S_{i+1} given a previous measurement S_i, as

$$f(S_{i+1}|S_i,\mu,\sigma,\theta) = \frac{1}{\sqrt{2\pi\hat{\sigma}^2}}\exp\left[-\frac{\left(S_{i+1} - S_i e^{-\theta\delta} - \mu(1 - e^{-\theta\delta})\right)^2}{2\hat{\sigma}^2}\right] \tag{23}$$

where from (21), we have made the substitution for the normal probability density function (pdf) variance

$$\hat{\sigma}^2 = \sigma^2\left(\frac{1 - e^{-2\theta\delta}}{2\theta}\right) \tag{24}$$

For a given parametrisation of the model $\eta \in [\mu, \sigma, \theta]$ we can write the likelihood function as the joint density function, or product of the independent probabilities of successive measurements, as follows

$$\mathcal{L}(\eta|S = S_1, \ldots, S_n) = \left(\frac{1}{\sqrt{2\pi\hat{\sigma}^2}}\right)^n \prod_{i=1}^{n}\exp\left[-\frac{\left(S_{i+1} - S_i e^{-\theta\delta} - \mu(1 - e^{-\theta\delta})\right)^2}{2\hat{\sigma}^2}\right] \tag{25}$$

Also we can write the corresponding log-likelihood function, as follows

$$\hat{\mathcal{L}} := \ln(\mathcal{L}) = -\frac{n}{2}\ln(2\pi) - n\ln(\hat{\sigma}) - \frac{1}{2\hat{\sigma}^2}\sum_{i=1}^{n}\left[S_{i+1} - S_i e^{-\theta\delta} - \mu(1 - e^{-\theta\delta})\right]^2 \tag{26}$$

where we wish to find the set of parameters η_{mle} which maximises $\hat{\mathcal{L}}$

$$\{\eta_{\text{mle}}\} \subseteq \{\arg\max_{\eta} \hat{\mathcal{L}}(\eta; S_1, \ldots, S_n)\} \tag{27}$$

The total log-likelihood, $\hat{\mathcal{L}}' = \hat{\mathcal{L}}_u + \hat{\mathcal{L}}_\omega$, is computed for our two equation model, where $\hat{\mathcal{L}}_u$ and $\hat{\mathcal{L}}_\omega$ are the log-likelihood values given by (26) for speed and turn-rate data respectively — where $\delta = 1/F_s = \Delta t$. For computing the likelihood $\hat{\mathcal{L}}_u$ from speed data u, we make the following value/parameter substitutions:

$$
\begin{aligned}
S_i &= u(t), \quad i = 1, \ldots, n && : \text{speed time series data} \\
\mu &= \mu_u && : \text{speed process mean-reversion} \\
\sigma &= \sigma_u && : \text{speed process volatility} \\
\theta &= \theta_u && : \text{speed process relaxation rate}
\end{aligned}
$$

13

Similarly, for computation of $\hat{\mathcal{L}}_\omega$ using turn-rate data $\omega(t)$, where we include nonlinear coupling and wall-avoidance terms:

$$
\begin{aligned}
S_i &= \omega(t), \quad i = 1, \ldots, n & &: \text{turn-rate time series data} \\
\mu &= \text{sgn}\big(\phi_W(t)\big)\alpha_W \exp\big(-\beta_W d_W(t)\big) & &: \text{wall-avoidance function } (f_W) \\
\sigma &= \alpha_c \exp\big(-\beta_c U(t)\big) & &: \text{turn-rate coupling function } (f_c) \\
\theta &= \theta_\omega & &: \text{turn-rate process relaxation rate}
\end{aligned}
$$

By making the above substitutions, all of the required parameters, including those describing the SDE coupling (f_c) and wall avoidance (f_W), are present in the description of the likelihood function $\mathcal{L}$. Note that the function f_W takes the place of the equilibrium parameter μ in $\mathcal{L}_\omega$, acting as a bias to an equilibrium turn-rate of zero. Similarly, the σ parameter in $\mathcal{L}_\omega$ is given by the coupling function with an explicit dependence on the speed $u(t)$. In contrast to our previous method in [13], the coupling parameters α_c and β_c are now estimated from both u and ω with a consistent probability model, described below.

The likelihood functions above are derived from the discrete-time solution of the standard OU process where we have linearised the model equations in (1) and assumed a normal probability density function. As we have discussed previously, the distributions of experimental turn-rate values ω, have much heavier tails than would be achieved using a standard OU equation possessing a normal distribution. The addition of the nonlinear coupling function f_c somewhat mitigates this discrepancy by enhancing turn-rate values at low swimming speeds, resulting in Ω distributions which compare more favourably to those found experimentally. An alternative modelling approach which seeks to address this issue directly can be found in [14]. The accuracy of the MLE calibrated parameter values depends on how well the underlying SDE can be approximated by a suitable, linearised SDE whereby nonlinear terms are held fixed over a single time step $\Delta t = 1/30\,\text{s}$.

We also note that measured values of forward speed u are strictly positive, contrasting with the normal pdf — defined over all real numbers. For fish with low mean swimming speeds, we therefore expect the distribution of experimental values u to exhibit heavier right hand (positive) tails, truncated to the left at zero. In such cases, the MLE method may perform poorly, fitting a (normal) distribution with exaggerated mean and reduced variance. However, results of MLE calibration of synthetic trajectory data, discussed in the following section, suggest that overall we are able to provide very good estimates for both μ_u and σ_u using the method described.

S5.2. Procedure

Parameter calibration using MLE is performed by constructing a single objective function equal to the sum of the log-likelihoods for both speed and turn-rate data, using two different applications of (26) with the substitutions given above. Specifically the objective function takes a trial set of input parameters

$$
\hat{\eta} = \{\eta_u\} \cup \{\eta_\omega\} = \{\mu_u, \sigma_u, \theta_u, \theta_\omega, \alpha_c, \beta_c, \alpha_W, \beta_W\}
$$

and returns the *negative* of the sum of both log-likelihoods, that is $-\hat{\mathcal{L}}(\eta, U, \Omega)$, which can be numerically minimised.

Finding the set of parameters $\hat{\eta}$ which minimises the objective function (maximises the log-likelihood) is achieved using a local gradient search algorithm. For this procedure we

14

employ the MATLAB® *fmincon* function (Optimisation Toolbox™, The Mathworks Inc) using a parallel, multi-start solver to find global minimum values of $\ln(\hat{\mathcal{L}})$, avoiding local minima. Parameters values within the set $\hat{\eta}$ are constrained between a lower bound of zero, and upper bounded by the vector $\hat{\eta} =$[10, 20, 10, 10, 50, 1, 50,1], with corresponding units [BL s^{-1}, BL s^{-1}, s^{-1}, s^{-1}, rad s$^{-3/2}$, s cm^{-1}, rad s^{-1}, cm^{-1}] – providing sufficient range for realistic parameter values and a more robust optimisation procedure. The multi-start solver is run using 20 initial parameters sets $\hat{\eta}_0$ with values uniformly distributed between the respective upper and lower bounds. The resulting optimisation yields the set corresponding to the smallest (scalar) value produced for $-\hat{\mathcal{L}}(\hat{\eta}, U, \Omega)$.

The input data required for the MLE calibration of an individual fish with n consecutive data samples, is a matrix of the form

$$\mathbf{M} = \begin{bmatrix} u_{(1)} & u_{(2)} & \omega_{(1)} & \omega_{(2)} & d_{W(1)} & \phi_{W(1)} \\ u_{(2)} & u_{(3)} & \omega_{(2)} & \omega_{(3)} & d_{W(2)} & \phi_{W(2)} \\ \vdots & \vdots & \vdots & \vdots & \vdots & \vdots \\ u_{(n-1)} & u_{(n)} & \omega_{(n-1)} & \omega_{(n)} & d_{W(n-1)} & \phi_{W(n-1)} \end{bmatrix} \tag{28}$$

where each row of represents a consecutive pair of speed u and turn-rate ω measurements, separated by the sampling period Δt and the projected wall distance and incident angle at time t. The objective function computes and sums the log-likelihood values via (26), calculated for each row of $\mathbf{M}$.

Using this pairwise construction of the input data allows us remove data pairs which contain extremes that may adversely affect the convergence of $\hat{\mathcal{L}}$ — essentially by removing entire rows, depending on the values of an individual element. In all calibrations, we chose to remove any data pairs in which either speed is between defined thresholds such that $u > U_{\min} = 0.2 \, \text{BL s}^{-1}$, and $u < U_{\max} = 10 \, \text{BL s}^{-1}$; or where $\omega > \Omega_{\max} = 20 \, \text{rad s}^{-1}$. When calibrating on experimental data, we also remove sample pairs where $d_W < 3 \, \text{BL}$ such that strong boundary effects are inhibited. With this final restriction, we are still able to estimate the wall interaction parameters α_W and β_W, providing there is a reasonably strong interaction beyond 3 BL, and that we have sufficient trajectory data where d_W is close to this limit.

S5.3. MLE calibration results

Model parameters for the individual-model equations were calibrated, for each of the 36 individual zebrafish trajectories. Crucially, we find that the degree to which the raw position data is smoothed via SG filtering has a strong impact on the resulting parameter values. By definition, the smoothing process reduces the degree to which position values deviate from a low-order polynomial function fitted to the trajectory (in a least-squares sense). The effect of this filtering is therefore to reduce transient fluctuations in position, and importantly for our calibration, in both the speed and turn-rate estimated from the position data. The impact on calibrating equilibrium values (for example μ_u) is expected to be minor; however SDE parameters describing the variance (σ) and autoregression (θ) should be more strongly affected by smoothing. Before we can obtain a reasonable estimate for a set of mean parameters from experimental data, we must first quantify the effects of position smoothing on the calibration of each parameter.
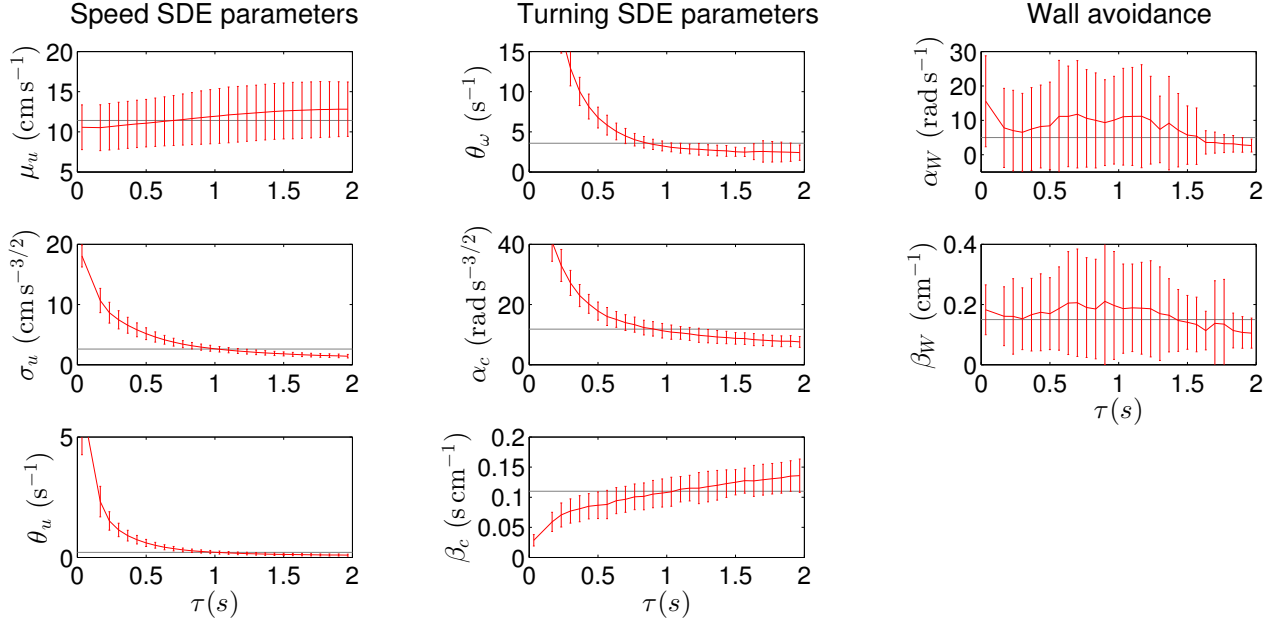
15

Figure S4: **Effect of smoothing position data on calibrating SDE parameters of 18 observations of zebrafish pairs.** Position data is either unsmoothed ($\tau = 0\,\mathrm{s}$), or smoothed using a third order Savitsky-Golay filter with varying sample window size prior to computation of speed and turn-rate used for MLE calibration. Mean values across all 36 individuals are reported with error bars showing associated standard deviation (red). Nominal input parameters selected for simulations are shown (grey lines) where we chose $\tau \approx 1\,\mathrm{s}$ (29 sample window).

The plots shown in Fig. S4 report the mean values of each parameter, averaged over all 36 zebrafish, calibrated using position data which has been smoothed with increasing values of the SG sample window size w, reported here in terms of the time duration spanning the window $\tau = w\Delta t$ (s), with $w = [5, 7, 9, \ldots, 59]$. As predicted, values corresponding to process fluctuations σ and α_c (variances around respective equilibria), and autocorrelation rates θ_u and θ_ω, are strongly affected by position smoothing. These values are found to decrease with as we increase the smoothing window, noting that the rate of decrease of σ_u is very similar to that of θ_u, and likewise for α_c and θ_ω. Process equilibria, namely μ_u and the wall avoidance parameters α_W and β_W, are comparatively much less affected by increased position smoothing.

From this analysis, the selection of the required smoothing window w is still non-trivial. In general, mean values of σ (or α_c) and θ decrease monotonically with increased w. The choice of w therefore appears somewhat arbitrary with a risk of over-smoothing, masking the intrinsic fluctuations of zebrafish motion, or under-smoothing and introducing artificial (tracking) noise. With both of these considerations in mind, we pragmatically chose a sample window $w = 29$ samples ($\tau \approx 1\,\mathrm{s}$).

S5.4. Nominal parameter selection

Having selected the appropriate level of smoothing, we report the parameters calibrated for individual fish, group in pairs, for each of the 18 observations where position data (Fig. S17). The mean values of each parameter, shown in respective figure panels, are chosen as the nominal model parameters adopted for this study (Tab. 1). However, MLE calibration

16

for wall avoidance parameters α_W and β_W is not always successful, resulting in the comparatively high standard deviation noted for these values in Fig. S4. For these parameters, we selected nominal values close to the median, computed across all observations, with $\alpha_W = 5$ and $\beta_W = 0.15$. Mean parameters values evaluated from our previous study of individual zebrafish (final column of Tab. 1) are found to compare well with those found in this study.

S6. Estimating interaction parameters

The parameters which describe the interaction between a pair of fish are those required by the speed response function U^* in (5a), and the turning response Ω^* in (5b). These include the three interaction strengths K_s, K_p, and K_v, corresponding respectively to the tangential (speeding) attraction and repulsion, the radial (turning) attraction and repulsion, and the (turning) alignment. We also require the radii of the repulsive regions r_u and r_ω which define the extent of the tangential and radial repulsive regions. Finally, we estimate the four parameters of the distance-decay functions which control the range and decay of the speeding and turning responses, namely δ_u, λ_u, δ_ω, and λ_ω.

Interaction parameters are estimated by applying the same force mapping analysis to simulated trajectory data. Initially, we compare the resulting axial projections (force profiles) of $a^\parallel$, $a^\perp$, and $\dot{\omega}$, with experimental data (Fig. 7), to estimate parameter values using an informed trial-and-error approach.[2]. The low dimensionality of the axial force/acceleration projections, provides a simple means by which we can quantify the resulting features of each interaction response – discussed in what follows.

S6.1. Repulsion radii

The repulsion radii r_u and r_ω are estimated directly from the axial projections of $a^\parallel$ and $a^\perp$ shown in Fig. 7. From these projections, we inferred the range of the repulsive regions as the values of d_{FB} and d_{LR} where the accelerations $a^\parallel$ or $a^\perp$ respectively, cross the zero axis. The projection of $a^\perp$ (Fig. 7B) was found to be highly symmetric in the d_{LR} axis, finding zero-crossings ($a^\perp = 0$) when $d_{LR} = 0$ and $d_{LR} \approx \pm 0.6\,\text{BL}$. We therefore chose the radial repulsion radius $r_\omega = 0.6\,\text{BL}$ (1.8 cm) as the nominal parameter value.

The equivalent $a^\parallel$ projection (Fig. 7A) indicated that repulsion in front of the fish (deceleration) is stronger than it is in the rear (acceleration) with an inflection that is not centred exactly at the origin ($d_{FB} = 0$). Rather, the inflection is displaced to negative d_{FB}, such that we observe deceleration when the neighbour is still slightly to the rear of the focal fish. In our model, we chose to approximate the repulsive interaction at close proximity to the focal fish with a symmetric response, centred at $d_{FB} = 0$, selecting a value $r_u = 1.2\,\text{BL}$ (3.6 cm), which provides a satisfactory estimation of the radii to both the front and rear.

S6.2. Interaction strength and distance-decay

The coupled dynamics of the two-fish system makes the *ab initio* selection of the interaction strengths, and associated distance decay parameters, much less straightforward. In

---

[2]MLE calibration of individual and interaction parameters simultaneously from pair data, including additional (nonlinear) likelihood terms for U^* and Ω^*, was attempted. However, some interaction parameters fail to converge on realistic (or known) values during the optimisation. Individual parameters (μ, σ, θ etc.) were also adversely affected.

this study, we take a heuristic approach: prescribing an initial set of interaction parameters, which are then manually tuned according to the resulting force profiles (Fig. 7) computed after full dynamical simulation of the model. Model realisations for different parametrisations are of a duration sufficient to explore a signification region of phase space so that we reduce the statistical noise in the resulting force maps. In this context, we always simulate 18 realisations of 20 min duration (30 Hz sample generation frequency) such that we have volume of data comparable with the experimental data set.

Experimentally, the amplitudes of $a^{\parallel}$ and $a^{\perp}$ are found to decay beyond distances of $\approx \pm 3\,\mathrm{BL}$, towards zero at around $d_{FB} \approx 7\,\mathrm{BL}$ and $d_{LR} \approx 6\,\mathrm{BL}$ respectively, giving us an indication of the range of attraction between conspecifics. However, from the position density plot (Fig. 2A), the cohesion between zebrafish pairs is very strong, finding a rapid reduction in the observed density beyond a similar range. The sparsity of data in this region, together with the artificial containment of the fish in a small tank, diminishes our ability to accurately estimate the range of either interaction.

For example, consider a hypothetical interaction in which attractive forces increases unbounded with distance. In this case, fish would be unable to stray further apart than a distance, determined chiefly by their equilibrium speed. Beyond this distance, the relative position density of a neighbour around a focal fish would rapidly decay to zero, with no detectable force, even though the attraction continues to grow with distance.

For both speeding and turning responses, we fixed interaction cut-off parameters, $\delta_u = 7\,\mathrm{BL}$ (21 cm) and $\delta_\omega = 6\,\mathrm{BL}$ (18 cm), and selected combinations of the remaining interaction parameters $\{K_s, \lambda_u\}$ and $\{K_p, \lambda_\omega\}$ to obtain adequate approximations to the experimentally observed force response profiles in Fig. 7. When selecting the initial values of for the remaining parameters, we therefore prioritised matching between the static model functions:

- tangential / speeding 'force':

$$a^{\parallel}_{\mathrm{est}}(d_{ij}, \theta_{ij}) = f_{d[u]} K_s (d_{ij} - r_u) \cos \theta_{ij} \qquad (29)$$

- radial / lateral 'force':

$$a^{\perp}_{\mathrm{est}}(d_{ij}, \theta_{ij}) = f_{d[\omega]} K_p (d_{ij} - r_\omega) \sin \theta_{ij} \qquad (30)$$

and corresponding experimental $a^{\parallel}$ and $a^{\perp}$, in the attractive regions before the peak response, where the neighbour position density was found to be highest (where $d_{FB}, d_{LR} < 3\,\mathrm{BL}$).

Through a process of trial-and-error to achieve best fits between resulting force profiles, we chose $K_s = 4\,\mathrm{s}^{-1}$ and $\lambda_u = 22.5\,\mathrm{cm}$ for the speed response, and $K_p = 6\,\mathrm{rad\,s}^{-2}$ and $\lambda_\omega = 6\,\mathrm{cm}$ for the (radial) turning response. Additionally, we selected $K_v = 12\,\mathrm{rad\,s}^{-2}$ according to the peak angular acceleration of the experimental $\dot{\omega}$ profile (Fig. 7C). For both speed and turning reposes, the corresponding combination of K and λ selected, produces estimated force profiles (red dashed trace) which overestimate the acceleration at distances beyond the experimental peaks observed. In both cases, the resulting model dynamics leads to excellent agreement with experimental force profiles. We also note, that although the sinusoidal dependence we prescribed for the alignment interaction ($K_v \sin \phi_{ij}$) somewhat overestimates the slope of $\dot{\omega}(\phi_{ij})$ compared with the experimental profile, the overall dynamical response is very well matched with model prediction. The complete set of interaction parameters described is provided in Tab. 2.

18

S6.3. Explicit vs. emergent alignment

To highlight the necessity of both radial attraction and alignment components of the turning response, we produced acceleration projections for simulations in which either has been selectively removed, that is setting K_p or K_v to zero respectively (Fig. S5). In particular, we refer here to the findings of Katz *et al.* [21] in which the study found no evidence of an explicit alignment interaction — assumed to emerge as a result of speed modulation and radial attraction.

Eliminating either the radial or angular component, results in essentially flat (zero) response profiles in terms of the associated acceleration projection, respectively: $a^\perp$ as a function of left-right separation d_{LR}, or $\dot{\omega}$ as a function of relative orientation ϕ_{ij}. In both cases, we find that the other response profiles, for $a^\parallel$, and either $a^\perp$ or $\dot{\omega}$, are only marginally affected with respect to nominal profiles. This observation supports our assertion that an explicit alignment rule is necessary to produce the observed angular acceleration response. Similarly, we find that the separate inclusion of two distinct behaviour responses: (i) radial attraction and repulsion in response on the position of a neighbour, and (ii) angular alignment in response to the orientation of a neighbour. Both observations can be justified in terms of the resulting pair dynamics.

With respect to our specific model, we also do not observe any compelling evidence of an emergent alignment response, resulting purely from position dependent attraction and repulsion, that is when $K_v = 0\,\mathrm{rad\,s}^{-2}$ (Fig. S5C3). As such, our observations potentially contradict assumptions made in [21] for golden shiners, in which angular accelerations were not considered. Studies in which alignment has been found to emerge without an explicit description, include those with purely attractive interactions [54, 55]. In these models, the formation of strongly polarised groups depends depends on precise combination of model parameters. However, when a frontal interaction bias, or blind zone, is introduced, collective patterns exhibiting strong local polarisation are dramatically enhanced.

To see whether frontally biased attractive (and repulsive) interactions leads to aligning interactions in our model, additional ($K_v = 0\,\mathrm{rad\,s}^{-2}$) simulations were performed, prescribing a blind-zone behind the focal fish with a posterior arc $\phi_b = \pi/2\,\mathrm{rad}$ (quarter circle). Neighbours within this cone, where $|\theta_{ij}| > \pi - (\phi_b/2)$, are rendered 'invisible' and thus do not elicit a response. Interestingly, this data does in fact yield a weak $\dot{\omega}$ response as a function of ϕ_{ij} (Fig. S5D3), providing some evidence of an emergent alignment response. This result, and those discussed in [54, 55], are clearly significant — indicating how the asymmetry of sensory fields can influence the observed interaction dynamics and emergent collective behaviours. From both $K_v = 0\,\mathrm{rad\,s}^{-2}$ data sets (Figs. S5C,D), we still find very close matching for linear acceleration responses ($a^\parallel$ and $a^\perp$). However, the strength of the experimental $\dot{\omega}$ response greatly exceeds the emergent response due to sensory asymmetry, suggesting that an explicit alignment may in fact be the dominant mechanism in zebrafish.

The dynamic effects of removing the alignment response are also described in the following figures, in terms of the semi-spatial force maps in Fig. S6, the full spatial force maps in Fig. S7, and distributions of the collective dynamical observables ($P, M, C, MNND, E$) in Fig. S8.
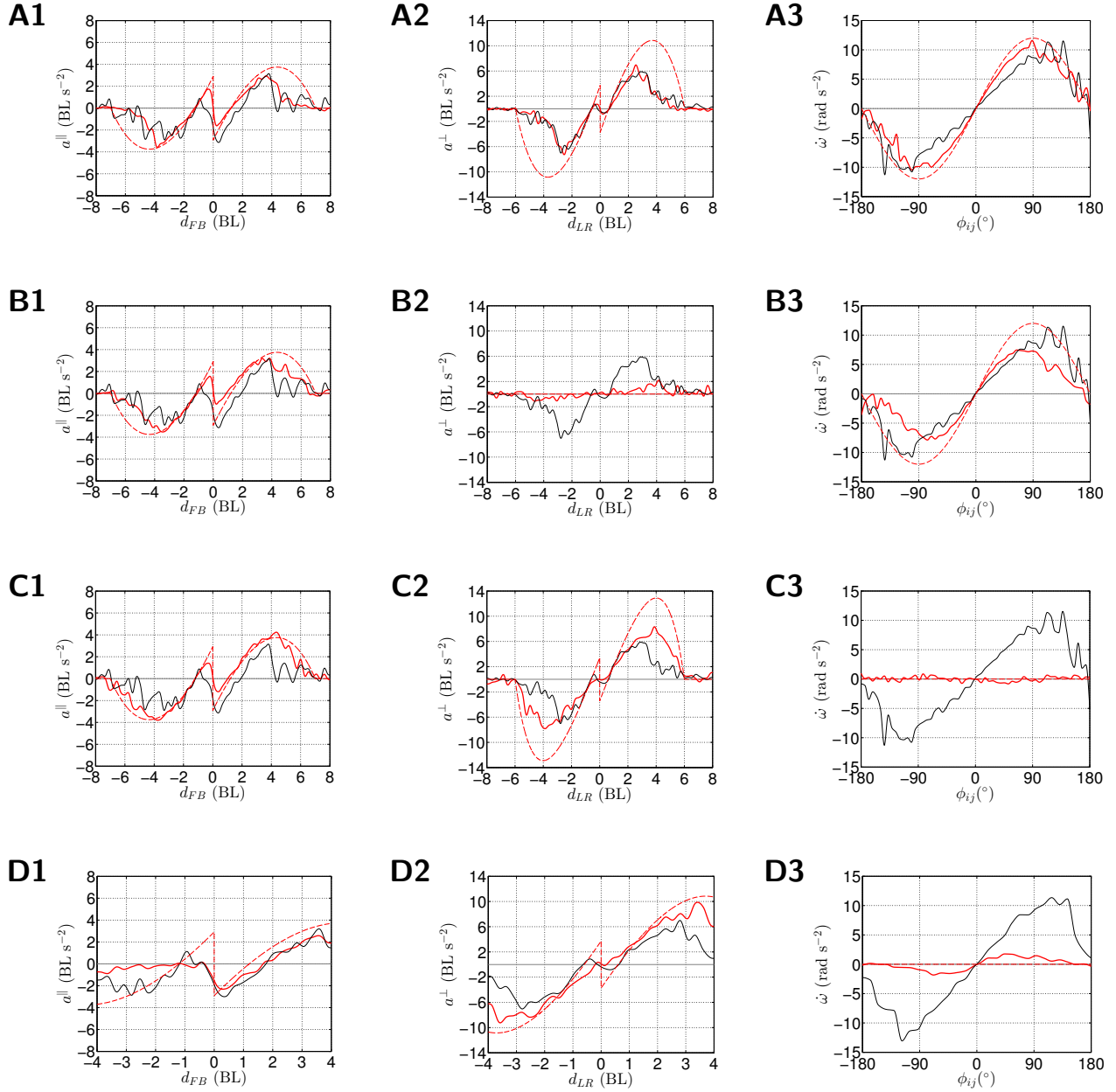
Figure S5: **Axial force projections for simulated fish pairs with inhibited turning behaviours.**
(A) Nominal parameters for radial attraction and alignment, i.e. with $K_s = 4\,\mathrm{s}^{-1}$, $K_p = 6\,\mathrm{rad\,s}^{-2}$ and
$K_v = 12\,\mathrm{rad\,s}^{-2}$, (B) no radial attraction rule: $K_p = 0\,\mathrm{rad\,s}^{-2}$, (C) no alignment rule: $K_v = 0\,\mathrm{rad\,s}^{-2}$, and
(D) no alignment rule ($K_v = 0\,\mathrm{rad\,s}^{-2}$) but also specifying a rear blind-zone with angle of $\phi_b = \pi/2$ within
which agents do not contribute to interactions. Projections shown are for: (1) tangential acceleration $a^{\parallel}$ in
the $d_{LR} = 0$ axis, parallel to the focal fish's direction of motion, (2) radial acceleration $a^{\perp}$ in the $d_{FB} = 0$
axis, perpendicular to the direction of motion, and (3) angular acceleration $\dot{\omega}$ as a function of the relative
heading angle ϕ_{ij} between focal fish i and neighbour j. Data from simulated trajectories (red) are compared
to experimental zebrafish data (black). Parametrised input functions for each rule (speeding attraction,
turning attraction and alignment) are shown in respective panels (red dashed).
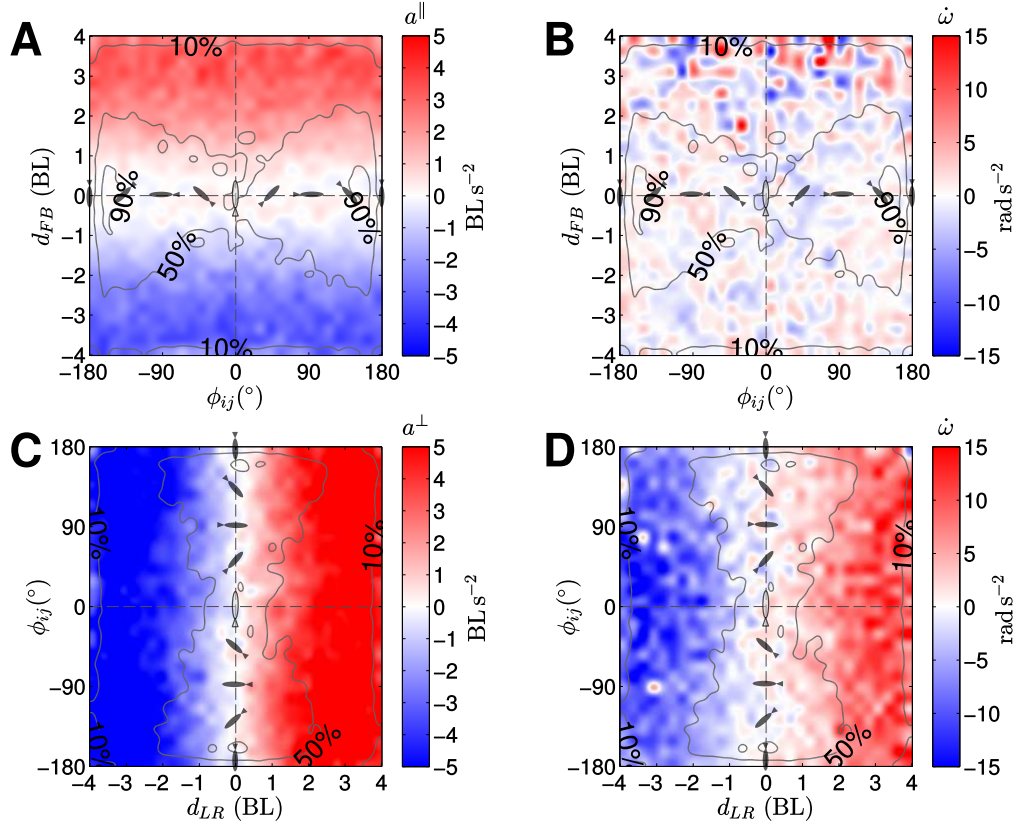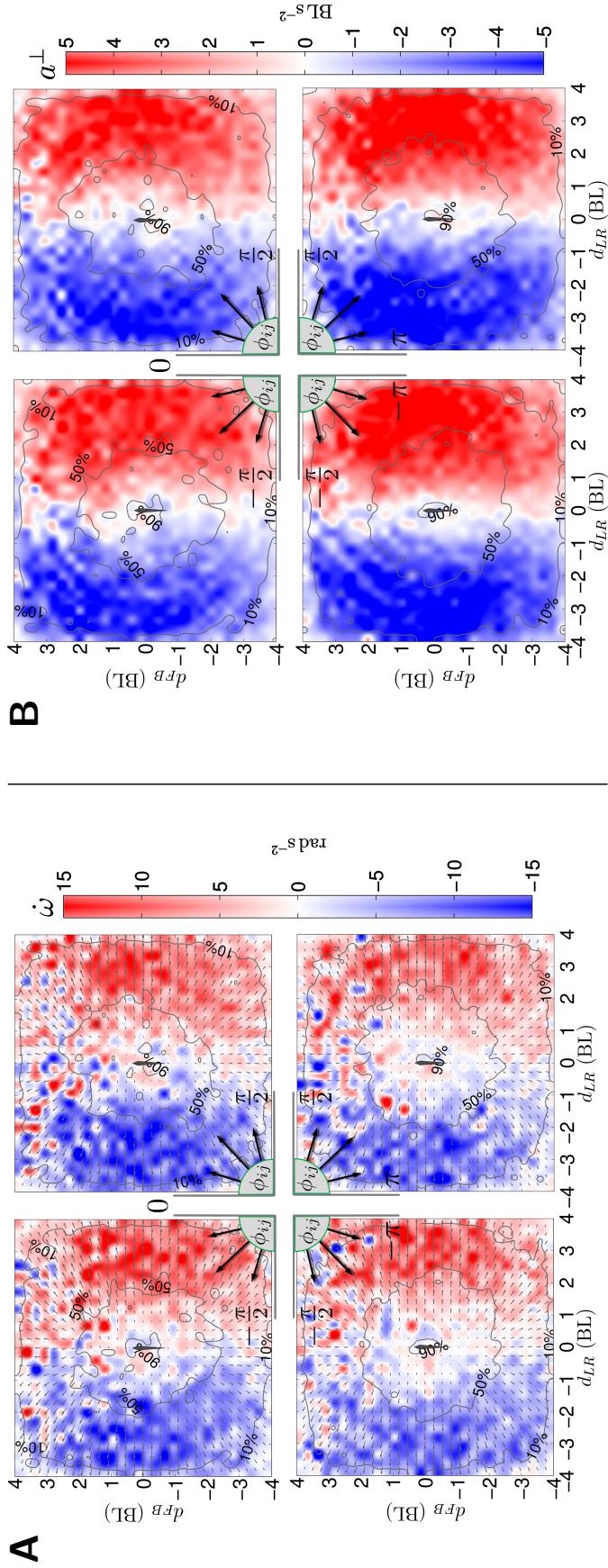
Figure S6: **Force maps plotted as a function of the relative heading angle between simulated conspecifics with no alignment rule.** Data mapped from simulated realisations ($18 \times 20\,\mathrm{min}$) of fish pair with nominal parameters but with no explicit alignment interaction: $K_v = 0\,\mathrm{rad\,s^{-2}}$. Panel descriptions as per Fig. 3. From this data, we find that when explicit alignment is removed, angular acceleration depends only on the perpendicular separation (B), with no detectable response to the relative orientation of the pair (C) — as found experimentally.

Figure S7: **Force maps plotted as a function of the relative heading angle between simulated conspecifics with no alignment rule.** Histograms map show: (A) the average angular acceleration $\dot{\omega}$, and (B) radial acceleration $a^{\perp}$ of the focal fish, as they vary depending on the relative position of its neighbour. Panel descriptions as per Fig. 4. With no explicit alignment rule, the angular acceleration is governed only by attractive interactions such that focal fish turns always towards the position of a neighbour, regardless of its orientation. As such, there is essentially no difference between the spatial structure of the angular and radial accelerations shown with respect to relative orientation.
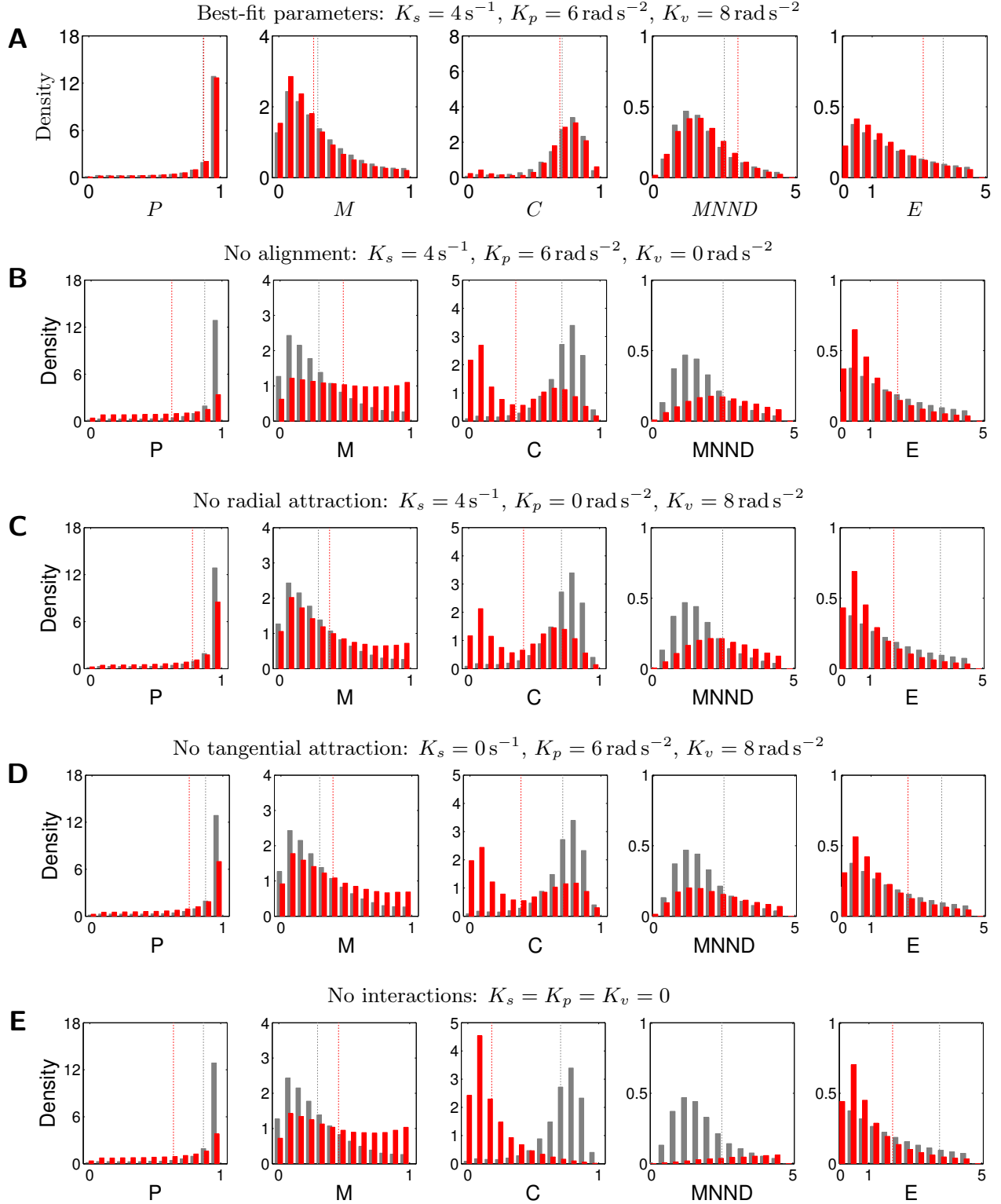
Figure S8: **Collective dynamics of simulated fish pair with inhibited interaction behaviours.** Distributions of global observables of experimental zebrafish pair data (grey) are compared with simulated data (red), where pair interact with: (A) best fit parameters $K_s = 4\,\mathrm{s}^{-1}$, $K_p = 6\,\mathrm{rad\,s}^{-2}$ and $K_v = 8\,\mathrm{rad\,s}^{-2}$, (B) no alignment rule: $K_v = 0\,\mathrm{rad\,s}^{-2}$, (C) no radial attraction rule: $K_p = 0\,\mathrm{rad\,s}^{-2}$, (D) no tangential attraction rule: $K_s = 0\,\mathrm{s}^{-1}$, and (E) no interactions: $K_s = K_p = K_v = 0$. From left to right, histograms report: (P)olarisation, (M)illing, (C)ohesion, Mean nearest-neighbour distance ($MNND$), and (E)longation. Mean values shown by vertical dashed lines.

23

S7. Social interaction network

The primary motivation of this work is to explore the structure and function of interaction behaviours between pairs of zebrafish, such that the topology of the 'network' is essentially binary: either fish are interaction, or they are not. For a pair of conspecifics in our model (Fig. S9A), the range of interaction is limited by the largest of the two distance-decay cutoff parameters: $\max\{\delta_u, \delta_\omega\}$. If this maximum value is the same for both fish, then the trivial network structure is described by a radial, metric topology, that is both fish are interacting only if $d_{ij} < \max\{\delta_u, \delta_\omega\}$. However, if these cutoff values are heterogeneous, the simple network may be directed such that one fish is connected to the other but not vice versa.

For small groups of fish $N \leq 3$, the interaction network between individuals is defined purely in terms of their individual range of perception (Fig. S9B). For populations exceeding 3 individuals (see main text §5), more realistic interaction topologies can be enforced, disconnecting pairs which might otherwise be within (radial) perceptive range. Here, for populations of $N > 3$ individuals (Fig. S9C), we use the (undirected) Voronoi partition. In this construction, we define regions around each individual, inside which another individual ($\mathbf{p}$) is closer to an individual that it is to any of its other neighbours [56]. A geometric description corresponding to these regions is provided by the two-dimensional Voronoi tessellation, were for N individuals with positions $\{\mathbf{x}(t)_i\}_{i=1}^{N} \in \mathbb{R}^2$ at time t, we obtain the i'th Voronoi cell (polygon) $V_i(t)$ as follows

$$V_i(t) = \{\mathbf{p} \in \mathbb{R}^2 \quad | \quad \|\mathbf{x}(t)_i - \mathbf{p}\| \leq \|\mathbf{x}(t)_j - \mathbf{p}\|, \quad \forall j \neq i, j \in \mathcal{V}\} \tag{31}$$

Within this spatial partitioning, two individuals at $\mathbf{x}(t)_i$ and $\mathbf{x}(t)_j$ are first-shell neighbours only if they share a Voronoi boundary, with elements of the adjacency matrix $\mathcal{A} = \{a_{ij}\}$ given by:

$$\text{(Voronoi adjacency):} \quad \{a_{ij}\} = \begin{cases} 1 & \text{if } V_i(t) \cap V(t)_j \neq \emptyset \\ 0 & \text{otherwise} \end{cases} \tag{32}$$
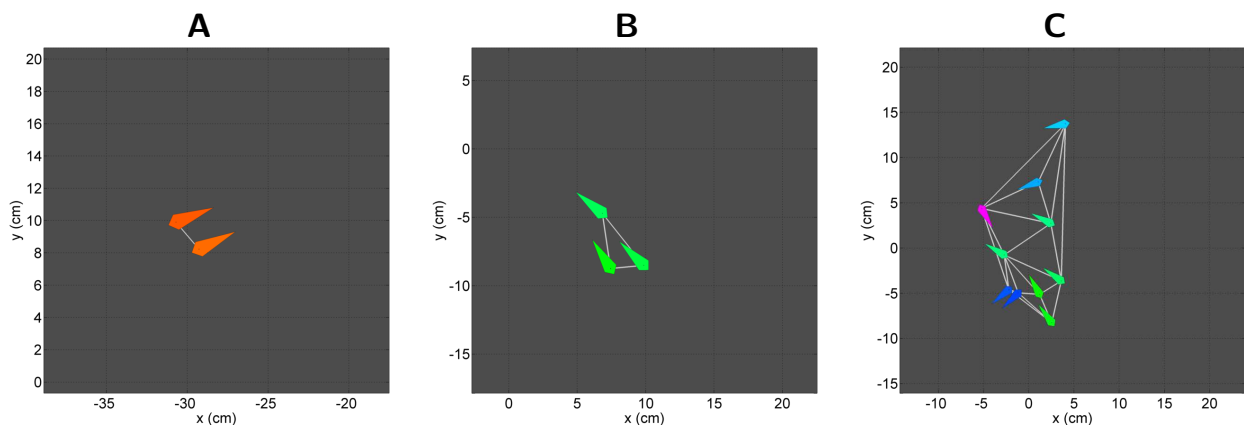

Figure S9: **Interaction network topology for different population sizes.**
(A) $N = 2$ fish interact via undirected, one-to-one coupling. (B) $N = 3$ fish interact via undirected, all-to-all coupling. (C) $N = 10$ fish, all within radial perceptive range, interact via undirected topology derived from the Voronoi tessellation of their positions (vertices of the Delaunay triangulation). Fish are represented by polygons with front to back length equal to 1 BL, coloured according to their heading angle ϕ_i.

i.e. where points of intersection are on the boundaries of both Voronoi cells [57, 58]. The ₁₀₁₃ corresponding interaction network is given by the dual representation, know as the Delaunay ₁₀₁₄ triangulation [59], where individuals sharing a Voronoi boundary are connected by a *Delaunay* ₁₀₁₅ *Edge*. ₁₀₁₆

With no impact on the resulting dynamics, we also apply an additional radial cutoff for ₁₀₁₇ homogeneous individuals according to distance-decay parameter $\delta_{u/\omega}$ — setting elements of ₁₀₁₈ the network adjacency matrix $a_{ij} = 0$, where $d_{ij} > \max\{\delta_u, \delta_\omega\}$. ₁₀₁₉

S8. Quantifying collective dynamics: global observables ₁₀₂₀

In what follows, we derive a set of scale invariant order parameters *Polarisation* and ₁₀₂₁ *Milling*, variations of which are typically used to describe the collective dynamical structures ₁₀₂₂ of fish schools [31, 38, 58, 60–62]. We also provide additional measures, *Cohesion, Mean* ₁₀₂₃ *nearest-neighbour distance* and *Elongation*, which together provide further quantification of ₁₀₂₄ the spatial arrangement, shape, and density of individuals within the group. Unlike polari- ₁₀₂₅ sation and milling, values of these observables depend on the spatial distribution, and metric ₁₀₂₆ distances between fish. ₁₀₂₇

The centre-of-mass (CoM) of a group of N individuals at time t, on a two-dimensional plane is defined as the vector mean of their individual positions $\mathbf{x}(t) = \{[x(t), y(t)]_i\}_{i=1}^{N}$, such that

$$\mathbf{X}(t) = \frac{1}{N} \sum \mathbf{x}_i(t) \tag{33}$$

from which we derive the relative position vectors $\mathbf{r}_i(t)$ of each fish with respect to the CoM, where

$$\mathbf{r}_i(t) = \mathbf{x}_i(t) - \mathbf{X}(t) \tag{34}$$

In this frame of reference, the state of the collective system at time t is determined by ₁₀₂₈ three order parameters, with range $[0, 1]$, which together describe the collective state of the ₁₀₂₉ shoal: (i) Polarisation $P(t)$, the degree to which the orientations of the agents are aligned, ₁₀₃₀ maximised when fish orientations are aligned; (ii) Milling $M(t)$, a measure of the group ₁₀₃₁ rotational momentum about the CoM, maximised when agents are rotating in a common ₁₀₃₂ sense of direction; and (iii) Cohesion $C(t)$, providing a measure of the spread of agents about ₁₀₃₃ the CoM, with respect to a fixed scale-length. These order parameter are defined as follows. ₁₀₃₄

- Polarisation: $P(t)$

$$P = \frac{1}{N} \left\| \sum_{i=1}^{N} \frac{\mathbf{v}_i}{\| \mathbf{v}_i \|} \right\| \tag{35}$$

  Here we define the polarisation of the shoal by considering the Euclidean norm $\|.\|$ ₁₀₃₅ of the mean (unit) velocity vector. Subsequently, $P \to 1$ when all unit vectors are ₁₀₃₆ aligned, and $P \to 0$ when unit vectors are equally distributed around the unit circle, ₁₀₃₇ independent of the speed $\|\mathbf{v}(t)\|$ of each fish. ₁₀₃₈

- Milling: $M(t)$

$$M = \frac{1}{N} \left\| \sum_{i=1}^{N} \frac{\mathbf{r}_i \times \mathbf{v}_i}{\| \mathbf{r}_i \| \| \mathbf{v}_i \|} \right\| \tag{36}$$

25

In the above formula, we compute the (unit) cross product between the velocity of each fish $\mathbf{v}_i(t)$, and the vector $\mathbf{r}_i(t)$ pointing towards the CoM of the group. The normalised mean value of the resulting orthogonal vectors provides $M \to 1$ when the velocity vectors are tangential to concentric circles centred on the CoM, rotating in the same directional sense. Correspondingly, the milling observable vanishes, $M \to 0$, when the net angular momentum about the CoM is zero.

- Cohesion: $C(t)$

$$C = \frac{1}{N} \sum \exp\left(- \parallel \mathbf{r}_i \parallel / r_{\text{coh}})\right) \tag{37}$$

Here, C represents the spread of positions around the CoM in terms of the distances $\|\mathbf{r}_i\|$, scaled by a fixed length $r_{\text{coh}} = 3\,\text{BL}$ – constant throughout this work and defined as per [60]. The function describes an exponential decay from unity to zero, where $C = 1$ only when all positions are superimposed (unrealistic for larger groups), and $C \to 0$ with a rate dependent on r_{coh}. For our choice of $r_{\text{coh}} = 3\,\text{BL}$, $C \approx 0.5$ when the fish are on average $2\,\text{BL}$ from the CoM, reducing to $C \approx 0.1$ when the separation average increases to approximately $7\,\text{BL}$.

Unlike order parameters P and M described above, values of C and the additional global observables defined here, provide values which depend crucially on the spatial distribution of individual fish positions. For example, the polarisation of a shoal is independent of the spatial arrangement of the individuals — only their orientation is considered, regardless of the individual positions. As such, a polarised shoal ($P \approx 1$), equally describes fish swimming side-by-side, or in single-file configuration. In this case, we differentiate between these two formations, and any intermediate configuration, by introducing a measure of the shoal elongation $E(t)$, along the group average heading direction [63]. The varying spatial dimensions of a coherent shoal implies local (shoal) density fluctuations, even though the total (environmental) population density in a confined environment remains constant. A useful indication of this local density, providing the average separation between individuals, is obtained from the mean nearest-neighbour distance $MNND$. These two additional spatial observables are derived as follows:

- Elongation: $E(t)$

$$E = \frac{l_{\parallel\langle\mathbf{v}_n\rangle}}{l_{\perp\langle\mathbf{v}_n\rangle}} \tag{38}$$

The elongation of a shoal is computed as the aspect ratio of the minimal bounding box containing agents at x where $l_{\parallel}$ and $l_{\perp}$ are respectively the side lengths parallel and perpendicular to the mean group velocity $\langle\mathbf{v}_n\rangle$. Accordingly, $E > 1$ when the shoal is elongated in its direction of motion, and $0 < E \leq 1$ otherwise. Noting that by this measure E is essentially unbounded, we set a maximum value of $E = 20$ for highly elongated shoals.

- Mean-nearest neighbour distance: $MNND(t)$:

$$MNND = \frac{1}{N} \sum_{i=1}^{N} \min\left(\{\parallel \mathbf{x}_i - \mathbf{x}_j \parallel\}_{i \neq j}\right) \tag{39}$$

26

The above formula calculates the separation between each individual i and its closest neighbour j, returning the average (mean) value over each of the N members of the shoal. The resulting *MNND* defines the average shortest distance between fish at time t, generally expressed in multiples of BL. Note that for experiments with $N = 2$ fish, the *MNND* is equivalent to the pair separation $d_{ij}(t) \equiv d_{1,2} \equiv d_{2,1}$.

From this description, it is apparent that for shoals which maintain a constant local density, the relative separation between individuals, given by the *MNND* should also remain constant, independent of the population size N. By comparison, group Cohesion (C) measured with respect to the CoM, decreases for larger N at constant local density as the spatial size of the shoal grows. We note that whilst the order parameter C offers a useful indication of the spread of positions around the CoM, its value is consistent only for comparing populations of the same population size. The *MNND* however, provides a consistent indication of group density, regardless of the population size.

S9. Additional figures
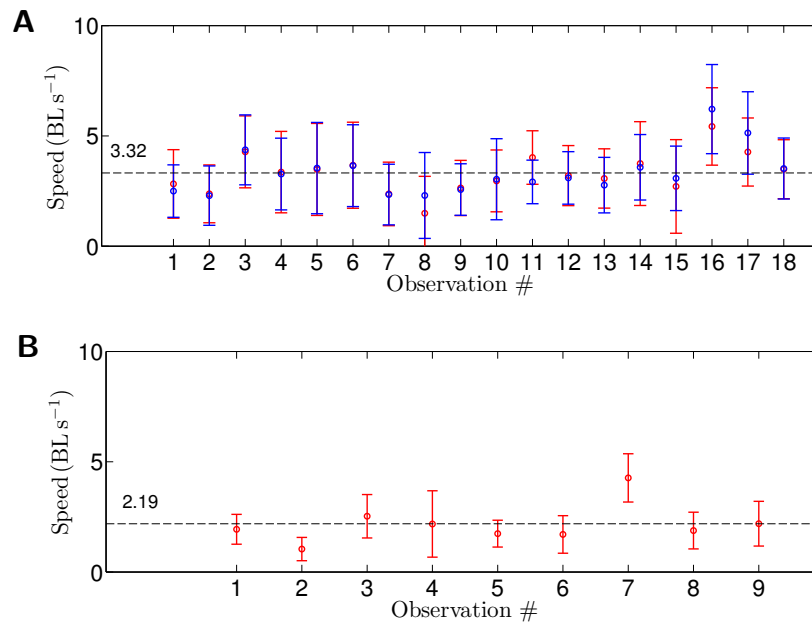
Figure S10: **Mean swimming speed of zebrafish in isolation and in pairs.** Plots indicate the mean swimming speed of individuals, (A) for 18 observations of zebrafish pairs — data from this study, and (B) for 9 observations of zebrafish swimming in isolation — data from [43]. Identical experimental conditions were maintained for both data sets using experimentally naïve fish for all observations. Group mean for each data set is shown as black dashed line .
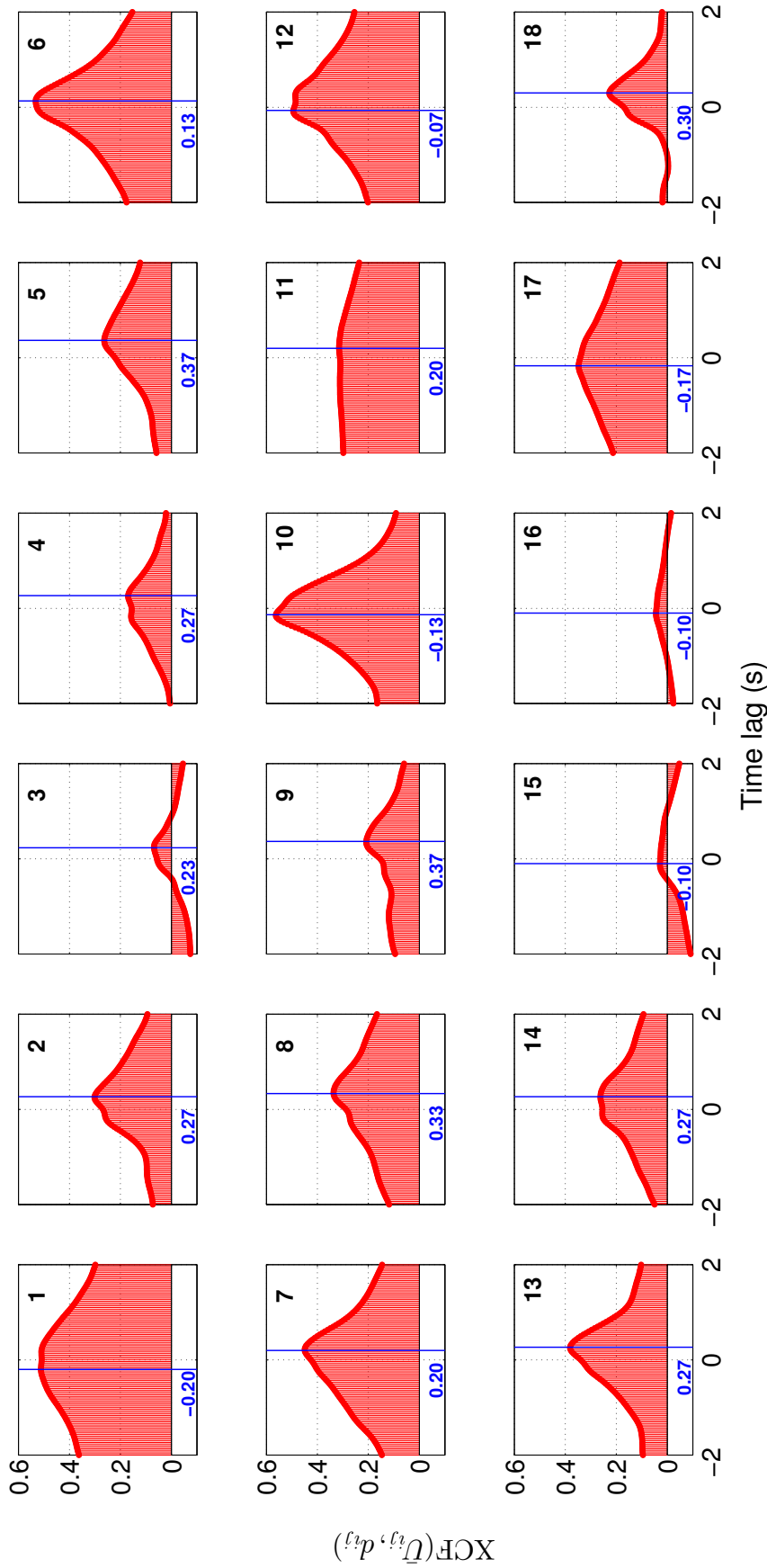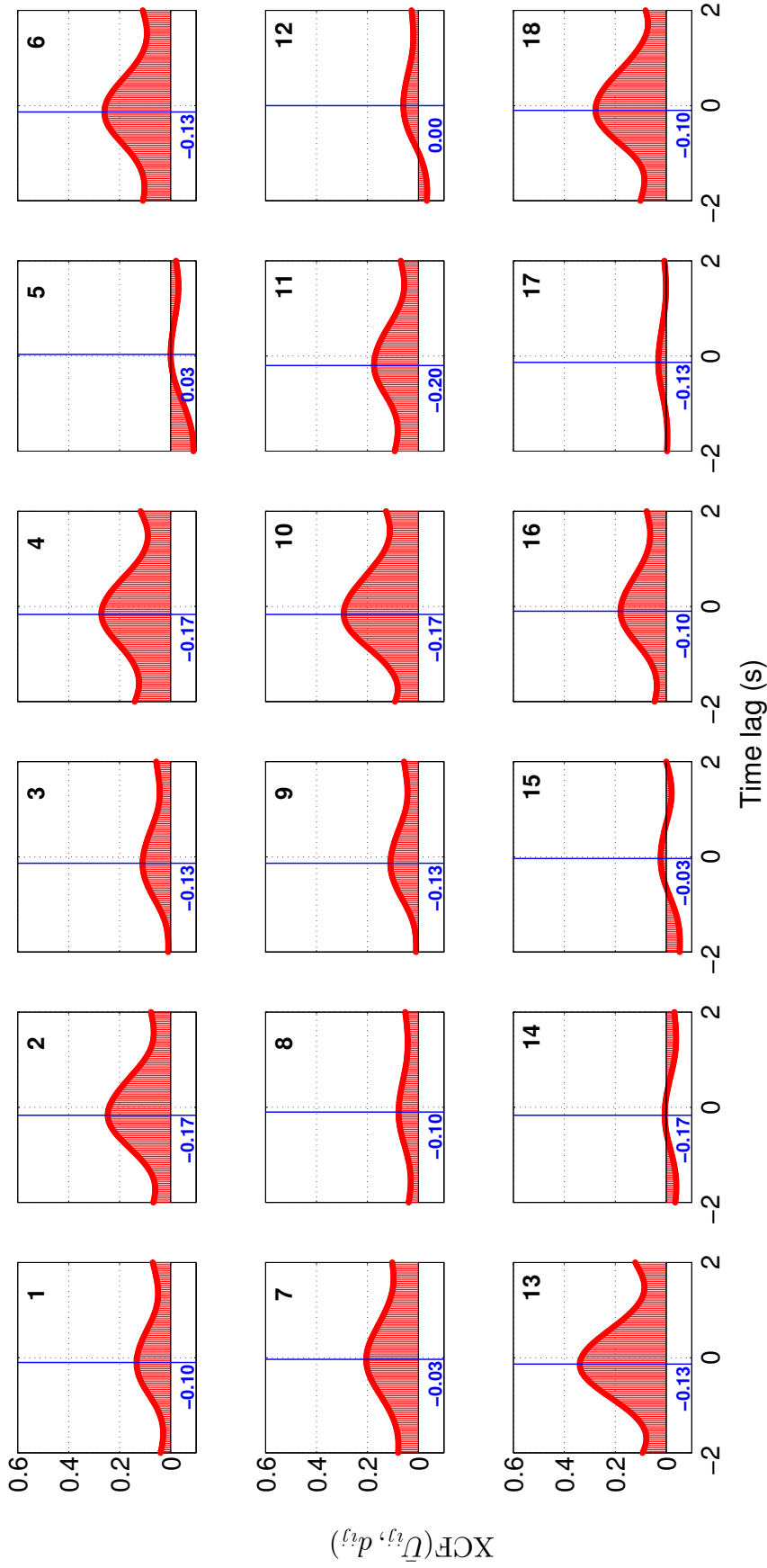
Figure S11: **Cross correlation function (XCF) of mean speed and pair separation.** Here we report the normalised XCF = $\mathrm{XCF}'(\bar{u}, d_{ij})/\sqrt{\sum_t |\bar{u}(t)|^2 \overline{\sum_t |d_{ij}(t)|^2}}$, as a function of the time lag between samples (red), for each observation (1-18) of a swimming zebrafish pair. We find a strong positive correlation, where the pair separation distance d_{ij} leads the mean speed of the pair $\bar{u}$ by approximately 0.14s on average (individual observation values shown in blue) — suggesting further evidence that fish regulate their speed in response to their separation, slowing down when their separation decreases and vice versa.

Figure S12: **Cross correlation function (XCF) of mean speed and pair separation.** Here we report the normalised XCF $= \mathrm{XCF}'(\bar{u}, d_{ij})/\sqrt{\sum_t |\overline{u(t)}|^2 \sum_t |\overline{d_{ij}(t)}|^2}$, as a function of the time lag between samples (red), for 18 simulated realisations of the model with two fish. Simulated pairs yield similar correlations to experimental data in Fig. S11, but where the mean speed of the pair $\bar{U}$ now leads the separation distance d_{ij}, by approximately $0.1\,\mathrm{s}$ on average.
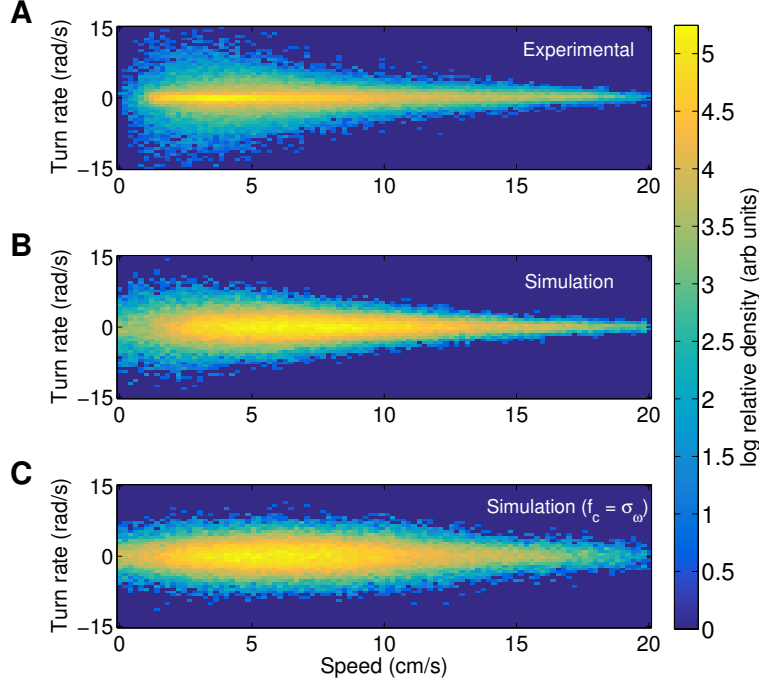
Figure S13: **Comparing joint distribution of speed and turn-rate for experimental and simulated trajectories.** (A) Analysing the ensemble of 9 individual zebrafish trajectories (data from [43]) reveals the speed dependence of the turn-rate distribution. The variance and range of the turn-rate is found to increase at low speeds, noting that tails of the turn-rate distribution are most affected, becoming progressively fatter. (B) Ensemble of 9 simulated trajectories, individually calibrated on the respective zebrafish observation, using model with speed coupled turn-rate variance f_c. By coupling the variance of the turn-rate fluctuations at time t (exponentially) to the speed $U(t)$, we achieve a reasonable approximation to the experimental data. The distribution of the simulated turn-rate is however less sharply peaked with thinner tails. (C) Ensemble of 9 simulated trajectories, calibrating parameters assuming fixed turn-rate variance parameter σ_ω for each realisation. The resulting joint-normal distribution fails to capture the increasing range and variance of the turn-rate at lower speeds.
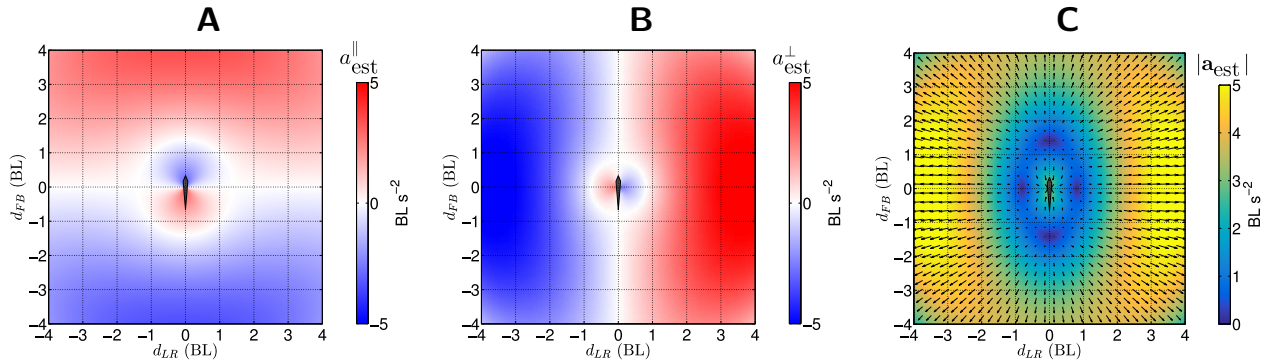

Figure S14: **Spatial mapping of model bias functions as functions of the relative pair separation without dynamics (static model).** Panels show histograms of the expected acceleration of a focal fish in orthogonal components with respect to its orientation, using the nominal parameter set given in Tab. 2, with $K_p = 5\,\mathrm{rad\,s^{-2}}$ and $\lambda_\omega = 18$. (A) tangential acceleration $a_{\mathrm{est}}^{\parallel}$. (B) radial acceleration $a_{\mathrm{est}}^{\perp}$. (C) resultant magnitude of linear accelerations with arrows indicating the vector field $[a_{\mathrm{est}}^{\parallel}, a_{\mathrm{est}}^{\perp}]$.
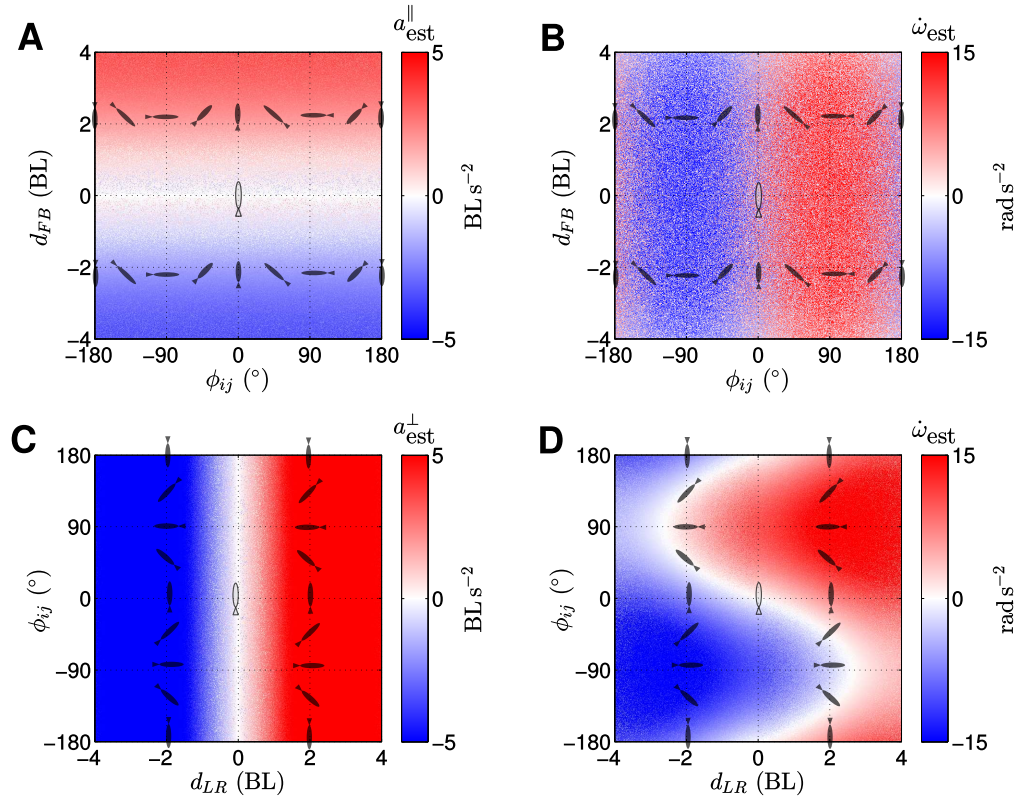
Figure S15: **Static model estimation of linear and angular accelerations as a function of relative position and pair orientation** ϕ_{ij}**.** Panels (A) and (C) show respectively the tangential and radial acceleration maps as functions of d_{FB}, d_{LR}, and ϕ_{ij} computed via (29) and (30), where position data in the missing spatial coordinate in all panels are randomised uniformly between the axis limits. Nominal parameters given in Tabs. 1 & 2 are to compute values at pixel coordinate. Panels (B) and () report the total angular acceleration ($\dot{\omega} \approx \theta_\omega \Omega^*$) computed via (5b). The angular acceleration estimate in panel (D) predicts the continuous distance-dependent weighting between the attraction and alignment turning responses. At short range ($d_{LR} < 2\,\mathrm{BL}$) alignment dominates where $\dot{\omega}$ varies principally as a function of ϕ_{ij}. Beyond this distance, attraction starts to dominate with the sign of the acceleration dependent primarily on whether the neighbour is on the left or right of the focal fish (sign of d_{LR}).
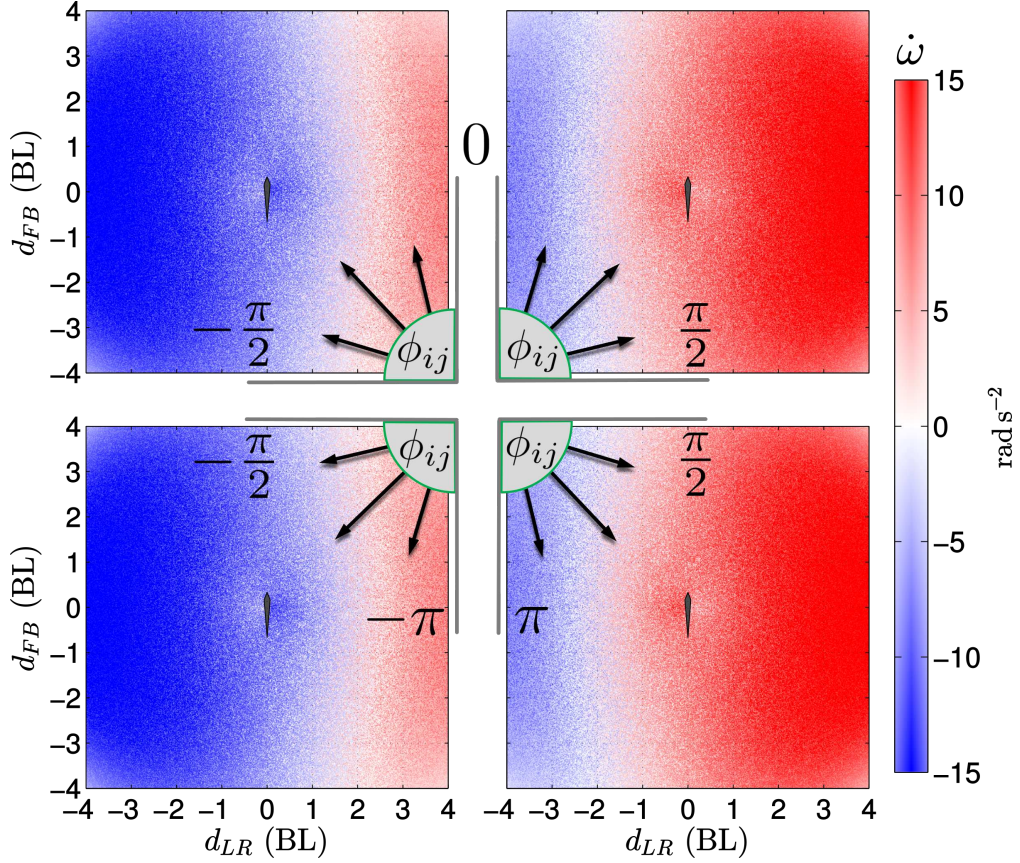
Figure S16: **Static model estimation of angular accelerations as a function of relative pair position for neighbours with different relative orientations.** Maps show the static model estimation of the average angular acceleration $\dot{\omega}_{\text{est}} = \theta_\omega \Omega^*$ of the focal fish, as a function of the relative position of a neighbour. Angular acceleration is computed via (5b) at each pixel coordinate, using nominal parameters from Tabs. 1 & 2. Panels show value computed using orientation (ϕ_{ij}) values uniformly randomised within ranges corresponding to four quadrants: (top-left) $-\frac{\pi}{2} < \phi_{ij} \leq 0$, (top-right) $0 < \phi_{ij} \leq \frac{\pi}{2}$, (bottom-left) $-\pi < \phi_{ij} \leq -\frac{\pi}{2}$, (bottom-right) $\frac{\pi}{2} < \phi_{ij} \leq \pi$, where positive values indicate neighbour is rotated clockwise with respect to the focal fish. Positive angular accelerations, or radial forces (red) indicate increased (clockwise) turning or acceleration to the right, negative angular accelerations or radial forces indicate increased (anti-clockwise) turning or acceleration to the left.
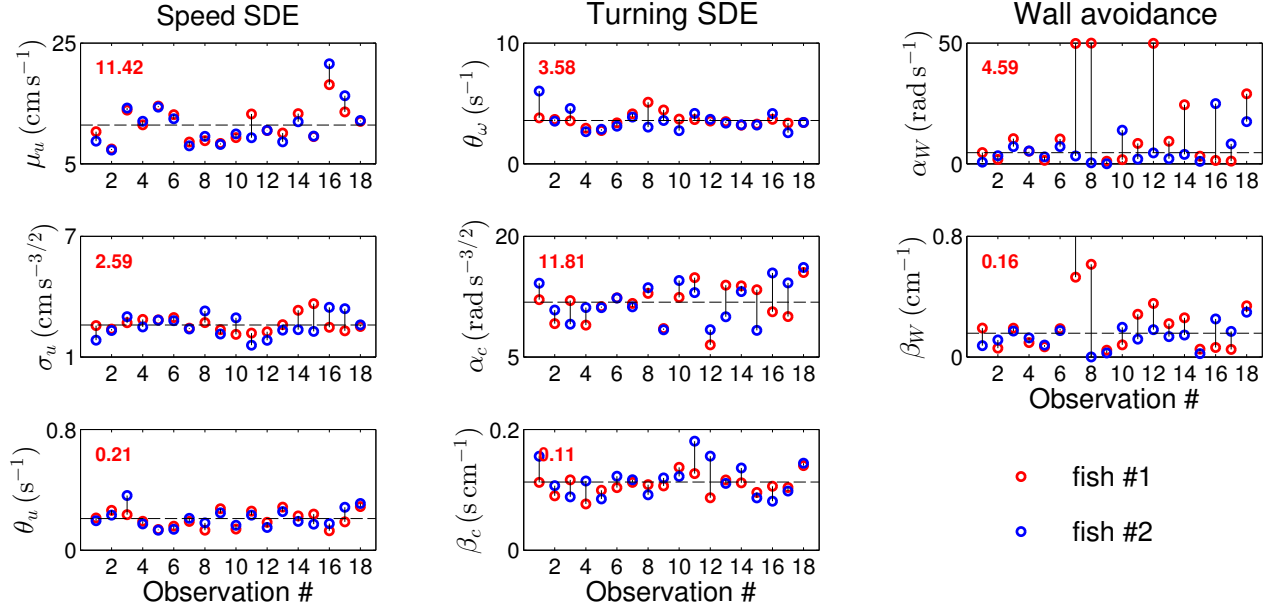
Figure S17: **Estimating mean parameters from observations of interacting zebrafish swimming in pairs.** Model parameters for 18 observations of zebrafish pairs are estimated using MLE for each individual fish (red and blue). Position data for all individuals was smoothed with a 29 sample window ($\tau \approx 1.0$ sec.) SG3 filter. The overall mean value for each parameter is given in each panel and marked (black dashed lines) - median values shown for α_W, β_W due to outliers where MLE procedure did not converge.
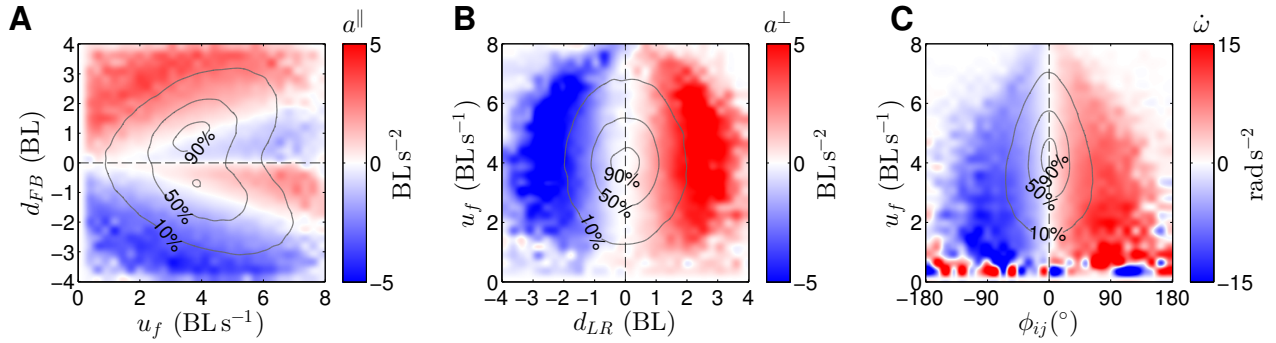

Figure S18: **Force mapping as a function of the focal fish speed (simulated data).** Trajectory data obtained from a simulated pair (1x360 min realisation) with nominal parameters. Force maps showing (A) the tangential acceleration $a^{\parallel}$ as a function of front-back separation d_{FB}, (B) radial acceleration $a^{\perp}$ as a function of left-right separation d_{LR}, and (C) angular acceleration $\dot{\omega}$ as a function of the relative orientation ϕ_{ij}, each as functions of the speed of the focal fish U_f. Contours show the population density of neighbours relative to the most common configuration.
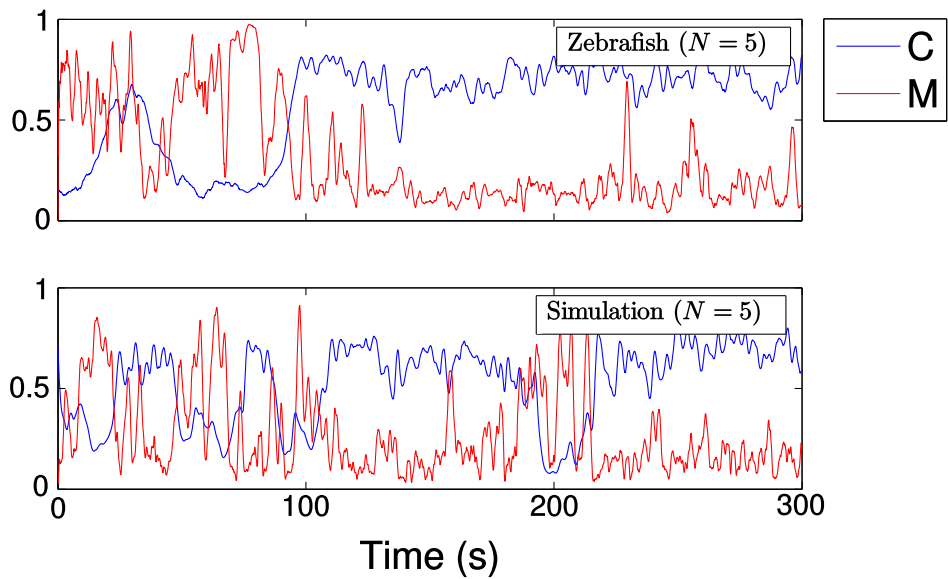
Figure S19: **Cohesion and milling time-series for** $N = 5$ **fish shoals.** Traces indicate $C(t)$, and $M(t)$ time-series for an observations of a five zebrafish shoal (top), and a simulated model realisation (bottom). In both instances we find that transient periods of rotational milling ($M \to 1$), are associated with reduced cohesion. The distribution of C is therefore subtly bimodal, exhibiting an additional small peak at low C corresponding to the value associated with transient rotational mills. Note that this features is not observed in $N = 2$ fish data since the milling radius is more comparable to the nominal pair separation — as such, the value of C is much less affected.

Additional references

[44] G. M. Cahill, Clock mechanisms in zebrafish., Cell Tissue Res. 309 (1) (2002) 27–34. 1086

[45] K. Wong, M. Elegante, B. Bartels, S. Elkhayat, D. Tien, S. Roy, J. Goodspeed, C. Suciu, 1087
J. Tan, C. Grimes, A. Chung, M. Rosenberg, S. Gaikwad, A. Denmark, A. Jackson, 1088
F. Kadri, K. M. Chung, A. Stewart, T. Gilder, E. Beeson, I. Zapolsky, N. Wu, J. Cachat, 1089
A. V. Kalueff, Analyzing habituation responses to novelty in zebrafish (*Danio rerio*)., 1090
Behav. Brain Res. 208 (2) (2010) 450–457. 1091

[46] C. Carson, S. Belongie, Blobworld: Image segmentation using expectation-maximization 1092
and its application to image querying, IEEE Trans Pattern Anal. Mach. Intell. 24 (2002) 1093
1026–1038. 1094

[47] A. Savitsky, M. J. E. Golay, Smoothing and differentiation of data by simplified least 1095
squares procedures, Anal. Chem. 36 (8) (1964) 1627–1639. 1096

[48] S. R. Krishnan, C. S. Seelamantula, On the selection of optimum Savitzky-Golay filters, 1097
IEEE Trans. Signal Process. 61 (2) (2013) 380–391. 1098

[49] F. Janabi-Sharifi, Discrete-time adaptive windowing for velocity estimation, IEEE Trans. 1099
Control Syst. Technol. 8 (6) (2000) 1003–1009. 1100

[50] V. Mwaffo, S. Butail, M. di Bernardo, M. Porfiri, Measuring zebrafish turning rate., 1101
Zebrafish 12 (3) (2015) 250–4. 1102

[51] P. Kloeden, E. Platen, Numerical solution of stochastic differential equations, Springer- 1103
Verlag, 1992. 1104

[52] C. Gardiner, Stochastic methods, Springer-Verlag, 2009. 1105

[53] D. Gillespie, Exact numerical simulation of the Ornstein-Uhlenbeck process and its in- 1106
tegral, Phys. Rev. E 54 (2) (1996) 2084–2091. 1107

[54] D. Strömbom, Collective motion from local attraction., J. Theor. Biol. 283 (1) (2011) 1108
145–151. 1109

[55] D. Strömbom, M. Siljestam, J. Park, D. J. T. Sumpter, The shape and dynamics of local 1110
attraction, Eur. Phys. J. 3323 (2015) 1–13. 1111

[56] U. Lopez, J. Gautrais, I. D. Couzin, G. Theraulaz, From behavioural analyses to models 1112
of collective motion in fish schools, Interface Focus 2 (6) (2012) 693–707. 1113

[57] M. Kolahdouzan, C. Shahabi, Voronoi-based K nearest neighbor search for spatial net- 1114
work databases, Proc. 30th Int. Conf. Very Large Databases 30 (2004) 840–851. 1115

[58] A. Kolpas, M. Busch, H. Li, I. D. Couzin, L. Petzold, J. Moehlis, How the spatial 1116
position of individuals affects their influence on swarms: a numerical comparison of two 1117
popular swarm dynamics models., PLoS One 8 (3) (2013) e58525. 1118

[59] F. Aurenhammer, Voronoi diagrams—a survey of a fundamental geometric data structure, ACM Comput. Surv. 23 (3) (1991) 345–405.

[60] M. Aureli, M. Porfiri, Coordination of self-propelled particles through external leadership, EPL 92 (4) (2010) 40004.

[61] M. Aureli, F. Fiorilli, M. Porfiri, Portraits of self-organization in fish schools interacting with robots, Phys. D Nonlinear Phenom. 241 (9) (2012) 908–920.

[62] T. Vicsek, A. Zafeiris, Collective motion, Phys. Rep. 517 (3-4) (2012) 71–140.

[63] I. D. Couzin, J. Krause, N. R. Franks, S. A. Levin, Effective leadership and decision-making in animal groups on the move., Nature 433 (7025) (2005) 513–6.